

UNIVERSIDADE DE SANTIAGO DE COMPOSTELA
FACULTAD DE FÍSICA
Departamento de Física de Partículas



**Charge exchange and knockout reactions
induced by Sn isotopes at relativistic energies**

Jossitt W. Vargas Cruz
Mayo de 2014

UNIVERSIDADE DE SANTIAGO DE COMPOSTELA
FACULTAD DE FÍSICA
Departamento de Física de Partículas



**Charge exchange and knockout reactions
induced by Sn isotopes at relativistic energies**

Memoria presentada por:
Jossitt W. Vargas Cruz
como disertación para optar al
Grado de Doctor
en Ciencias Físicas
Mayo de 2014

**UNIVERSIDADE DE SANTIAGO DE
COMPOSTELA**

José Benlliure, Catedrático de del Departamento de Física de Partículas de la Universidad de Santiago de Compostela

CERTIFICA:

que la memoria titulada **Charge Exchange and knockout reactions induced by Sn isotopes at Relativistic Energies** ha sido realizada bajo su dirección por **Jossitt Williams Vargas Cruz** en el **Departamento de Física de Partículas de esta Universidad**, y constituye el **Trabajo de Tesis** que presenta para optar al **Grado de Doctor en Ciencias Físicas**.

Santiago de Compostela, a 19 de Mayo de 2014

Fdo. José Benlliure

Fdo. Jossitt W. Vargas C.

Contents

Contents	iii
1 Peripheral heavy-ion collisions	3
1.1 Introduction	3
1.2 Experimental challenges and advantages	3
1.3 Theoretical description of relativistic peripheral reactions	4
1.3.1 Microscopical description	5
1.3.2 Macroscopic descriptions	7
1.4 Physics highlights	8
1.4.1 Interaction cross sections and nuclear density distributions	9
1.4.2 Direct reactions	11
1.4.3 Nucleon Knockout	11
1.4.4 Electromagnetic excitations and collective modes	12
1.5 Charge exchange reactions	12
1.5.1 Elastic and Inelastic Channels	13
1.5.2 Low Energy Transitions	14
1.5.3 High Energy Transitions	17
2 Experimental technique	22
2.1 The accelerator facility and the detection setup	23
2.1.1 The GSI accelerator system	23
2.1.2 Beam monitor: SEETRAM calibration	24
2.1.3 Targets	26
2.2 The Fragment Separator FRS	27

2.3	The detection equipment	29
2.3.1	One stage configuration: nuclear reactions using stable beams	29
2.3.2	Two stage configuration: nuclear reactions unstable secondary beams	30
2.3.3	The time projection chambers (TPCs)	30
2.3.4	Plastic scintillators	31
2.3.5	The Ionization chambers (MUSIC'S)	33
2.4	Identification of the reaction residues	34
2.4.1	Determination of the Magnetic Rigidity	34
2.4.2	Determination of the reduced momentum	36
2.4.3	Determination of Atomic number Z	37
2.4.4	Mass-over-charge ratio determination Determination of mass resolution	38
3	Physical Observables	41
3.1	Isotopic identification	41
3.2	Measuring Kinematical Quantities	42
3.3	Recoiling energy of projectile residues	45
3.3.1	Energy transformation of the beam frame	46
3.3.2	Energy resolution	47
3.3.3	Unfolding of the experimental response	49
3.4	Angular distributions	53
3.5	Cross Sections	55
3.5.1	Background subtraction	55
3.5.2	Dead Time	56
3.5.3	Secondary Reactions	56
3.5.4	Ionic charge states	57
3.6	Reactions using secondary beams	58
4	Isobaric charge exchange reactions	60
4.1	Systematic study of charge-exchange reactions	61
4.2	Recoiling energy distributions of projectile residues	63
4.2.1	Comparison with previous experiments	65
4.2.2	Results of reactions using stable beams	68
4.2.3	Results of reactions using unstable beams	72
4.3	Quasielastic channel	74
4.4	Sensitivity to the radial distributions	76
4.5	Excitation of baryon resonances in the nuclear medium	78
4.5.1	Evidences for the excitation of different resonances	78
4.5.2	Model Calculations	88

4.5.3	In-medium production of the Δ resonance	90
4.5.4	In-medium production of the Roper resonance	92
5	Proton Removal Channel	97
5.1	Measurements	97
5.2	Nucleon removal cross sections	101
5.2.1	Model calculations	103
5.2.2	Results and discussion	106
5.3	Missing energy spectra	110
	Conclusions	112
A	Appendix: List of layers in the experiment	115
B	Deconvolution Method applied to the Energy Distributions	119
C	Appendix: Measured Cross Sections	121
	Bibliography	123
	Resumen	130

INTRODUCTION

In this work we propose to make use of peripheral heavy-ion collisions induced by stable and non-stable relativistic projectiles to investigate nuclear and nucleonic excitations in nuclei. We will induce these excitations by means of isobaric charge-exchange reactions and nucleon knockout.

Charge-exchange reactions are spin-isospin transitions which can provide information on the isovector component of the nuclear force. These excitations may take place in two different energy regimes: at low energies, this quasi-elastic charge exchange lead to nuclear excitations (Fermi, Gamow-Teller, spin-dipole, quadruple, giant resonance etc.) and are understood as a virtual charged meson exchange between projectile and target nucleus. At higher energies the process is explained by the excitation of nucleonic resonances and their subsequent decay emitting real charged mesons that escape from the nuclear medium. In the present work, we concentrate on the latter case. We propose then to investigate baryon excitations in asymmetric nuclear matter. The peripheral character of these reactions, imposed by the escaping condition for the emitted mesons, could be used to investigate the relative abundance of protons and neutrons at the nucleus periphery.

In this work, we also investigate nucleon knockout processes. These reactions have been largely used to investigate the single-particle structure and the radial extension of nuclei far from stability. Moreover, we make use of these reactions to investigate nuclear excitations in proton-removal collisions.

The investigation of these processes was done in an experiment at the GSI facilities (Germany). In this experiment, we used stable (^{112}Sn , ^{124}Sn) and unstable (^{110}Sn , ^{120}Sn and ^{122}Sn) tin projectiles accelerated at 1000 AMeV. Systematic study of the energy dependence of charge exchange reactions was performed with a beam of ^{112}Sn at different energies : 1000, 700 and

400 AMeV. In addition, we used different targets (C, CH₂, Cu and Pb) to investigate these reactions according to the projectile isospin, energy and target nature. The projectile reaction residues were identified in atomic and mass number using a high-resolution zero-degree magnetic spectrometer, the Fragment Separator (FRS). This spectrometer also allowed us to measure with high accuracy the longitudinal momentum of the projectile residues. From these measurements, we could define two observables to characterize isobar charge-exchange and nucleon knockout reactions: the cross sections of these reaction channels and the energy lost by the projectile residues.

The missing-energy spectra measured with the FRS for the projectile residues issued in isobar charge-exchange reactions showed two clear components, corresponding to the quasi-elastic charge-exchange and the baryon excitation. Moreover, an accurate deconvolution technique developed in the framework of this investigation allowed us to identify several baryonic excitations: the Δ and Roper ($N^*(1440)$) resonances, and a third one not yet identified. We could also observe a clear dependence of the cross sections of these reaction channels with the neutron excess in the target and projectile nuclei.

The systematic investigation of proton and neutron knockout reactions showed a clear dependence of the cross sections of these reaction channels with the projectile neutron excess: at large neutron excess proton knockout induces larger excitations and vice versa.

The present work is organized as follows: In chapter one, we present the start-of-the-art knowledge on charge-exchange and nucleon-knockout reactions. Chapter two provides a detailed description of the experiment. In chapter three, we describe the observables we use for our investigations. Finally, in chapters four and five, we present our results concerning the investigation of isobar charge-exchange and nucleon-knockout reactions.

CHAPTER 1

Peripheral heavy-ion collisions at relativistic energies

1.1 Introduction

In this introductory chapter we review the state-of-the-art use of relativistic radioactive beams for investigating the structure of atomic nuclei far from stability, in special the experimental techniques and the reactions that provide a better insight into the structure and dynamics of the atomic nucleus. These reactions, in special the peripheral ones, provide us with an important tool to investigate the low nuclear-densities regime and the single particle properties of nuclei. In our review, we focus on charge-exchange and knock out reactions since these are the reactions, we have used in our investigations.

1.2 Experimental challenges and advantages

The availability of fast radioactive beams produced by fragmentation generated a high interest in the investigation of nuclei near the driplines via scattering experiments. High beam energy experiments allow for reaction studies in the regime of short interaction times and small scattering angles. The main experimental advantages are the possibility of using relatively thick targets (in the order of g/cm^2) and the emission of the projectile residues in forward direction that makes full-acceptance measurements feasible with moderately-sized detectors. Moreover, another important advantage of this technique is the clean separation and identification of the reaction prod-

ucts. Further details on the study of reactions with fast radioactive beams of neutron-rich nuclei are presented in [1]. Noteworthy in this respect, in the relativistic energy regime, the theoretical description of these reactions allow to use approximations as the optical limit of the Glauber model [2, 3, 4], adiabatic approximation [5, 6]. The experiment analyzed in this work are based in the inverse kinematics technique. In this case the reaction products are emitted forward and can then be analyzed with an a zero-degree magnetic separator. In our case we make use of the FRagment Separator (FRS); details about this experimental set up will be described in chapter 2. The inverse kinematic technique also allow to produce from stable projectiles secondary beams that emerge from the production target with a velocity close to that of the projectile. In most cases, the nuclear reaction mechanism determines the kinematic properties of the reaction products such as average energy, energy spread, and angular distribution. Using the first stage of the magnetic separator it is possible to select all ions with the same mass-to-charge ratio; for bare fragment ions this is equivalent to a separation in A/Z . The A/Z resolution is sufficient in most experiments where the particles are identified event by event using time-of-flight (ToF) and position measurements. With the ToF value it is possible to determine the velocity while the position information it is related with the magnetic rigidity. The position and ToF were measured at the dispersive plane of the magnetic separator. There is a third measurement, which is the atomic number obtained from energy loss measurements in an ionization chamber, scintillator or solid state detectors. Using these measurements, it is possible to determine the isotopical identification of each fragment. In addition, using the magnetic rigidity it is possible to determinate kinematical quantities as the longitudinal momentum of the residues produced in a reaction as will be presented in chapter 2.

In the next chapter we will describe the experimental technique and in chapter 3 we will explain how do we obtain of the physical observables: the cross section and the energy distributions using the inverse kinematic at relativistic energies.

1.3 Theoretical description of relativistic peripheral reactions

The increment of experimental data on fragmentation extend the knowledge on nuclear properties such as nuclear level densities and nuclear dynamics. Many physical observables allow us to known the parameters that characterize a reaction like the cross section and the momentum energy dis-

tribution.

The inelastic nuclear reactions at relativistic energies occur in two steps that take place at different time scales. The first step is an offhand reaction that may modify the composition of the reaction participants and introduces a certain amount of excitation energy and angular momentum. The typical time of this reaction step is several times 10^{-23} s. Several models describe the first step of the fragmentation process namely the intranuclear-cascade model [7] and the abrasion model [8].

The second stage is the de-excitation of hot pre-fragments produced during the reaction. This stage is described using a statistical model as will be explained in the chapter 5.

1.3.1 Microscopical description

In the microscopical description of fragmentation, we can stand out intranuclear cascade and Glauber models. Intranuclear Cascade models (INC) use Monte Carlo methods and the evolution of the INC models was performed by the work of Metropolis [7] and Bertini [9]. The INC codes calculated the nucleon removal as a series of individual nucleon-nucleon interactions in a classical way with Pauli blocking considerations.

Intra-Nuclear Cascade codes: INC

Intranuclear cascade codes described the fragmentation problem at microscopical level. The microscopic calculations concerning the first stage of the reactions, can be performed with the so called intra-nuclear cascade (INC) models [10, 11, 12, 13]. At relativistic energies the nucleon-nucleon sequential interactions may be considered as intra-nuclear cascade interactions rather than interactions in the mean-field. This assumption is used in the INC codes briefly introduced here, which can be considered as transport codes of hadrons within the nucleus.

Typically there are two types of INC codes, depending on the treatment of the nuclear medium: the Bertini-like codes [9], where the nuclear density is considered continuous; and the Cugnon-like codes where the nucleons are treated individually particles. The nucleon-nucleon interactions are defined from free-NN cross sections. The cascade is initiated by the nucleon of the projectile hitting somewhere on the target sphere (only the radial density dependence is considered).

Versions of Liège intranuclear cascade (INC) ([10, 11] and references cited therein) add new features: a) modifications in the diffuse nuclear surface.

b) the Pauli blocking is improved c) pion dynamic is improved in special the Δ lifetime.

Glauber model

The Glauber model and the transport equation are the popular techniques for studying the nuclear scattering at high energies.

The Glauber model [2], in its basic form, is a quantum mechanical description using eikonal wave functions in order to describe the scattering at high energies.

Moreover, in some cases the results can be interpreted in terms of the mechanic of nucleon-like rigid balls in a semiclassical approach.

But it is important to note that the term *Glauber* can be used in a broad context namely used in the probability concepts based on the nucleon's mean free path and forward scattering or when quantum mechanical method based on eikonal wavefunctions are used.

The theoretical study of the nucleon removal reaction is possible using the eikonal theory. In this model, several reaction mechanisms are considered to participate in the two-nucleon removal: the inelastic removal of both nucleons, the elastic removal with one of them; the inelastic removal of the second, and the elastic removal of both nucleons. For more details on the reaction model [14, 15].

Glauber model offers an alternative explanation at the problem of the fragmentation by a different point of view. The interaction process is described in terms of nucleon-nucleon collisions. The probability of the occurrence of n nucleon-nucleon collisions with an impact parameter \mathbf{b} is given in the following equation:

$$P(n, \mathbf{b}) = \binom{AB}{n} [T(\mathbf{b})\sigma_{NN}]^n [1 - T(\mathbf{b})\sigma_{NN}]^{AB-n} \quad (1.1)$$

The first term is the number of combinations for finding n collisions out of AB possible nucleon-nucleon encounters where A or B is the number of nucleons in the nucleus A or B . The second term of this equation is the probability of having exactly n collisions, while the last term is the probability of having $AB - n$ misses. $T(\mathbf{b})$ is the thickness function for the collisions defined as the probability of have a nucleus-nucleus collision within the transverse element area $d\mathbf{b}$. This thickness function is normalized and it is possible to relate it with the corresponding thickness function for the nucleon-nucleon collision using the following equation:

$$T(\mathbf{b}) = \int \rho(\mathbf{b}_b, z_b) d\mathbf{b}_b z_b \rho(\mathbf{b}_a, z_a) d\mathbf{b}_a dz_a t(\mathbf{b} - \mathbf{b}_a - \mathbf{b}_b) \quad (1.2)$$

1.3 Theoretical description of relativistic peripheral reactions 7

where $\rho(\mathbf{b}_a, z_a)$ is the probability of finding a nucleon in the transverse area $d\mathbf{b}_a z_a$ and the $t(\mathbf{b})$ function is defined by the normalization condition:

$$\int t(\mathbf{b})d\mathbf{b} = 1$$

The total probability is the sum of the all possibles probabilities of the occurrence of n nucleon-nucleon collisions and is given by the following equation:

$$\frac{d\sigma}{d\mathbf{b}} = \sum_{n=1}^{AB} P(n, \mathbf{b}) = 1 - [1 - T(\mathbf{b})\sigma_{NN}]^{AB} \quad (1.3)$$

The total cross section σ^{AB} of the interaction nucleus-nucleus is given by the following equation:

$$\sigma^{AB} = \int d\mathbf{b} \{1 - [1 - T(\mathbf{b})\sigma_{NN}]^{AB}\} = 2\pi \int bdb \{1 - [1 - T(b)\sigma_{NN}]^{AB}\} \quad (1.4)$$

In its basic form in the quantum mechanical description using eikonal wave functions in order to describe the scattering at high energies. Moreover, in some cases the results can be interpreted in terms of the mechanic of nucleon-like rigid balls in a semiclassical approach.

1.3.2 Macroscopic descriptions

At macroscopical level, the Abrasion model [8, 16, 17, 18] describes the fragmentation between the target and projectile. If the velocity of the particle beam is higher than the Fermi velocity of the potential well, nucleon-nucleon collision are restricted by the overlapping volume between projectile and target. In the geometrical point of view, it is possible to define the interaction zone where nucleons of projectile and target with the name of *participator*. In addition the non-overlapping zones are named *spectator* where part of nucleons of projectile and target keep on moving almost undisturbed with their initial velocities. Using approximate numerical methods it is possible to calculate the overlap zone. In this way, the mass number of the projectile prefragments is determined as a function of the impact parameter as well as its production cross section. The geometrical model suggested in[19] had been justified using Glauber-type calculations [2]. It is possible to distinguish two stage in the fragmentation using a macroscopical model: the abrasion and ablation. In the first stage, the abrasion was described above like a shearing off of volume in the participants in the reaction process, on other

hand, the ablation is the energy loss due to excitation resulting from the collisions into evaporated particles.

The abrasion-ablation can predict the nucleon removal and this model could show some systematic deviations from the experimental data attributed to an underestimated excitation energy of the prefragments but this subject will be discussed in the chapter 5 .

Abrasion codes: ABRABLA

ABRABLA [20] is an abrasion/ablation code developed to described projectile fragmentation reactions at relativistic energies. In the first stage of the collision (abrasion), the number of removed nucleons is determined by the volume of the overlapping zone between projectile and target nuclei defined by the the impact parameter. During the abrasion process certain number of nucleons are removed producing vacancies (holes) in their Fermi distribution.

From the number of removed nucleons and their nature (neutrons or protons), the code must determines the initial conditions for the subsequent evaporation stage (ablation) , that is mass number, neutron excess, excitation energy and angular momentum of the pre fragments. The N/Z ratio of the pre fragments is calculated according to the hypergeometrical model , where there is no correlation at all between the nucleons during the abrasion, that is, each nucleon has a statistical chance to be neutron or proton.

All of these features are implemented in the code ABRABLA, and a discussion about the results obtained with this code and its comparison with the tin beam fragmentation products will be presented in the chapter 5.

1.4 Physics highlights

Nuclear reactions are a common tool to learn about the structure and dynamics of nuclei. The arrival of radioactive intensive beams (RIB) extended these kind of investigations to this new exotic species. In some cases the application of these techniques was not possible and new observables extracted from novel experimental approaches needed to be introduced. The determination of bulk properties such as nuclear size and density distributions have been used to constraint the nuclear potential and the nuclear structure (single particle properties). The evaluation of these properties has been done in the past, for stable nuclei, through proton (nucleon distribution) and electron scattering, and isotope-shift measurements (proton distribution). The use of direct reactions was also much extended to learn about the nuclear structure. Typically elastic and inelastic scattering and few nucleon transfer reactions

were the preferred methods to obtain this information. Coulomb excitation was also employed to both learn about the nuclear structure, namely single-particle properties but also the collective excitation modes associated to some nuclei. We will highlight in the next section the most relevant experiments that have been performed to extend this kind of investigations to unstable nuclei. This selected summary intends to provide a general idea of the status of art achieved in the use of nuclear reactions with RIB.

1.4.1 Interaction cross sections and nuclear density distributions

The study of nuclear size and matter density distribution are among the first properties to determine experimentally. In stable nuclei, we have learnt that proton and neutron distributions are very similar, however for unstable nuclei they have probed to be very different. Interaction cross-sections (σ_I) were the first experiments performed with RIB at Lawrence Berkeley National Laboratory (LBNL), at relativistic energies, at the end of last century (1980's). The pioneer experiment performed by Tanihata and collaborators [21] where very large interaction cross-sections were measured for neutron-rich short live nuclei produced by fragmentation and detected in-flight, is still today very important since allowed the experimental discovery of unusual properties associated to the matter density distributions of the later known as halo or neutron skins. The comparative analysis of density distributions for stable and unstable nuclei allowed to discover the identified neutron skins and halos. The term neutron halo[22, 23, 24] describes an excess of neutrons at the nuclear surface. It corresponds to a dramatic change at the surface of the neutron density distribution associate to the development of an extended very low density tail. The rms associated to this distribution is very large compared with neighbor isotopes that do not exhibit this phenomenon. The interest on the study of halo nuclei is large. The phenomena was discovered in nuclei near the drip lines, but considering that the neutron drip line is reached only up to oxygen the potential is large. Some works predict the existence of halo with than two neutrons in heavier elements. These early experiments were followed by an important collection that applied the method for elements up to argon. These experiments have been performed at the FRS at GSI and are compiled in [25].

At intermediate energies the contribution of inelastic channels can be important. In this energetic regime the reaction cross-section ¹ measure-

¹The reaction cross-section includes the sum of interaction cross-section and inelastic scattering channels

ments were largely employed. There is an important compilation for stable nuclei [26], latter completed for RIB with many experiments addressing the determination of reaction cross-sections at GANIL[27, 28, 29, 30], MSU [31, 32, 33],RIKEN[34, 35] and RIBLL[36].

The goal of all these works on unstable nuclei was the determination of matter density distributions. This task is far to be easy since we do not have any model- independent approach to do it. The most widely accepted method is the use of Glauber model that following a rather geometrical approach allows to connect nuclear matter radius with the measured cross-sections. In the most basic version (the optical limit), the model needs to be feed with known densities distributions. In the case of stable nuclei, the determination of charge distributions was achieved using electromagnetic probes such as electron scattering and muonic atoms [37]. The neutron distribution were assumed to be identical and thus root mean square radii could be extracted.

The natural extension of this kind of studies to short-live nuclei is not so direct. In one hand, electron scattering of unstable nuclei is nowadays not possible since they will demand colliding experiments (i.e: ELisE at FAIR) that are not yet available. On the other hand we know that the neutron density distribution cannot be assumed to be identical to the proton one, particularly for those species exhibiting halos or pronounce neutron skins. There exist other methods to measure the charge distribution using of the isotope shift method allowing to determine the charge radii (rms) with high accuracy, but this is experimentally restricted restricted to very light neutron-rich isotopes[38, 39, 40, 41, 42]. As an alternative method the charge-change cross-section (σ_{CC}) determination was used since the first days of the RIB studies [21]. The interpretation of this observable in the framework of the Glauber model [43] allows, with this time moderate precision, the determination of proton radii. The method was employed in the 80's with stable beams [44] and later extended for short live species [45, 46, 47, 48].

The determination of proton radius is of extreme interest in the study of nuclear halos and skins, since they are necessary to correct the nuclear matter distribution and extract the neutron contribution. The determination of thickness of neutron skin is also a sensitive ways to determine the equation of state (EOS) of asymmetric nuclear matter, of uppermost importance to understand stellar objects (e.g: neutron stars and supernovae). Neutron skin thicknesses are then determined combining the matter radii determined by interaction cross-sections and proton distribution radii deduced from charge radii. A very complete compilation of the results (σ_I and σ_{CC}) obtained are presented in [25].

1.4.2 Direct reactions

Direct reactions are a very powerful tool to investigate the nuclear structure. They are rather fast and involved very few nucleons and very low momentum transfer (e.g: elastic and inelastic scattering, transfer, knock-out etc.). In this work we will concentrate on direct reactions at relativistic energies with special emphasis to nucleon knock-out. There are recent review articles that discuss this subject in detail [1, 49, 50], even though the most relevant highlights will be mention in the following subsection.

1.4.3 Nucleon Knockout

Knockout experiments in inverse kinematics started in the 90's [51] and since then a really important number of experiments have been performed in different medium and relativistic energy facilities (e.g: NSCL/MSU, GANIL, RIBF, and GSI see [50, 52] and references therein). A relativistic secondary beam impinged on a light target and as a result of the interaction the A-1 fragment emerges from the target and continues its path with an almost unaffected velocity. The first experiments were not selective on any de-excitation of the remaining fragments after the knockout (after the reaction only the heavy emerging fragment was detected), but soon it became obvious the interest of performing selective experiments to gain in accuracy.

The general goal of these experiments is to provide spectroscopic information on unstable nuclei. The main observables are the momentum distribution of the remaining fragment (A-1 after the reaction) and the associated cross-section. The first one is directly related to the angular momentum content of the removed nucleon and thus to the spacial extension of the unstable nucleus. Moreover and according to a single-particle picture both the momentum distribution and the cross-section, define the nuclear structure of the unstable nuclei under study. This connexion is model- dependent and needs a detailed description of the reaction mechanism along with an adequate nuclear structure input. The first experiments focused on the study of light halo states, and they are still the best examples to illustrate the power of the experimental technique. A very detailed description of the structure of the neutron ^{11}Be and proton halo ^8B can be found in [53, 54] respectively. These first works were later extended to other species (e.g: heavier nuclei, neutron-deficient nuclei, deeper bound states, two-nucleon removal) and brought very interesting information on the structural changes experimented by the nuclei with the isospin (see the recent compilations [55, 56]). They have been also used to benchmark different nuclear structure interactions [57, 58]. At present, the use of knockout reactions to determine experimental spectro-

scopic factors are subject of strong debate in the nuclear physics community [59]. Recent experiments addressing Quasi Free Scattering reactions induced by relativistic ion beams on light (proton) target have been performed in several facilities. They will complement the results so far obtained with knockout reactions. At the same time they would allow to extend this kind of studies to the inner part of the nuclei. This subject will be one of the selected topics of the future R3B experiment at the FAIR facility.

1.4.4 Electromagnetic excitations and collective modes

Electromagnetic processes at relativistic energies give constitute an interesting source of nuclear-structure information, particularly when they address exotic nuclei [60]. At these energies (~ 1 GeV/nucleon), collective nuclear states at low and at high excitation energies are excited in peripheral heavy-ion collisions with large cross sections. The realization of experiments with minimum beam intensities is possible and surface vibrations and particular giant resonances can be studied. GSI was pioneer in the study of electromagnetic excitation, in both stable and unstable nuclei, of the giant dipole resonance induced by high-energy beams on targets with large Z [61]. For the unstable nuclei, particularly neutron-rich isotopes, low-lying strength appeared at energies near the neutron threshold. This new low-lying strength distribution (E1) was latter known as Pygmy Dipole Resonance (PDR) [61, 62, 63, 64, 65, 66].

On the other hand, the Coulomb breakup (induced by the presence of heavy targets) is also an experimental method to explore single-particle properties of halo- nuclei, as it was the case of [67, 68, 69].

It is also important to mention the interest of using the Coulomb dissociation method to extract (p, γ) or (n, γ) reaction rates, which essentially determine the astrophysical r , and rp -reaction paths. While the direct measurement of these rates is very difficult, the (γ, p) and (γ, n) reaction can be measured by electromagnetic excitation (heavy target) using high-energy secondary beams [70, 71, 72] which is the time-reversed process. This allows to achieved higher luminosities through the use of thicker Pb break-up targets. The method benefits also of larger acceptance of the reaction products due to stronger forward focussing (relativistic inverse kinematics).

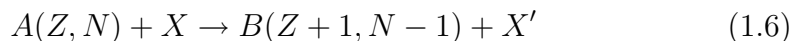
1.5 Charge exchange reactions

These reactions are represented by the change of the isospin operator τ and could also affect the spin.

In isobaric charge-exchange reaction processes the projectile changes its charge but without altering its initial mass number (A). A typical charge-exchange reaction can be illustrated by reactions (n, p) or (p, n) . In the first case, the reaction (n, p) , a neutron the projectile interacts with the target exchanging its charge. This process can be represented by following form:



where X represents the target, $B(Z - 1, N + 1)$ is the nucleus produced in the reaction. In the analogous way, for the relation (p, n) it is a possible to find the reaction:



In this case, the nucleus produced in the charge exchange reaction, $B(Z + 1, N - 1)$, has an additional proton, but a neutron less. The charge exchange reaction guards a great similarity with the β decay. Apart from the dynamics of the dispersion, the principal difference between the charge-exchange reactions and the β decay, it is that in the charge exchange reactions the (p, n) and (n, p) channels are not restricted by considerations of the value Q of the reaction to the final conditions (that are lower in energy for the decay β).

To produce the charge exchange reactions the experiment used different projectiles like electromagnetic, leptonic and hadronic probes. It is possible to use light and heavy ions as a probe in order to induce charge exchange reactions, but in this case the theoretical approach it is more complicated. With pions and heavy ions it is possible to study the double charge exchange reaction. In such reactions a couple of nucleons changes its charge at the same time. These useful reactions are sensitive to two-body correlations in the nuclei and this information is closely related to obtained using two-nucleon transfer reaction and also is related to double β -decay [73, 74, 75].

Charge exchange reactions are a useful tool in the analysis of the nuclear structure. The (n, p) and (p, n) channels are often used to obtain the Gamow-Teller matrix elements, which can not be extracted from β -decay experiments (see for example [76, 77]). At intermedium and high energies, above of a pion mass threshold, it is possible to excite a Δ resonance. In isobaric charge-exchange reactions, the real pion produced in the inelastic channel must escape in order to preserve the isobar feature of this reaction.

1.5.1 Elastic and Inelastic Channels

Using isobaric charge-exchange reactions it is possible to distinguish the number of neutrons and protons in the nuclear periphery, since the pro-

duction of this reaction at relativistic energies takes place by means of two channels. The quasi-elastic channel corresponds to charge exchange low energy spin-isospin transitions and the inelastic channel corresponds to nucleon excitations.

The inelastic channel has been observed when the reaction has enough energy to create the Δ resonance, about the average energy of 300 MeV. The probability of the inelastic channel and the production of Δ isobars and its respective decays is described by the isobaric model [78] and [79]. In the case of isobaric charge exchange reactions, the inelastic channel corresponds to nucleon-nucleon collisions in the nuclear periphery leading to a cold residual nucleus, without energy excitation. The Δ and other possible nucleon excitations decay and the emitted pion must escape of the nucleus in order to preserve the isobaric feature of this reaction.

1.5.2 Low Energy Transitions

In the low energy regime, nuclear collective excitations are produced. In the quasi-elastic channel corresponds to Gamow-Teller transitions, spin-dipole, spin-quadrupole and other excitations below the production of a pion threshold. The elemental isovectorial transitions ($\Delta T = 1$) with $\Delta T = 1$ generated in the charge exchange reactions depend on other physical factors like a spin flip ΔS and the angular momentum ΔL . Low energies transitions are summarized in the following:

- Fermi Transitions: $\Delta T = 1, \Delta S = 0, \Delta L = 0$
- Gamow Teller Resonance (GTR): $\Delta T = 1, \Delta S = 1, \Delta L = 0, \sigma\tau$
- Spin Dipole Resonance (SDR) : $\Delta T = 0, 1, \Delta S = 1, \Delta L = 1, \sigma\tau$
- Giant Dipole Resonance (GDR) : $\Delta T = 0, 1, \Delta S = 0, \Delta L = 1, \tau$

The charge exchange reactions at low energies have their origin in virtual pion exchange, where the pion changes the charge of the reaction. The diagram 1.1 represents the charge exchange reaction process in the quasi-elastic energetic region in the reaction $^{112}\text{Sn}(Pb, X)^{112}\text{Sb}$.

Figure 1.2 shows the energy dependence of the isospin (τ) and spin-isospin ($\sigma\tau$) transitions as a function of energy. At relativistic energies regime used in the present dissertation, we can observe that it is more probable to produce ($\sigma\tau$) excitations as GTR and SDR than Fermi Transitions and GDR excitations.

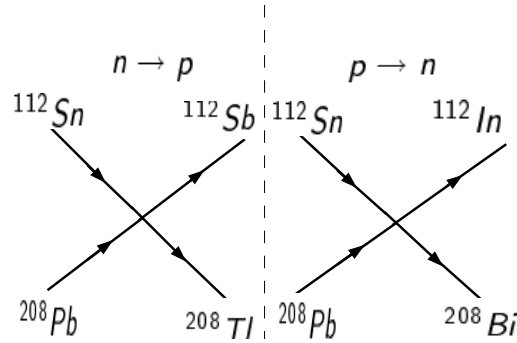


Figure 1.1: Schematic diagram for the charge exchange reaction in the quasi-elastic peak for the $n - p$ and $p - n$. This process is mediated by a virtual pion exchange.

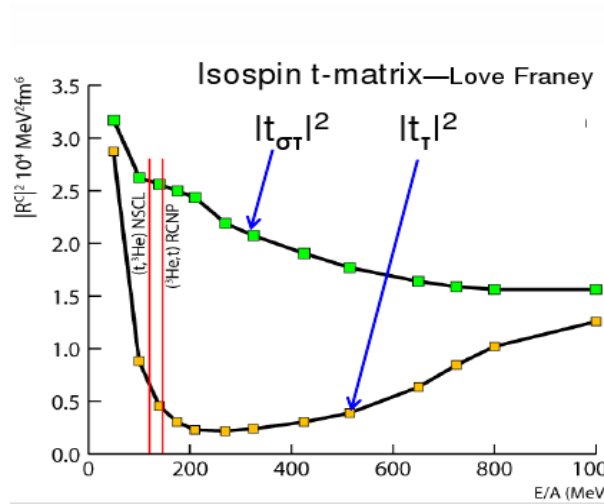


Figure 1.2: Energy Dependence of each isovector transition calculated in [80].

Depending on the angular momentum involved in the reaction, each isovector transition has a maximum position in the cross section at different angles (see the figures 1.3 and 1.4). For example in $^{90}\text{Zr}(p, n)^{90}\text{Nb}$ transitions like IAS and GTR which has a peak in the angular distribution at 0° correspond to $\Delta L = 0$ and the SDR transitions correspond to a peak around $\sim 5^\circ$ with $\Delta L = 1$ and high momentum transitions $\Delta L > 1$ [81]

The Gamow Teller (GT) resonance is a nuclear collective spin-isospin oscillation in which the nucleons coherently change their spin and isospin direc-

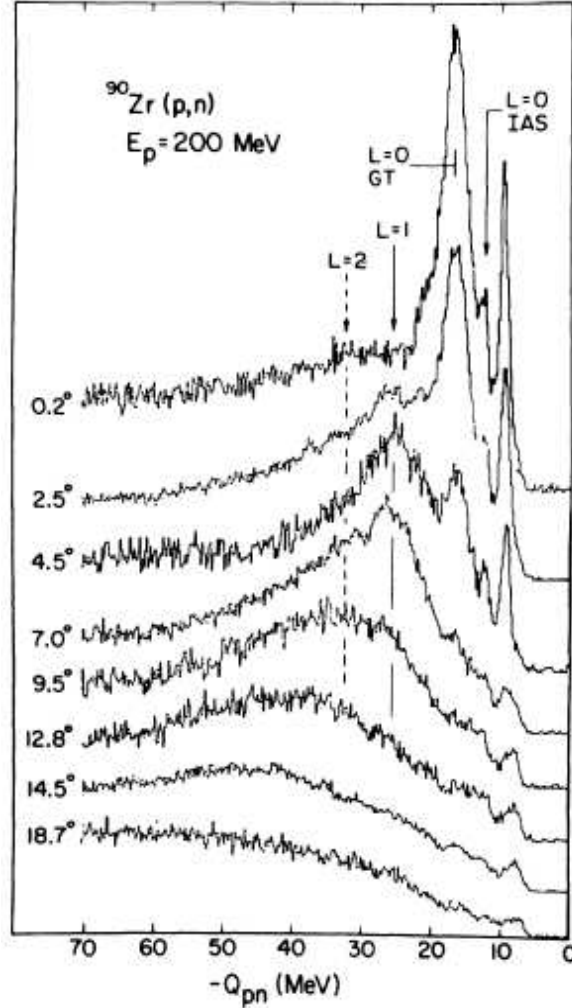


Figure 1.3: Neutron spectra at $E_p=200\text{MeV}$ for $^{90}\text{Zr}(p,n)^{90}\text{Nb}$ reaction at different scattering angles (from [81]). In this plot it is clear that the angular dependence and the different excitation energy of each isovectorial transition in the quasi-elastic region.

tions without changing their orbital motion. In 80s decade, the spin-isospin correlation was understood after the (p,n) charge-exchange experiment was carried. These experiments demonstrated the existence of collective spin-isospin modes in the nuclei (see [81, 82, 83]). The collective mode was predicted in 1963 by Ikeda, Fujii and Fujita [84] who predicted the existence of the GT. The β decay has limited access to nuclear states in a small energy window. Therefore, using hadronic probes such as proton, neutrons or

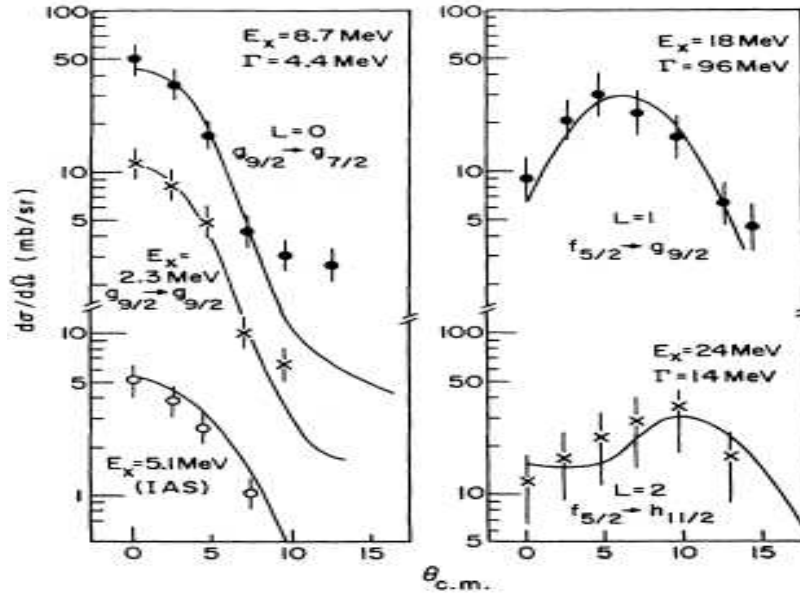


Figure 1.4: Angular distributions from the $^{90}\text{Zr}(p,n)^{90}\text{Nb}$ reaction for different excitation energy regions. From [81].

light and heavy ions in charge exchange reactions, it is possible to have a complete map out response function in the $\sigma\tau^\pm$ channels. The (p,n) reaction is connected to the β decay only if the GT cross section is measured at low momentum transfer $q \sim 0$. This condition is fulfilled only for zero degree scattering and high beam energies. This means that the transfer angular momentum (L) is equal to zero, then the orbital motion of the nucleons is unchanged. The GT resonance is characterized by broad peak with the width of about 4 MeV in all heavy-mass nuclei.

1.5.3 High Energy Transitions

Nucleon Resonances

In the quark model picture, the resonances correspond to spin, isospin or spin-isospin states of a nucleon quark system. Nucleon resonances are excited states of nucleon particles with extraordinarily short lifetimes ($\sim 10^{-24}\text{s}$). According to the constituent quark model [85], the nucleon is a ground state

of the quark triplet. At relativistic energies it is possible to excite this basic state in baryon resonances, as shown in the figure 1.5 . This resonant states could be isoscalar transitions with $\Delta T = 0$ associate with mesons σ, η or isovectorial transitions with $\Delta T = 1$ through π and ρ mesons exchange.

Δ Resonance

The delta resonance (Δ) is the nucleon resonance with the lowest energy at 1232 MeV . In a quark picture of baryons it can be viewed as the internal spin-isospin flip excitation of the nucleon. The Δ resonance has an isospin multiplet which has the symbols $\Delta(1232)^{++}$, $\Delta(1232)^+$, $\Delta(1232)^-$, and $\Delta(1232)^0$ and electric charges $+2$, $+1$, $+0$ and -1 respectively.

Table 1.1 shows of the Δ resonance properties taken from Particle Data Group [86].

Breit-Wigner Mass (MeV)	Breit-Wigner full width (MeV)
1231 to 1233 (≈ 1232)	116 to 120 (≈ 118)

Table 1.1: Breit-Wigner mass and width of the Δ resonant [86].

The $\frac{3}{2}$ spin means that all the three quarks inside a particle have their spin axis pointing in the same direction, unlike the nearly identical proton and neutron in which the intrinsic spin of one of the three constituent quarks has a different spin orientation. This spin alignment is complemented by an isospin quantum number of $\frac{3}{2}$ which differentiates the Δ^+ and Δ^0 and ordinary nucleons, which have spin and isospin of $\frac{1}{2}$. All varieties of Δ quickly decay via the strong force into a nucleon (proton or neutron) emitting a pion of appropriate charge.

Δ mass shift

An important energy shift ($\sim 70 \text{ MeV}$) is observed by comparison between the Δ -resonance excitation in proton in nucleus-nucleus collisions (see [87, 88] and references therein). The investigation of the Δ -resonance excitation in (p,n) and ($^3\text{He}, t$) charge-exchange reactions has revealed how this process is affected by nuclear in-medium effects. The main observation is a downward energy shift of the Δ -resonance peak position by around 70 MeV when using heavy targets ($A > 10$) as compared to the mean energy of the Δ resonance produced in free nucleon nucleon collisions [87, 88].

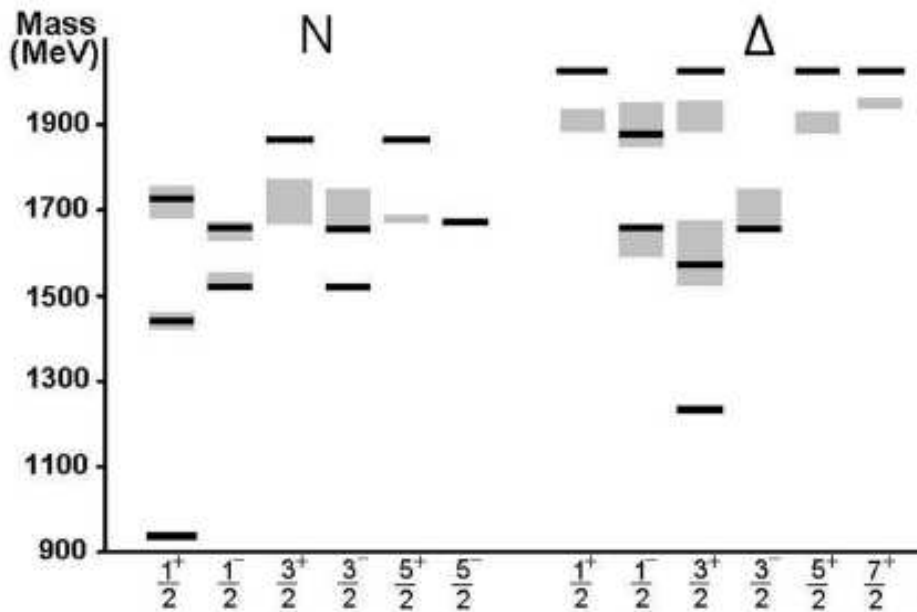


Figure 1.5: Baryon resonances and its experimental masses from PDG for 4^* and 3^* resonances. The black lines correspond to calculated values using constituent quark model [85] and the green boxes correspond to the experimental masses. Transition with $\Delta T = 0$ require scalar meson (σ, η) and $\Delta T = 1$ require such as π or ρ mesons.

Further experiments investigating the Δ -resonance excitation in charge-exchange reactions using heavy ion collisions also have shown a clear dependence of the magnitude of the downward energy shift in the Δ resonance with the mass of the target nucleus. In these experiments, performed at the Laboratoire National Saturne in France, the longitudinal-momentum of projectile residues produced in isobar charge-exchange reactions was measured with the spectrometer SPESIV with a typical resolution $\Delta p/p = \pm 7 \times 10^{-4}$ [89, 90].

More recently, it was demonstrated that the magnetic spectrometer Fragment Separator (FRS) [91] at GSI (Darmstadt) can also be used for this purpose. In this case, a ^{208}Pb beam at 1A GeV was used to induce isobaric charge-exchange reactions in proton, deuterium, and titanium targets, leading to the production of ^{208}Bi . The recoiling nuclei were isotopically identified with the FRS. The corresponding longitudinal-momentum distributions showed two components that were associated to quasi-elastic and inelastic charge-exchange reaction channels as previously discussed.

The quasi-elastic channel peak corresponds to Gamow Teller transitions. The inelastic channel in isobar charge exchange reactions is understood to be due to the excitation of a Δ resonance in a nucleon nucleon collision, where the subsequently emitted pion escapes from the nuclear medium. Because of the large pion absorption cross-section, these processes correspond most likely to extremely peripheral collisions. Under such conditions, one can expect that the properties of the excited Δ resonance could provide not only information on the in-medium modifications of the hadron masses, but also on the nucleon–nucleon cross section at low densities. Moreover, at GSI one can produce beams of nuclei far from stability. Measuring the properties of the excited Δ resonance in isobaric charge-exchange reactions induced via projectiles with a different neutron excess, one could expect to deduce information on the isovector component of the nuclear force.

Roper Resonance

The roper resonance is a nucleon monopole excitation ($L = 0$) excitation. This resonance appears at about 1440 MeV [92]. In 1963, in a partial-wave analysis performed at Lawrence Livermore National Laboratory, L. D. Roper found a P11 resonance [93]. The result was surprising as there were no hints for such a state and the P11.

Considerable uncertainties are apparent, specially in the full Breit-Wigner width and the branching ratios to the strong-decay channels. Indeed, different values are obtained with different models. The table 1.2 shows the estimates values of the Roper resonance properties are summarized in the

take from Particle Data Group [86]

Breit-Wigner Mass (MeV)	Breit-Wigner full width (MeV)
1420 to 1470 (≈ 1440)	200 to 450 (≈ 300)

Table 1.2: Breit-Wigner mass and width of the $N(1440)$ (Roper) resonant [86].

CHAPTER 2

Experimental technique

In this chapter we will present the experimental approach followed to investigate charge exchange and knockout reactions induced by several tin isotopes on different targets. The experiments are based on the use of the inverse kinematics technique using the relativistic heavy-ion beams produced at GSI.

In the inverse kinematics the projectile products are emitted forward and can then be analyzed with an in-flight magnetic separator. In our case it is the FRagment Separator (FRS). The beam is monitored on the SEcondary Electron TRAnsmssion Monitor SEETRAM and it is focused onto the different targets in each case. The optical features of the Fragment Separator (FRS) and the high quality of detection guarantees the unambiguous separation and identification according to mass and charge.

With the inverse kinematics it is also possible to produce secondary beams of exotic nuclei using fragmentation reactions. In the two-stage configuration of the FRS the first section of the spectrometer is used to produce a secondary beam while the second stage allows to analyze the reaction products of these exotic nuclei.

Using the FRS it is possible to measure with high accuracy the atomic and mass number of each fragment. In addition, it is possible to determine the cross section, the recoiling energy and the angular distribution of the reaction residues.

In the present work, the charge exchange and knockout reactions are produced by different isotopes of Sn at different energies (GeV/u) impinging on different targets (2.1 and 2.2) These reaction channels are investigated

by measuring their isotopic production cross section and recoiling energy distributions.

The experiment was divided in two parts: First, the production of charge exchange reaction yields using stable beams (^{124}Sn and ^{112}Sn) at 1 A GeV. Secondly, we studied reactions with unstable tin isotopes (^{122}Sn , ^{120}Sn and ^{110}Sn).

2.1 The accelerator facility and the detection setup

In this section we provide a general description of the experimental facility used in this work, beginning with a brief description of the beam acceleration and its monitoring.

The experiment was performed at the GSI facilities in Darmstadt, Germany. Using the GSI accelerators it was possible to accelerate heavy-ions at relativistic energies with high intensities (over 10^7 ions/s). The identification of heavy ions at relativistic energies requires a high resolution detection system.

2.1.1 The GSI accelerator system

The GSI accelerator system was used to produce beams of relativistic energies and high quality. The acceleration system at the GSI (see Fig 2.1) consists in three stages: first stage, the MEVVA ion source was used to produce $^{112,124}\text{Sn}$ ions. The second stage is the linear accelerator UNILAC (Universal Linear Accelerator) and the beam is conducted to the third stage.

The third stage of the acceleration system is the synchrotron accelerating ring [94]. This ring consists of 12 cells each one contains two dipoles, a focus quadrupole and a set of sextupoles in order to correct the chromatic aberrations. This set of cells forms the SIS ring with a perimeter of 216 m. The complete set of acceleration system provides very intense beams, necessary for studying the charge exchange and knockout reactions.

For this experiment the beam intensity was about 10^8 particles/spill for ^{124}Sn and 7×10^7 particles/spill for ^{112}Sn . Figure 2.1 represents a schematic view of the GSI (Darmstadt) experimental halls. In this representation it is possible to identify the three acceleration stages, the ion sources, the UNILAC and SIS and the experimental halls, in particular the Fragment Separator (FRS.)

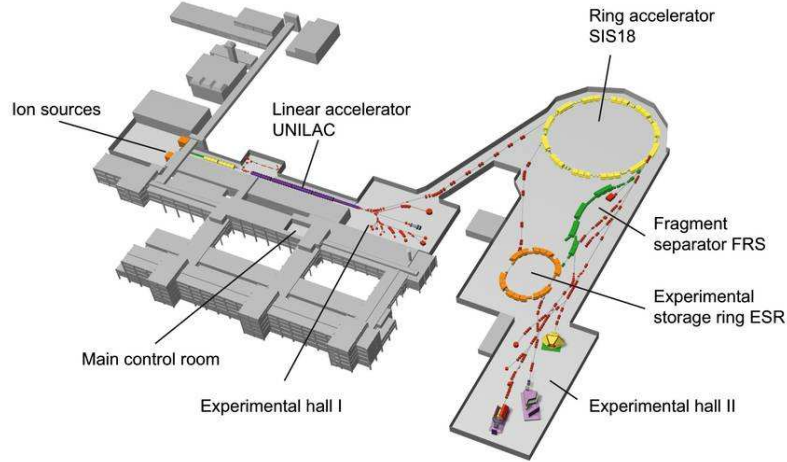


Figure 2.1: Schematic view of the GSI (Darmstadt) experimental halls. In this representation it is possible to identify the three acceleration stages, the ion sources, the UNILAC and SIS and the experimental halls, in particular the FRagment Separator (FRS).

2.1.2 Beam monitor: SEETRAM calibration

To measure a cross section it is necessary to monitor the number of particles impinging on target. The monitor used in this work was the SEcondary Electron TRANsmssion Monitor (SEETRAM) [95]. This monitor consists of three aluminum foils with $10 \mu\text{m}$ thickness that was arranged in the perpendicular direction of beam propagation. Two of these foils are connected to the a voltage of $+ 80 \text{ V}$ and the central foil is connected to the ground. When the beam particles pass through the central foil, it generates secondary electrons in the surface. These electrons are collected in the outer foils by the influence of the applied voltage. The analogous output signal is digitized and then recorded in a scaler. Figure 2.2 represent a beam profile as a function of time measured for this experiment with the beam monitor SEETRAM. The typical spill structure is clearly observed. The background due to the dark current of the detector is also observed this background must be subtracted in order to obtain the real number of beam projectiles.

To determine the number of impinging beam particles it is necessary to calibrate the seetram units to the number of particles [96]. The calibration was done by comparing the signals of the SEETRAM with the signals of a plastic scintillator. The calibration curve appears in figure 2.3, where the

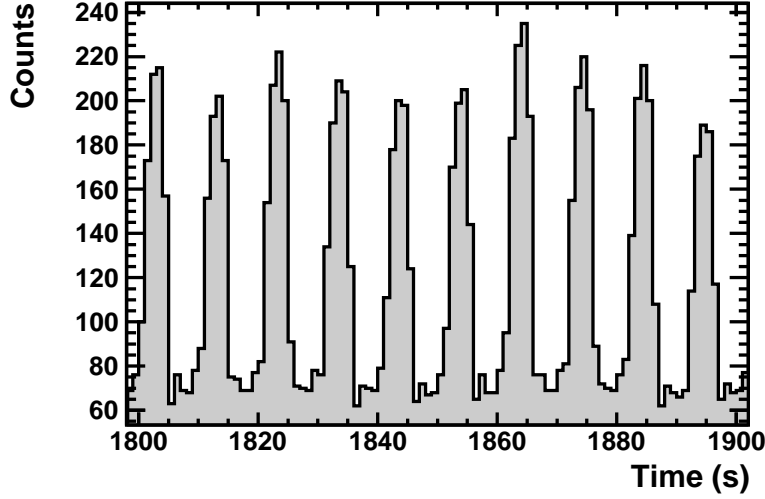


Figure 2.2: Beam profile as a function of time for this experiment measured with the beam monitor SEETRAM. The typical spill structure is observed. The background is observed also due to the dark current of the detector is also observed.

curve corresponds to a linear fit in the range of low intensities. The slope calibration factor of this linear fit is of $f = 855.4 \pm 21.4$ particles/SEETRAM. The number of particles N_{beam} is obtained using the following expression:

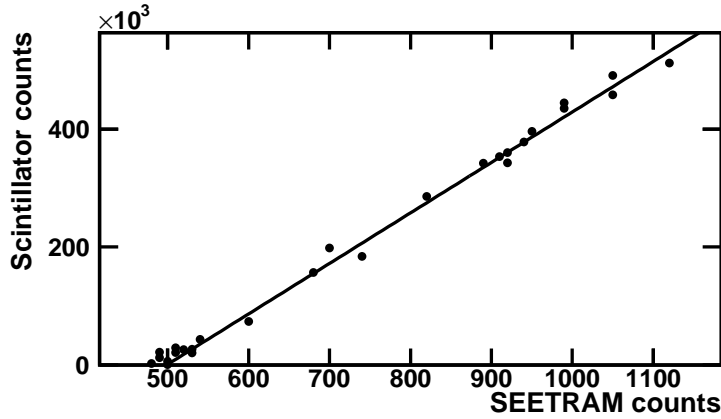


Figure 2.3: Number of counts obtained by the plastic scintillator as a function of the SEETRAM units in the non saturation zone at low beam intensities.

$$N_{beam} = (N_{Seetram} - N_{background}) \cdot f \cdot 10^{10} \cdot Se \quad (2.1)$$

$N_{Seetram}$ is the number of SEETRAM units, $N_{background}$ is the background, f is the SEETRAM calibration factor, Se is the SEETRAM sensitivity that can be changed between $10^{-4} - 10^{-10}$.

2.1.3 Targets

In the case of the direct beams experiment, each target was located at the entry of the spectrometer. In order to investigate the dependence of the charge exchange and knockout reactions with the target mass, several targets were used in the experiment shown in the table 2.1.

Material	Thickness(mg/cm^2)
CH_2 (Polyurethane)	95 ± 2
C	167 ± 3
Cu	373 ± 8
Pb	954 ± 19
Pb	255 ± 5

Table 2.1: Targets and thicknesses used at S0 in the one-step measures.

On the other hand to obtain the secondary beams, we used a beryllium production target located at S0. The thickness of this production target was of $4g/cm^2$. In the section 2.3.2 we explain that in the two stage configuration it is necessary to use reaction targets placed at the middle focal plane. These reaction targets are shown in table 2.2:

Material	Thickness(mg/cm^2)
CH_2 (Polyurethane)	1240 ± 25
C	1472 ± 29

Table 2.2: Targets and thicknesses used at S2. In this case a unstable beam produced at S0 in a Beryllium target of $4g/cm^2$ impinging on these target at S2.

Using the Monte Carlo MOCADI code [97] it is possible to optimize the value of target thickness in order to calculate a good compromise between the reaction production and the resolution in the energy spectrum of the projectile residues.

For more details see the section 3.2. .

2.2 The Fragment Separator FRS

The FRS is a zero-degree magnetic spectrometer with two symmetrical sections: the intermediate plane focal plane is dispersive, being achromatic the complete device. The figure 2.4 shows a schematic representation of the spectrometer. Each part of the spectrometer consists of two dipoles with its respective quadrupoles and sextupoles. The function of the quadrupoles is to guarantee and to support the optical qualities of the focal planes. The sextupoles are used for corrections of high optical order. The FRS can operate in different modes: achromatic and energy loss. In this work we use the FRS in its achromatic mode that consist of assuring the position point to point from the entry to the image exit of the spectrometer. The separator length 72 m with a maximum magnetic field ($B \sim 1.6$) T and using the curvature radius (around $\rho \sim 11.26$ m) assure a maximum magnetic rigidity of $B\rho = 18$ Tm. The FRS angular acceptance is approximately 15 mrad and the momentum acceptance is about 3%

The dispersion is the separation in a position when the momentum fragment changes a 1% with respect to the beam, i.e. the dispersion is the transversal distance between the central-trajectory and the trajectory of a particle with momentum difference $\delta p = 1\%$ behind a bending magnet. The dispersion value is expressed in $cm/\%$. A lower dispersion reduces the magnetic rigity resolution necessary for isotopically identification. For this reason, one can find a compromise between acceptance and dispersion. Other important factor related to the dispersion is the *Magnification*. It is the variation of a coordinate of the particle, from one image plane to the next one. The magnification depends on the dipoles and quadrupoles system in a spectrometer.

The achromaticity is obtained because the dispersion at the final focal plane of FRS $D_{24} = 7.40cm/\%$ compensates the dispersion at middle focal plane of FRS $D_{02} = -7.20cm/\%$ the magnification is $M_{24} = D_{24}/D_{02} = 1.028$. These values were obtained by measuring the trajectory of ^{124}Sn projectiles at 1 A GeV for different values of magnetic fields in the dipoles of the spectrometer (see Fig 2.5).

The intrinsic resolution of the spectrometer depends on two parameters: the dispersion and the acceptance. The *acceptance* is the maximum amount in momentum space transmitted through the spectrometer. The acceptance is determined by geometrical constraints and the characteristics of the magnetic fields of the different elements of the spectrometer.

The maximum momentum acceptance $\left(\frac{\Delta p}{p_c}\right)_{max}$ is related with the dispersion $(x|\delta p)_{02}$ (in Brown notation [98]) through the following equation:

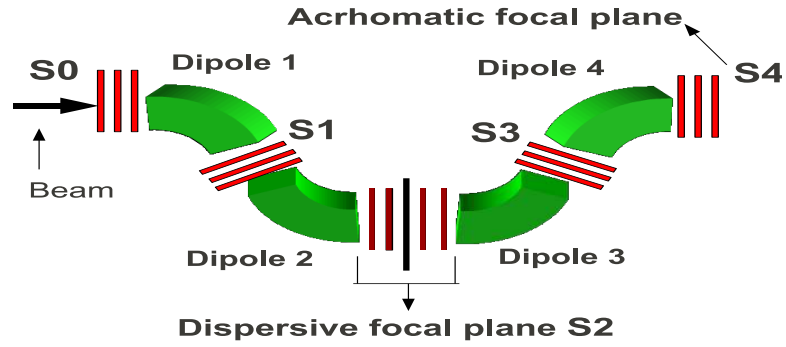


Figure 2.4: FRS Scheme: Dipoles and quadrupoles are shown. The first part is the entry of the spectrometer named S0 followed by different focal planes S1, S2, S3 and S4. The intermediate plane S2 receives the name dispersive focal plane and the plane S4 is the final focal image plane or achromatic focal plane.

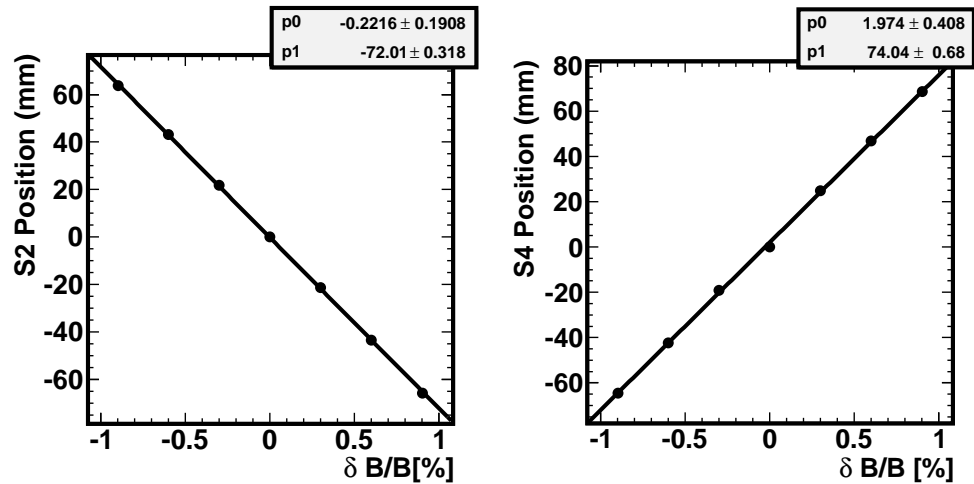


Figure 2.5: Position of the ^{124}Sn beam as a function of the variation of the magnetic field ($\delta B/B$) in the dipole system for the calibration in S2 (left panel) and the final focal plane S4 (right panel).

$$\left(\frac{\Delta p}{p_c}\right)_{max} = \frac{x_2}{(x|\delta p)_{02}} \quad (2.2)$$

This equation shows us that the momentum acceptance is increased by reducing of dispersion.

2.3 The detection equipment

In this section we describe the two configurations of the FRS used for the measurements and the associated detection equipment. Reactions using stable tin projectiles were induced in targets located at the entrance of the FRS. The complete spectrometer was then used to identify the projectile residues and to determine with high accuracy its longitudinal momentum. This is the so called one-stage configuration of the FRS.

To investigate reactions induced by unstable tin isotopes we used the two-stage configuration of the FRS. In this configuration the first part of the spectrometer is used to produced and select the secondary beams and the second part to analyzed the charge-exchange and knockout residues produced by those unstable beams.

2.3.1 One stage configuration: nuclear reactions using stable beams

To investigate stable tin isotopes (^{112}Sn ^{124}Sn) it is possible to use beams with high intensities and different energies. This features made it possible to reduce the thickness of target mass because in our experiment it is very important to reduce the straggling. This experimental optimization will be discuss in the sections 3.2, 2.1.3 . Beams of ^{124}Sn and ^{112}Sn at 1000, 700 and 400 A MeV beams impinged on different targets and the residues produced were analyzed by using the in-flight technique [99]. The figure 2.6 shows the one step configuration. Three plastic scintillators [100] were placed at the S1, the intermediate and the final focal planes. The plastic scintillators provide the information about the time of flight (ToF). In order to track the reaction products to determine the horizontal (x) and vertical (y) position of each fragment, time projections chambers (TPC) were placed at the dispersive focal plane (S2) and the final focal plane (S4) .

The atomic number of fragments was determinated by measuring the energy loss in two Multiple-Sampling Ionization Chambers (MUSICs) [101] placed in the dispersive and the final focal plane, respectively.

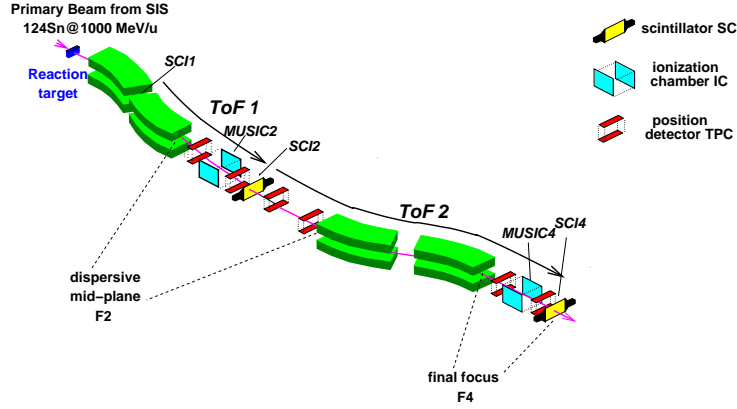


Figure 2.6: *Experimental one step setup: In this configuration it is possible to generate charge exchange reaction in the target at S_0 and identify this reactions products in the S_2 or S_4 focal planes.*

2.3.2 Two stage configuration: nuclear reactions unstable secondary beams

In the experiment it was also possible to investigate reactions using unstable beams. A stable beam impinged on production target located at S_0 and the secondary beam was produced by fragmentation. This secondary beam was identified and separated using the first section of the FRS. We choose the thickness of the reaction target at S_2 as a compromise between the production and straggling effects (see table 2.2) . The intensity of secondary beams is lower than direct beam. For this reason, in order to improve the production we used thicker targets. Figure 2.7 shows the two step setup used to study reaction using secondary beams.

The products of this reaction flying in the forward direction were identified using the second section of the FRS.

2.3.3 The time projection chambers (TPCs)

Time Projection Chambers (TPCs) are ionization gas detectors used with a subdivided anode to measure the horizontal and vertical positions of the particles traversing these devices [102, 103]. The advantage of this detector is the low amount of matter in the active volume that reduce the angular and energy straggling in order to preserve the achromatic mode of the spectrometer. The position resolution obtained with these detectors is about $\sim 200 \mu\text{m}$.

For this experiment 5 TPC's were placed along the FRS: four of them

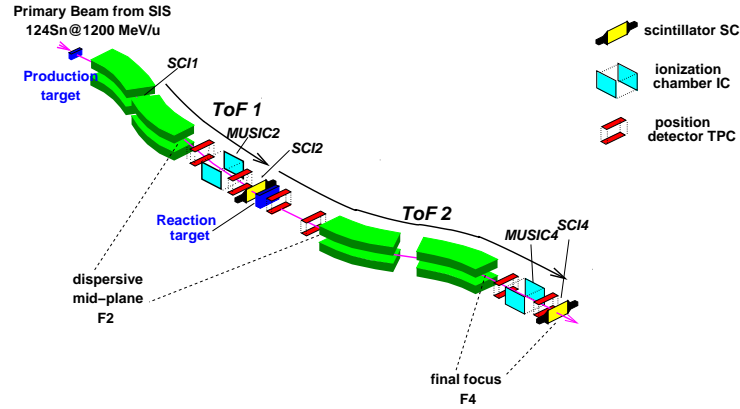


Figure 2.7: *Experimental two step setup: In this experimental configuration is possible study charge exchange reactions using unstable beams. The secondary beam produced at S0 impinging on the reaction target at S2 and in this place the secondary reaction produce the charge exchange reaction products. This reaction products are identified at S4.*

located at the intermediate focal plane and two at final focal plane, as show in figures 2.6 and 2.7. A schematic view of these detectors is shown in Fig. 2.8 and it was filled with P10 gas inside of a uniform electrical field applied in the vertical direction. A charged particle that passes through this detector creates ionization producing electron-ion pairs along the particle track in the gas. The electrons drift toward the anodes by the application of a uniform electrical field.

The drift time provide a measure of the coordinate y and the x axis is obtained by using the delay lines

TPC calibration requests the use of scintillators mask. The mask consist in a grid of scintillators that was placed in front of the TPC. The Direct beam of ^{124}Sn impinged on the scintillator mask and the beam was defocused to covered the mask surface. Finally, the coincidence between the scintillator and TPCs form a pattern. This pattern in figure 2.9 shows the calibration which has been matching the grid in channels with their position values $X = 12\text{mm}$ and $Y = 12\text{mm}$.

2.3.4 Plastic scintillators

To guarantee the high resolution of the FRS it is necessary to fulfill the sufficiently thin detector that preserve the optical quality of the spectrometer, in order not to deteriorate the resolution in the different focal planes.

To reach this requirement an option is to use is necessary to use a set of

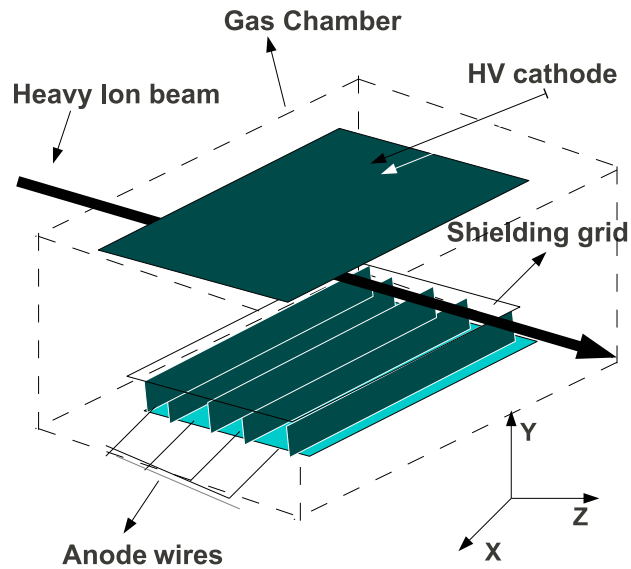


Figure 2.8: Schematic figure of Time projection Chamber TPC. This tracking detector had two delay lines, each one covering a pair of anodes.

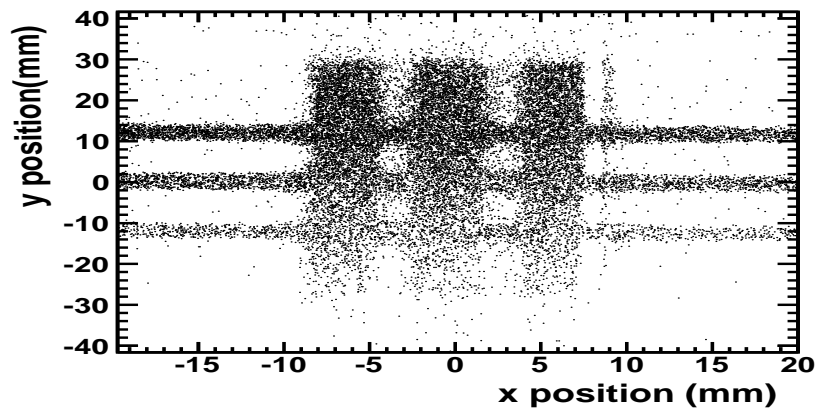


Figure 2.9: This pattern was obtained using the mask scintillators in coincidence with the TPCs for calibrate the position. The lines correspond tho the position and widths of scintillator fingers.

plastic scintillators, that for this experiment made of (BC420). The thickness of the plastics ones located in S1 and S2 (to see figures 2.6 and 2.7) they

was 3 mm and the last plastic in S4 was 5 mm. Every plastic covered the whole focal plane and was connected by two parts of pipe photomultipliers HAMAMATSU R2083, which allow a good time resolution if it did not exceed the limit of high intensities ($\leq 10^5 Hz$).

2.3.5 The Ionization chambers (MUSIC'S)

To identify the charge of some nuclei produced we used two MUlti-Sampling Ionization Chambers MUSIC [101]. These chambers are gaseous detectors and their active volume is of 400 mm along the beam direction. The electrical field inside the chamber is generated across the high voltage applied to the electrodes. Figure 2.3.5 shows a schematic representation of a MUltiple-Sample Ionization Chamber (MUSIC) were placed at S2 and S4.

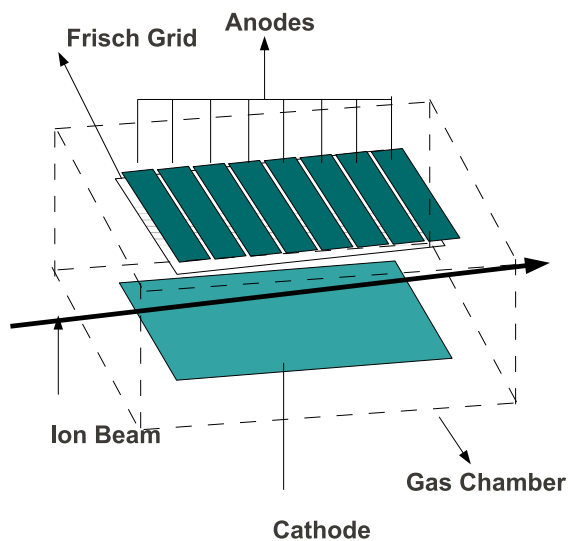


Figure 2.10: Schematic representation of a MUltiple-Sample Ionization Chamber (MUSIC). Identical MUSICs with 8 independent anodes were placed at S2 and S4.

When an ion crosses the active area it loses energy proportional to square of its charge and inversely proportional to its velocity in agreement to Bethe-Bloch's equation. Then produced electrons in the interaction of the ion with the atom gas are collected by the anodes and induce a signal that is amplified

and then digitalized by an ADC (Analog-to-Digital Converter). The digitized signal read out by the system of acquisition.

2.4 Identification of the reaction residues

The FRS and its detection devices allows us an unambiguous identify the reaction products due to its high resolution but also to determine with high accuracy its recoiling momentum. The basic principle that use all magnetic spectrometers is the the action of the Lorentz force from a magnetic field on a moving charge particle.

This relation is written in the following equation:

$$F = q\mathbf{v} \times \mathbf{B} = qvB \quad (2.3)$$

where F is the Lorentz force, q charge and \mathbf{v} is the charge and velocity of particle, B is the magnetic field. From the equation 2.3 it is possible calculate the trajectory of a particle in a circular trajectory of radius ρ :

$$\gamma m_0 \frac{v^2}{\rho} = qvB \quad (2.4)$$

where m_0 is the rest mass of the particle, γ is Lorentz's factor, ρ is the radius of curvature of the particle with charge q inside of the magnetic field B . The previous equation can be rewritten in the following way:

$$B\rho = \frac{Au}{Qe}\gamma\beta c \quad (2.5)$$

In this equation $B\rho$ is named magnetic rigidity , u is the atomic mass unit , e is the elementary charge, c is the speed of the light and $\beta = v/c$. Measuring the magnetic rigidity and the velocity it is possible determine A/Z . In addition the measurement of the atomic charge Q will provide the complete identification in mass (A) and atomic number (Z) of the projectile residues, provided they are fully ionized ($Z. - Q$) and thus it is possible to identify the reaction yield.

2.4.1 Determination of the Magnetic Rigidity

Ion optics formalism [104] provides us a relation to determine the magnetic rigidity of a particle traversing a magnetic spectrometer. In general, the position of a charged particle traversing a dipole magnet along the dispersive coordinate can be described according to the following equation:

$$x_f = (x|x_i)_s x_i + (x|x'_i)_s x'_i + (x|y_i)_s y_i + (x|y'_i)_s y'_i + (x|(\delta B\rho)_i)_s (\delta B\rho)_i \quad (2.6)$$

where the subscript s names the values of the variables of the phase space in the different focal planes of the FRS ¹. The quantities in brackets of the subscript s indicates the coefficients that define the ionic optics of fragment separator for example $(x|x_i)$ is the magnification and $(x|(\delta B\rho)_i)_s$ is the so called dispersion. The other quantities in brackets in the equation 2.6 are variations of the x position with respect to x' , y and y' quantities.

In the focal planes which are also called *image planes*, the correlation between the longitudinal position x and the transversal position y and its angles x' and y' is 0, hereby the equation 2.6 can be written and simplified in the following way:

$$x_f = (x|x_i)_s x_i + (x|y_i)_s y_i + (x|(\delta B\rho)_i)_s (\delta B\rho)_i \quad (2.7)$$

The magnetic rigidity $(B\rho)_s$ can be written in terms of its relative variation with respect to the magnetic rigidity value $(\delta B\rho)_c$ followed by a particle in a central path along the spectrometer. This relative variation $(\delta B\rho)$ is expressed in the following equation:

$$(\delta B\rho)_s = \frac{(B\rho)_s - (B\rho)_c}{(B\rho)_c} \quad (2.8)$$

In the case of the FRS, it has a symmetry in respect to the focal plane, so horizontal and transverse components are independent, thus the term of the equation 2.8 $(x|y_i)_s = 0$. So, we can obtain a relation between the magnetic rigidity, the position of the focal plane and the optics of the magnetic system. For example in the case of the intermediate plane or S2 the magnetic rigidity can be written as:

$$(\delta B\rho)_2 = (B\rho)_c \left(1 - \frac{x_2}{D_{02}} \right) \quad (2.9)$$

Here x_2 is the position in the intermediate focal plane and D_{02} is the value of the dispersion from the S0 up to this focal plane in S2. For the focal final plane it is possible to find the following relation for the magnetic rigidity:

$$(\delta B\rho)_4 = (B\rho)_c \left(1 - \frac{x_4 - M_{24}x_2}{D_{24}} \right) \quad (2.10)$$

¹ $s = 0$ indicates the entry of the FRS, $s = 2$ indicates the intermediate focal plane or dispersive plane and $s = 4$ indicates the final focal plane

where x_2 and x_4 are the positions in the focal planes S2 and S4 respectively, D_{24} is the dispersion between both planes: the intermediate and the final focal plane with M_{24} is the magnification. We can determine any nucleus rigidity if we know all parameters of the ionic optics given in the equation 2.10 principally the magnification and the dispersion as well as the magnetic rigidity of a particle with central path across the FRS.

The value of the central magnetic rigidity $(B\rho)_c$ was measured by a beam reference through out of FRS, besides with this value and the direct measure of the magnetic field obtained with the Hall probes that have a relative resolution around $\sim 10^{-4}$ in magnetic rigidity. The resolution achieved for the atomic mass is $\Delta A/A = 4.08 \times 10^{-3}$ (FWHM).

2.4.2 Determination of the reduced momentum

In the equation 2.5, the term $\gamma\beta$ is called the *reduced momentum* and it is obtained from the measurement of the time-of-flight (ToF) of the nucleus traversing the FRS. For this experiment the ToF was determined from the time measurement provided by the plastic scintillators located at the image planes of the FRS as it appears in the figures 2.6 and 2.7.

Each plastic scintillator provide two signals of time: a signal for the left side (L) and other one for the right side (R). These signals are filtered and sent to Time to Amplitude Conversor (TAC). The ToF quantity was measured a from the average of the left and right signals as shown the following equation:

$$ToF^* = \frac{\alpha_L ToF_L + \alpha_R ToF_R}{2} \quad (2.11)$$

Here α_L and α_R are the TAC calibration factors obtained from a pulse generator of adjustable frequency. The START signal for the time measurement is given by the scintillators at S4 whereas the STOP signal is given by the scintillator at S2 delayed a quantity T_0 , this fact is to assure the arrival of the START signal before the STOP one. Then the real value of ToF is obtained in the following way:

$$ToF^{Si} = ToF_{STOP}^{Si} - ToF_{START}^{Si} = T_0 - ToF^* \quad (2.12)$$

where superscript Si indicates the ToF measurement in each focal plane e.g. for $i = 2$ note the ToF measure at S2. The delay parameter T_0 was obtained from measurements with the primary beam at different velocities.

This calibration was performed using targets with different thickness in order to change the beam velocity in each setting, therefore to change the time-of-flight. The corresponding velocities of the beam were then calculated

calculated using the AMADEUS code [105]. The relationship between the inverse velocity and ToF^* is given in the following expression:

$$\frac{1}{v} = \frac{T_0}{l_{Si}} - \frac{ToF^*}{l_{Si}} \quad (2.13)$$

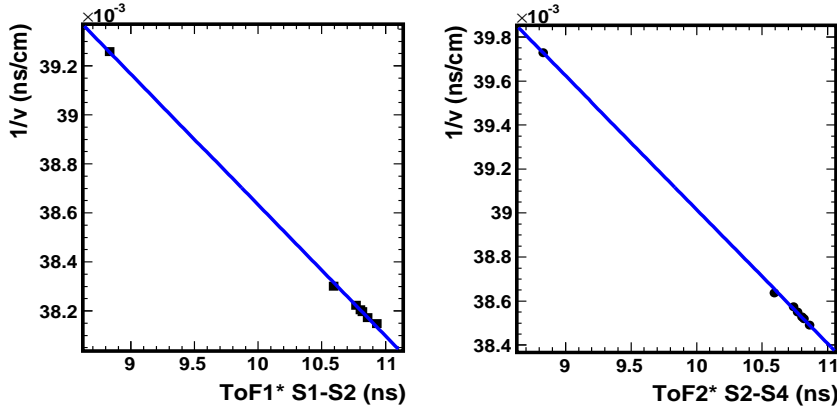


Figure 2.11: Inverse of velocity as a function of Time of Flight (ToF^*) used for calibration. The left panel corresponds to S1-S2 ToF and the right panel to the S2-S4.

Where l_{Si} is the beam path between two measured time points (i.e S1-S2 or S2-S4). T_0 and l_{Si} were determined using a linear fit like appeared in the figure 2.11 whose coefficients provided the values $T_0 = 89.33ns$ and $l_{S2} = 37.92m$. The typical ToF resolution achieved in the experimental set up was around 170 ps FWHM .

2.4.3 Determination of Atomic number Z

In the section 2.3.5 we explained that the energy loss of the reaction product inside of the MUSIC is proportional to square of its atomic number (Z^2). We can determine the atomic number of the reaction product using the average of the energy loss in each anode by the following way:

$$Z = \alpha + \beta \sqrt{\sum_{j=1}^N \frac{\Delta E_j}{N}} \quad (2.14)$$

here N is the number of anodes (in our case N=8), ΔE_j is the amplitude of the signal from each anode. The calibration parameters α and β were

obtained using a ^{124}Sn beam at 1 A GeV (see Fig. 2.12). The resolution achieved for the atomic mass is $\Delta Z/Z = 3.35 \times 10^{-3}$ (FWHM).

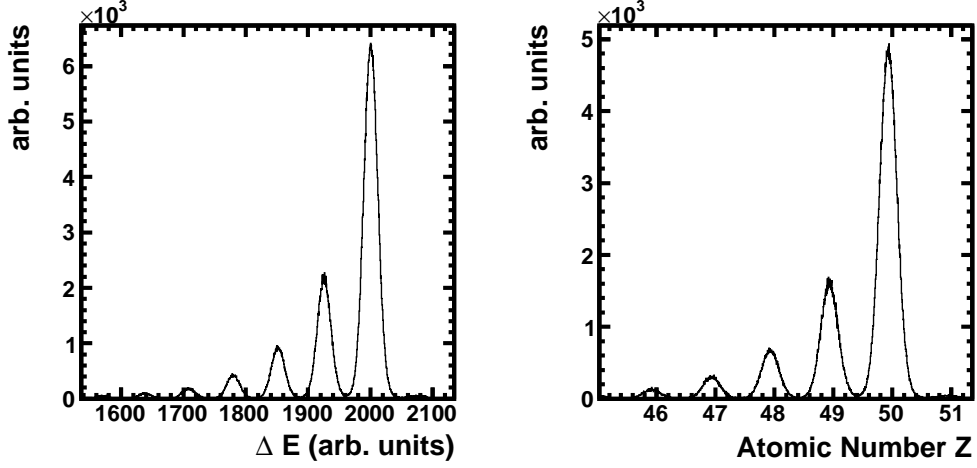


Figure 2.12: Charge identification of the peaks signals from the MUSICs. Left panel: Average energy loss in the MUSICs detectors for a setting centered on ^{124}Sn . Right panel represent the spectrum of MUSIC for a magnetic setting centered in ^{124}Sn .

Figure 2.12 shows the energy-loss peaks for a magnetic setting centered in ^{124}Sn . The average energy loss ΔE and its correspond Z values are shown.

2.4.4 Mass-over-charge ratio determination Determination of mass resolution

Many factors can affect the correct identification of each isotope and it is important to correct this effects in order to improve the identification. One of this effects is the mass-over-charge dependence on the horizontal angle θ due to the path length of the residues which is not the same because each isotope does not have the trajectory inside of FRS. Using the calculation of the angle defined in the equation 3.10 we can correct the mass over charge ratio dependence on angle. (see the figure 2.13).

Using the equation 2.5 it is possible to determine the mass-over-charge ratio (A/Z) of each transmitted nuclei by combining two independent measurements: the magnetic rigidity ($B\rho$), determined from the position measurements of the TPC detectors, and the velocity, obtained from the measured time-of-flight (ToF).

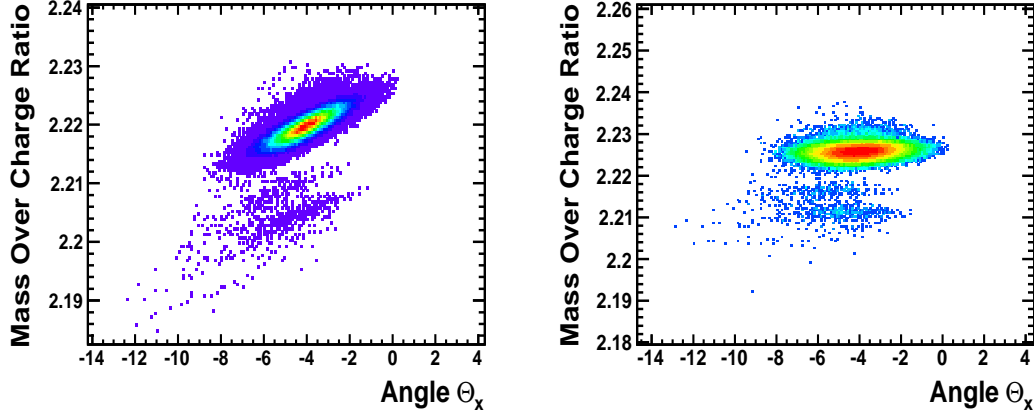


Figure 2.13: Mass-over-charge (AoQ) correction with respect to angle θ . The left represent the AoQ ratio as a function of the angle θ_x of the trajectories at the final focal plane for some isotopes transmitted in a setting centered on ^{112}Sn .

Figure 2.14 shows the resolution achieved for the mass-over-charge ratio for the Indium isotopes 3.06×10^{-3} (FWHM). With this resolution in A/Z and atomic number (Z) achieved in these measurements are very good, allowing us to unambiguously separate all fragments produced and transmitted along the magnetic spectrometer as appear in the identification matrix (see for example 2.15).

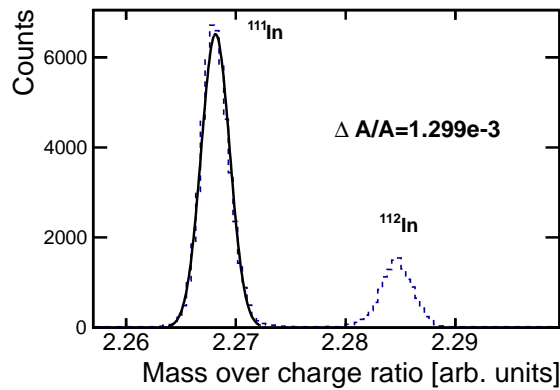


Figure 2.14: Distribution of mass-over-charge ratio of the Indium fragments in a setting centered in ^{112}In setting centered in ^{112}In .

The calculated A/Q , together with the atomic number (Z) obtained from the energy loss detectors (MUSIC chambers), can be used to produce an identification cluster plot like the one shown in Figure 2.15, where each nucleus is represented by a spot.

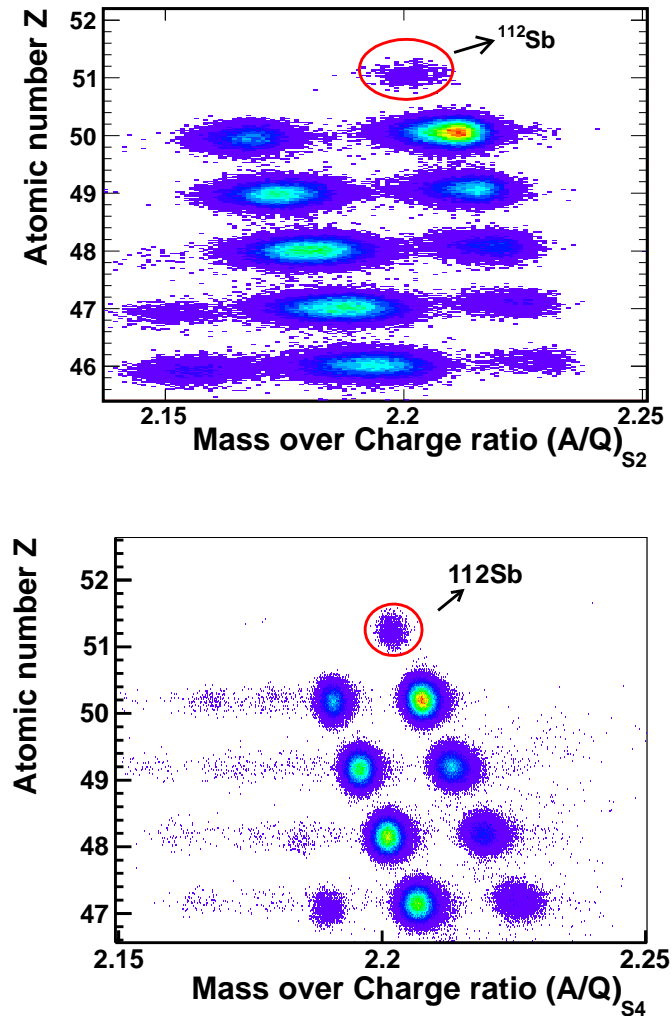


Figure 2.15: Identification plots (atomic number Z as a function of mass-over-charge ratio): the upper figure is a identification plot at dispersive focal plane (S_2) of the reaction products in the reaction at 1 A GeV of $^{112}\text{Sn}(C, X)^{112}\text{Sb}$. The following plot is the identification plot at the final focal plane S_4 of the reaction product in the reaction at 1 A GeV of $^{112}\text{Sn}(C, X)^{112}\text{Sb}$.

CHAPTER 3

Physical Observables

The aim of this chapter is to describe the procedure followed to determine the of physical observables: the longitudinal momentum, angular distributions and the cross section of the projectile residual nuclei produced in these reaction channels.

The determination of the longitudinal momentum and angular distributions require a high accuracy measure of the position of the fragment trajectories inside the FRS using the TPC detectors and the magnetic Hall probes. Many factors affect the resolution of the longitudinal momentum and angular distributions as discussed in section 3.2. Sections 3.3 and 3.4 describe the procedure followed to obtain the energy and angular distributions . Section 3.5 will be dedicated to the evaluation of the residual projectiles cross-sections in the one and two configurations of the experiment. The cross section allows us investigate the neutron and proton content in the projectile, and by using the energy distribution it will be possible to analyze the interaction probability of charge exchange reactions or knock out reactions.

3.1 Isotopic identification

In the previous chapter we explained in detail the isotopic identification process of the residues produced in the reactions investigated in this work. As it was explained our experimental approach is based in the complete identification of the projectile reaction residues. This isotopic identification is the base to obtain the physical observables: cross sections of the projectiles

residues and their energy recoil distributions.

According to equation 2.5, the mass-over-charge ratio (A/Q) of a particle traversing the FRS can be determined from their magnetic rigidity and the velocity. The magnetic rigidity can be determined from the positions of the fragments at the intermediate and final focal planes, respectively. The velocity in both stages was obtained from the time of flight ToF measurements.

Using the A/Q and the atomic number (Z) values obtained from the MUSE chambers, it is possible to produce an identification plot (atomic number Z as a function of mass-over-charge ratio) like the one shown in Figure 2.15. The resolution in A/Q and atomic number achieved in these measurements are excellent and allow us to unambiguously separate all fragments produced and transmitted along the FRS. Nevertheless, the identification in the final focal plane of the spectrometer (S4) is better than the one obtained at dispersive focal plane because the velocity resolution is increased by the increment of the flight path length of each particles.

Using the two sections of the FRS spectrometer it is possible to identify the particles in the intermediate and final focal planes. The two stages configuration of this spectrometer allow us to carry out reaction using stable or unstable beams, in the first case the reaction was produced in entrance of the FRS (at S0) (see section 2.3.1) and in the second case the reaction using a secondary beam was investigated locating the target at the the intermediate focal plane (at S2) (section 2.3.2).

3.2 Longitudinal-momentum of the recoiling projectile -like residues

The momentum (energy) recoil distributions is an essential physical observable that characterize the reaction process. The accurate determination of the longitudinal momentum of the nuclei traversing a zero-degree magnetic spectrometer such as the FRS depends on the measurement of the corresponding magnetic rigidities.

If one considers incident particles with the same magnetic rigidity, the same expression (2.2) will provide us the accuracy in the magnetic rigidity determination according to the dispersion of the magnetic spectrometer and the accuracy in the measurement of the positions of the trajectories at the intermediate and final image planes.

The accuracy in the measurement of the positions can be affected by the resolution of the tracking detectors, the initial emittance of the beam, the energy, angular, and reaction location straggling of the transmitted particles

in the different layers of matter traversed by the reaction residues.

Figure 3.1 represents the estimated contributions to the final resolution in the measurement of the magnetic rigidity due to the resolution of the tracking detectors, the beam emittance, and the electromagnetic interactions of the nuclei with an aluminum target as a function of its thickness. In these calculations, we have taken as reference the nominal values of the dispersion and magnification of the Fragment Separator ($(x|\delta p)_{24} = 7.40 \text{ cm}/\%$ and $(x|x)_{24} = -7.20 \text{ cm}/\%$

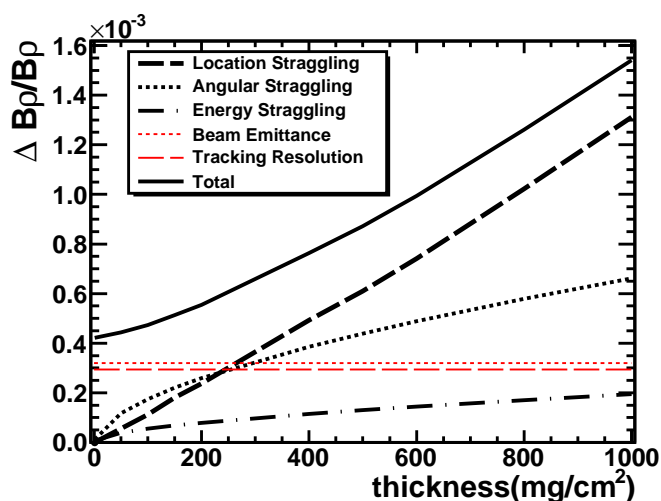


Figure 3.1: Different contributions to the resolution in magnetic rigidity measurements with a magnetic spectrometer as a function of the target thickness. The thin horizontal lines represent the energy spread of the beam (dotted line) and the effect due the position resolution of the tracking detector (dashed line). The thick lines represent the effect due to the electromagnetic interactions of the projectile and residual nuclei with the target: energy straggling (dashed-dotted) line, angular straggling (dotted line), the reaction location straggling (dashed line). The thick solid line represents the final resolution considering all the contributions.

In the figure 3.1, the thin horizontal lines represent the contribution to the resolution due to the beam energy dispersion $\Delta E/E = \pm 5 \times 10^{-4}$ (dotted line) and the tracking detector resolution considering $\Delta x_2 = \Delta x_4 = 0.2 \text{ mm}$ (dashed line). The thick lines evolving with the target thickness represent the contribution to the magnetic rigidity resolution due to the electromagnetic interactions of the incoming nuclei with the target material, the energy straggling (dashed-dotted line), the angular straggling (dotted line) and the reaction location straggling (dashed line). The solid line represents the final resolution considering all the above mentioned effects.

As can be seen in the figure, the position resolution of the tracking detectors and the beam emittance limit the magnetic rigidity resolution for aluminum targets thinner than 250 mg/cm². For thicker targets, the resolution is limited by the electromagnetic interactions of the transmitted nuclei with the target material.

Unfortunately, the target thickness is very often determined by statistical considerations. In the particular case of measurements with secondary beams of nuclei far from stability having low intensities the feasibility of the measurements requires the use of thick targets. In those cases, the possibility of unfolding contribution of those effects degrading the magnetic rigidity resolution could be an option for accurate measurements. Moreover, the measurement of the momentum dispersion of non-interacting beam nuclei provide an optimal definition of the experimental response function required by the unfolding procedure. Indeed, beam nuclei experience electromagnetic interactions in the target and the layers of matters that are placed along the spectrometer.

In our case, we choose the targets (see 2.1.3) in order to minimize the straggling effects and in this way improve the energy distributions.

In the case of reactions at S0 we could to select thinner targets than S2 reactions because the high intensity of a direct beams assured a high production of nuclear residues. On other hand, in the case of the S2 reactions the secondary beam has a relative low intensity, for this reason we increase the thickness of the reaction target in order to increase the production reaction products. This procedure implies that the resolution of the momentum distribution decreases as consequence of the straggling effects.

Longitudinal and Parallel Momentum distributions

The longitudinal momentum of a reaction residue is one of the physical observables and that preserves the physical information about the interaction at microscopical level. This observable can be obtained from the equation 2.4 rewritten the expression in the following way:

$$p_{\parallel} = \gamma m_0 v = qB\rho \quad (3.1)$$

The relation between the parallel (p_{\parallel}) and the transversal (p_{\perp}) momentum can be obtained from the following equation:

$$\tan\theta = \frac{p_{\perp}}{p_{\parallel}} \quad (3.2)$$

where θ is the polar angle of the projectile residues that can he obtained with the TPC tracking.

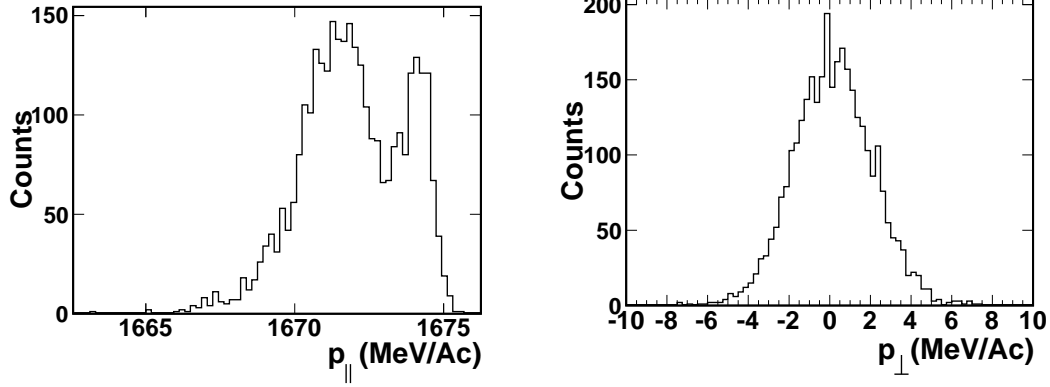


Figure 3.2: Momentum Distributions in the Laboratory frame in the reaction of $^{112}\text{Sn}(C, X)^{112}\text{Sb}$ at 1 A GeV. Left panel: longitudinal momentum p_{\parallel} . On the right panel: longitudinal momentum p_{\perp} .

In the figure 3.2 we compare the two components of the momentum in the reaction of $^{112}\text{Sn}(C, X)^{112}\text{Sb}$ at 1 A GeV. We can observe that the p_{\parallel} is much larger than p_{\perp} and for this reason, in our case, the transversal component is considered negligible.

3.3 Recoiling energy of projectile residues

From the magnetic rigidity or longitudinal momentum it is possible to determine the recoiling energy of the projectile reaction residues. The relativistic kinetic energy at the intermediate image plane S2 can be obtained from the magnetic magnetic rigidity according to the following equation:

$$E_{S2} = A \cdot u \left[\sqrt{1 + \left(\frac{B\rho_{S2} \cdot Z \cdot c}{A \cdot u} \right)^2} - 1 \right] \quad (3.3)$$

Here $u = (931.45 \text{ MeV}/c^2)$ is the nucleon mass unit, A is the mass number of the nucleus, $B\rho$ and Z are its magnetic rigidity and atomic number charge respectively. The transformation of this observable into the frame of the moving projectile will provide the energy lost induced by the nuclear reaction.

3.3.1 Energy transformation of the beam frame

In order to determine the energy of the projectile residues in the frame defined by the mean velocity of the incoming projectile nuclei in the middle of the target, it is necessary to correct the slowing down of the nuclei through the layers of matter they traverse the S2 or S4 focal planes.

Figure 3.3 illustrates the energy lost by the incoming projectiles in the different layers of matter located along of the beam-line until the middle of the target (E_0). The list of layers of matter placed along the FRS is presented in the appendix A.

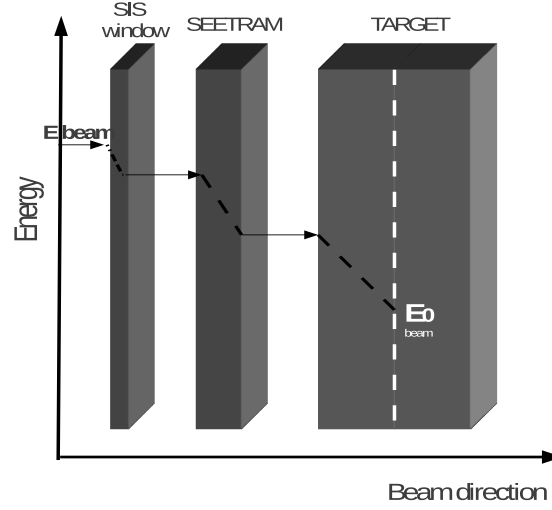


Figure 3.3: Schematic diagram that represents the considerations done by us in order to determine the average velocity of the beam in the middle of the target. This approximation is important because this is the reference velocity used to calculate the Lorentz boost.

In order to obtain the energy or momentum distribution in the beam velocity frame, it is necessary to make a Lorentz transformation. The following equation give us the transformation between the references frames:

$$\begin{pmatrix} E_{bf} \\ p_{\parallel bf} \end{pmatrix} = \begin{pmatrix} \gamma_{vb} & -\gamma_{vb}\beta_{vb} \\ -\gamma_{vb}\beta_{vb} & \gamma_{vb} \end{pmatrix} \begin{pmatrix} E_{lab} \\ p_{\parallel lab} \end{pmatrix} \quad (3.4)$$

where $\gamma_{vb} = 1/\sqrt{1 - \beta_{vb}^2}$, $\beta_{vb} = V_{vb}/c$; V_{vb} represent the beam velocity in the middle of the target, E_{lab} and $p_{\parallel lab}$ are the total energy and longitudinal

momentum of the fragment in the laboratory frame respectively. From the equation 3.4 it is possible to obtain the longitudinal momentum $p_{\parallel bf}$ in the beam reference frame using the following expression:

$$p_{\parallel bf} = \gamma_{vb} \left(p_{\parallel lab} - \beta_{vb} \frac{E_{lab}}{c} \right) \quad (3.5)$$

$$p_{\perp lab} = p_{\perp bf}$$

The transversal momentum p_{\perp} is the same in both reference frames.

Also it is possible to obtain the energy in the beam particle frame (E_{bf}):

$$E_{bf} = \gamma_{bf} (E_{lab} - \beta_{bf} p_{\parallel lab}) \quad (3.6)$$

Figure 3.4 shows the energy distribution of ^{124}Sb projectile residues produced in the reaction $^{124}\text{Sn}(C, X)^{124}\text{Sb}$ in the beam-moving frame. In this reference frame the particles close to zero value are those with a kinetic energy similar to the beam and corresponds then to elastic reaction channels. Particles with negative energy indicate the kinetic energy loss induced in inelastic reaction channels. The two peaks observed in the figure correspond to elastic and inelastic isobar charge-exchange reactions that will be explained in the next chapter.

3.3.2 Energy resolution

The final energy resolution that could be achieved depends on several factors such as the resolving power of the spectrometer, the optical quality of the primary beam, the amount of matter along the FRS and the resolution of the position detectors. All these factors produce an extra broadening in the energy distributions that is not related to the reaction mechanism. The intrinsic energy resolution was evaluated by using the following equation:

$$\frac{\Delta E}{E} = \left(1 + \frac{Mc^2}{Mc^2 + E} \right) \frac{\Delta(B\rho)}{B\rho} \quad (3.7)$$

The equation 3.7 takes into account the contribution of the resolution of the spectrometer. The additional effects will contribute quadratically to the final resolution according to the following equation:

$$\left(\frac{\Delta E}{E} \right)_{exp} = \sqrt{\left(\frac{\Delta E}{E} \right)^2 + \left(\frac{\Delta E}{E} \right)_{str}^2} \quad (3.8)$$

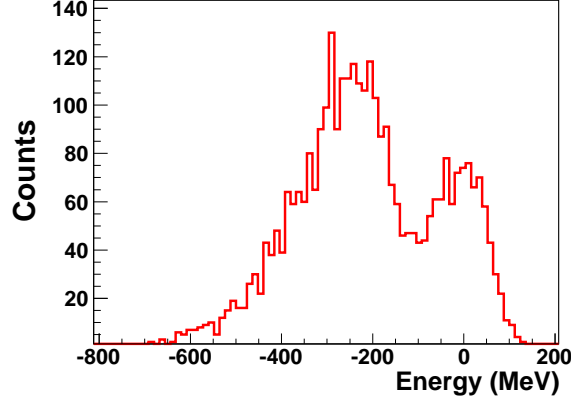


Figure 3.4: Energy distribution for ^{124}Sb in the beam particle frame obtained by the np reaction channel of the ^{124}Sn on carbon target at 1 A GeV

The term $\left(\frac{\Delta E}{E}\right)_{str}$ is the straggling effect and beam emittance that affect the energy measure, this value is calculated using AMADEUS code [105]. These effects were already discussed in the section 3.2.

Table 3.1 summarize the energy resolution achieved for each target in the one step configuration. However, the resolutions achieved in the two step configuration are presented in the table 3.2 with higher values than one step configuration.

Target	Thickness (mg/cm^2)	$\Delta E/E(\text{MeV})$
Carbon	197	10.0
Cooper	373	10.3
Lead	255	10.0

Table 3.1: Energy Resolution in the beam particle frame using the one step configuration

Target	Thickness (mg/cm^2)	$\Delta E/E(\text{MeV})$
Carbon	1400	28.5
Carbon	910	19.0

Table 3.2: Energy Resolution in the beam particle frame using the two step configuration

The energy value of the resolution obtained with the 3.7 and considering the beam-line matter appears in the tables 3.1 and 3.2.

3.3.3 Unfolding of the experimental response

Using unfolding techniques one can try to separate the physical information of the experimental distribution with respect to the effects induced by the limited resolution of the experimental setup. In this work, we used the Richardson-Lucy deconvolution method. An extended description of the method is presented in the appendix B [106] .

In this method we assume that the measured energy distribution of the primary beam ions represents the response function of our experimental setup. Indeed, for the implementation of the deconvolution the energy distribution of the beam ions will represent the effect of the energy and location straggling, induced by the detection system and the beam emittance. In Fig 3.5 we show the response function and the experimental distribution obtained for the reaction $^{124}\text{Sn}(C, X)^{124}\text{Sb}$ at 1 A GeV that we use as inputs for the deconvolution method.

The Richardson-Lucy deconvolution is an iterative technique and as with other deconvolution techniques, the output of this method is iteration-dependent. This issue must be addressed carefully, particularly in those cases where the width of the distribution of a given observable is of interest, as in the case energy distributions that we will discuss in the chapter 4. Figure 3.6 represents the unfolding dependence with the number of iterations (N). This test, performed with this method, revealed that the width of peaks in the true distribution become narrower in successive iterations.

In order to minimize the uncertainties associated with the oscillations or degradation of the solution in an iterative deconvolution, a method of regularization is necessary to define the optimal number of iterations [107]. To optimize the computing time, a relatively simple regularization method based on the χ^2 is proposed in this work. This χ^2 is applied to the difference between unfolded and the original spectrum for each N iteration. Regularization methods and stopping criteria based on the standard χ^2 are well-known in other applications such as image reconstruction techniques [108, 109]. In some of these methods, the feasibility of the solution is measured with the χ^2 , and the process is stopped when this reaches a certain limit, preventing the solution to degrade. In the present case, we look for a minimum of the χ^2 in order to halt the deconvolution process.

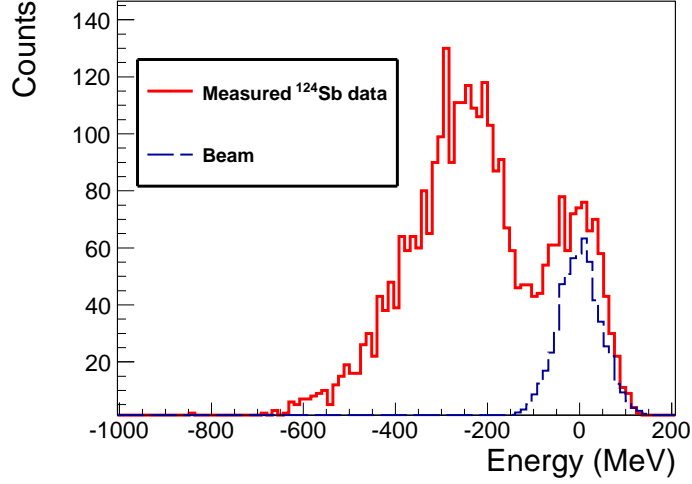


Figure 3.5: Comparison between the beam energy distribution (^{124}Sn dashed line) and the ^{124}Sb (solid line) produced in the reaction $^{124}\text{Sn}(C, X)^{124}\text{Sb}$ at 1 A GeV in the beam particle frame. The beam energy distribution represents the response function. The response function contains the contributions of the target thickness, energy-loss straggling, the beam emittance and the intrinsic resolution of FRS.

Correlations of calculated parameters

In general, the χ^2 value should be an indicator of the goodness of the result. In order to test this, we represent in Fig. 3.7 the correlation between the value of the χ^2 from the deconvolution method and the deviation of the result of each parameter in the case of Breit- Wigner peaks (mean values and widths) respect to their corresponding true values. The panels show that the resulting values concentrate in the vicinity of the true distribution and χ^2 around 1. A collection of measured distributions Y is produced by varying the statistics and the binning of the histogram. Statistical fluctuations are taken into account changing the statistical counts by events. On the other hand, variations on the histogram binning change the number of points available to calculate the true distribution. The Richardson-Lucy deconvolution and the χ^2 - based regularization method are applied to this collection of distributions. Interestingly, there seems to be no particular correlation between the value of χ^2 and the accuracy of the results at this stage.

Based on the results shown in Fig.3.7 , a mean and width value of each parameter would be a good approximation to the results of the deconvolution process. However, a further stage can be applied in order to improve the quality of the results: it is not unusual for deconvolution methods to yield

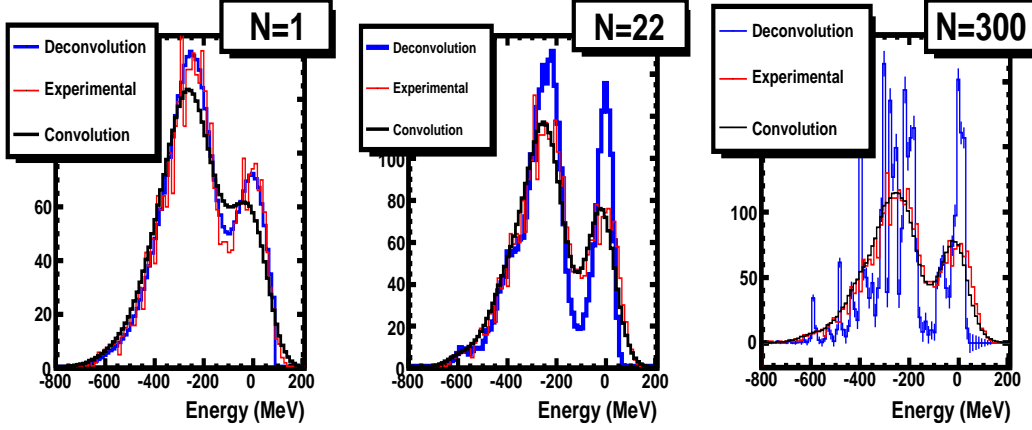


Figure 3.6: Unfolding dependence with the number of iterations (N): we can see the evolution of the deconvolution spectrum when the iteration number is increased. The convolution (black line) and its comparison with the experimental data give us the χ^2 value used in the regularization method. The χ^2 value corresponding to $N=1$ is 1.78, for $N=22$ we found a minimal value of $\chi^2 = 1.02$ and after this χ^2 is increased, for example for $N=300$ this $\chi^2 = 1.27$.

mathematical artifacts within the set of solutions. In order to separate these anomalies, we perform a robust average of the parameters describing the peaks found in the distribution. This procedure, based on the algorithm proposed by Rousseeuw and Van Driessen [110], searches within the set of solutions the subset that minimizes the sum of the standard deviations of the parameters. The minimum size of the subset is fixed at number of points + number of parameters + 1/2. In this case we consider the systematic error in the unfolding method is about $\frac{\Delta T}{T}_{Unf} \sim 8\%$ in the mean value estimation and 18% for width value estimation using the method described in the reference [106].

Then the final result will be given by the following equation:

$$\left(\frac{\Delta T}{T}\right)_f = \sqrt{\left(\frac{\Delta T}{T}\right)_{Unf}^2 + \left(\frac{\Delta T}{T}\right)_{fit}^2} \quad (3.9)$$

This error value depends on the goodness of $\frac{\Delta T}{T}_{fit}$ because in the case of the mean value determination. Then this error must be analyzed thoroughly in each case.

In addition to the deconvolution process, it is necessary to subtract the contribution of the reaction in the beam-layer materials. In fact these reactions increase the number of counts and modify the energy distributions. In

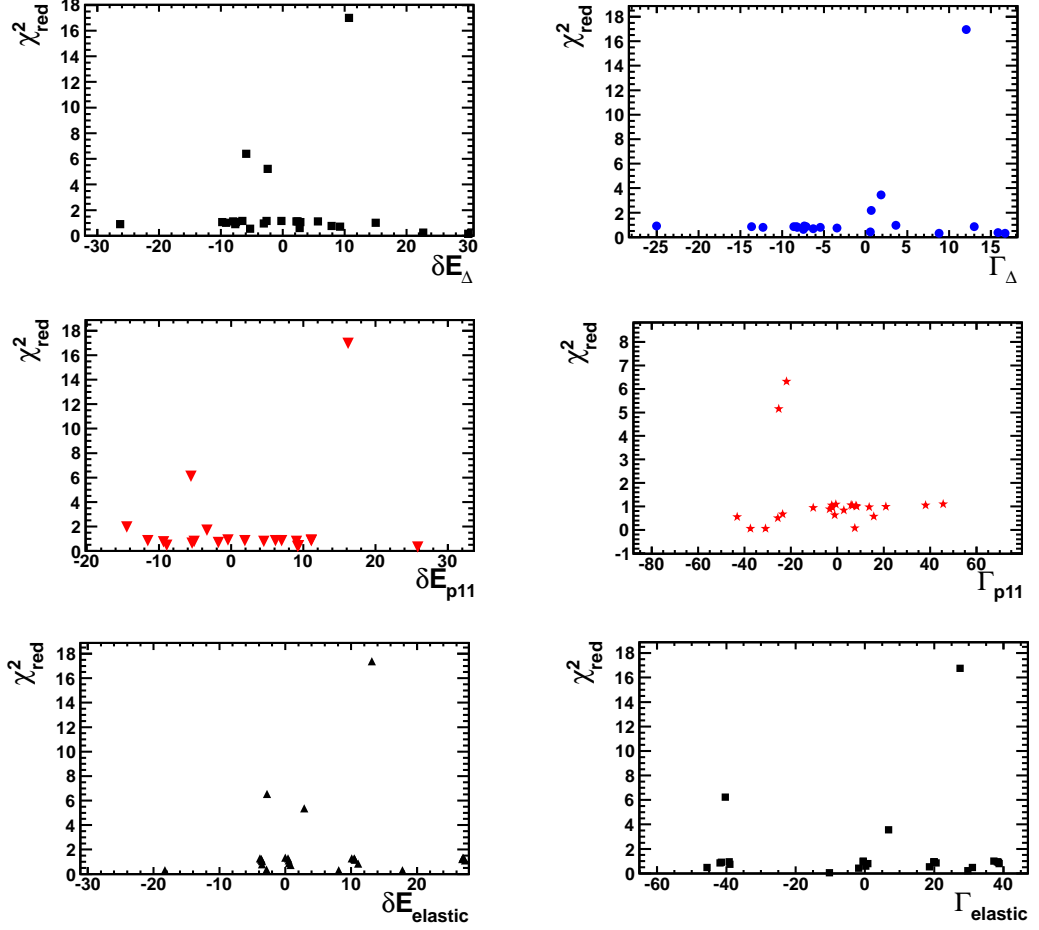


Figure 3.7: Correlation between the value of the χ_{red}^2 resulting from the deconvolution and regularization methods and the deviations in the mean (δE_i) and width values (Γ_i). At top part correspond to the mean and width values of the Δ resonance, the following plots correspond to the Roper resonant δE_{P11} and Γ_{P11} mean and width values respectively and $\delta E_{elastic}$ and $\Gamma_{elastic}$. Each point corresponds to the correlation for a particular binning and number of counts in the histogram.

the section 3.5.1 this effect was already corrected in the case of the section measure.

Figure 3.8 represents the energy distribution (solid line) and its deconvolution (dashed line). The final energy distribution obtained by the unfolding method represents the physical information without response function contributions.

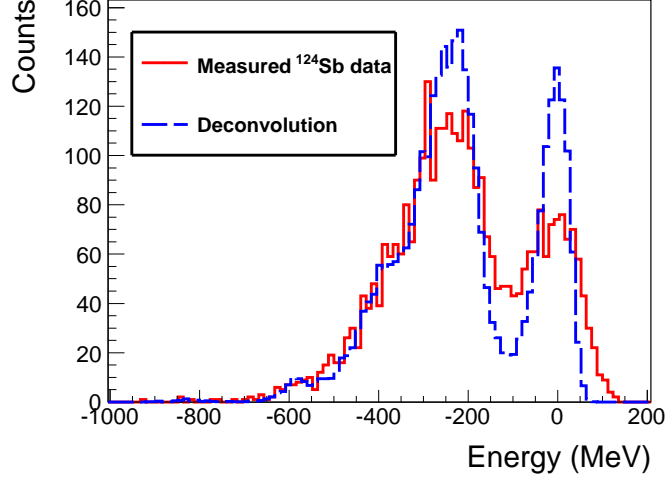


Figure 3.8: Figure represents the energy distribution (solid line) and its deconvolution (dashed line). The final energy distribution obtained by the unfolding method represents the physical information without response function contributions.

3.4 Angular distributions of charge-exchange reaction residues

Using the positions measured with the TPC's it is possible to obtain the polar angle of the reaction residues between these tracking detectors. The following relation shows the way to calculate the forward angle in the laboratory frame θ_{lab}

$$\theta_{lab} = \tan \left(\frac{X_{3pos} - X_{2pos}}{Dist_{32}} \right) \quad (3.10)$$

where X_{3pos} and X_{2pos} are the position in each respective TPC, $Dist_{32}$ is the distance between the TPC's. To obtain the angle in the center mass frame (CM) we need to express it in the following way:

$$\theta_{CM} = \text{atan} \left(\frac{\sin(\theta_{Lab})}{\gamma(\cos(\theta_{Lab}) - \frac{V_{beam}}{V_p})} \right) \quad (3.11)$$

where V_{beam} and V_p are the velocities of beam and particle respectively and $\gamma = \sqrt{\frac{1}{1-\beta^2}}$. The figure 3.9 shows the angular distribution in the reaction $^{112}\text{Sn}(C, X)^{112}\text{Sb}$ at 1 A GeV.

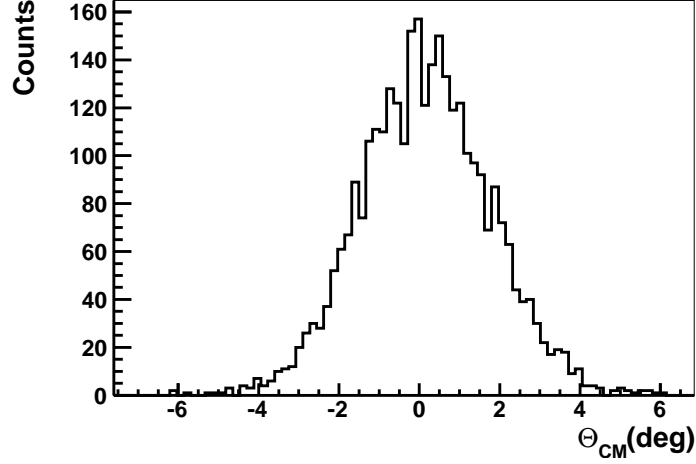


Figure 3.9: Angular Distributions of $^{112}\text{Sn}(C, X)^{112}\text{Sb}$ at 1 A GeV in the CM frame.

Figure 3.10: Angular Distributions of $^{112}\text{Sn}(C, X)^{112}\text{Sb}$ at 1 A GeV and 700 A MeV in the CM frame.

The resolution in the position measure affect the calculation of the forward angle. First we consider the angular resolution obtained by the propagation of the uncertainty of the position measurement give in the next equation:

$$\frac{\Delta\theta}{\theta} \sim \frac{\Delta x}{Dist_{ij}} - \frac{X_{jpos} - X_{ipos}}{\Delta Dist_{ji}^2} \quad (3.12)$$

where Δx and $\Delta Dist_{ji}$ are the position uncertainties of the TPC measure and the distance between de TPC's respectively. But the total angular measure is affected by the angular straggling. Due to the electromagnetic interaction of the nuclei with the material layers the direction of the fragment changes.

This effect changes the original angle and alters the angular distribution as well. Then the final angular resolution $\frac{\Delta\theta}{\theta}_{lab}$ is given by the position resolution calculation $\frac{\Delta\theta}{\theta}$ and the angular straggling contribution $\frac{\Delta\theta}{\theta}_{st}$ by the following way:

$$\left(\frac{\Delta\theta}{\theta}\right)_{lab} = \sqrt{\left(\frac{\Delta\theta}{\theta}\right)^2 + \left(\frac{\Delta\theta}{\theta}\right)_{st}^2} \quad (3.13)$$

Using the equations in 3.13 it is possible to obtain the resolution in the CM frame, this value is about $\sim 0.7^\circ$

3.5 Production cross sections of projectile residues

This chapter deals with experimental technique and the calculation of the cross section. The reactions produced at $S0$ in the one-step configuration (see 2.3.1) are corrected with the factors that will be described in the next section. A particular case of the cross sections measures using the two step configuration will be studied in the section 3.6.

The cross section is determined by the production yield of every nucleus normalized to the number of projectile and the number of atoms per cm in the target.

$$\sigma = \frac{y \cdot C_f}{N_t N_b} \quad (3.14)$$

In this equation N_b is the number of projectiles determine with the SEETRAM monitor (see section 2.1.2), N_t is the number of atoms per unit of area, y measured yield of fragments corrected from secondary reactions by subtraction the yields obtained for the same nuclei in *empty target* measurements. This *empty target* measurements provide the production of residual nuclei in the different layers of matted located along of the beam-line. The factor C_f in equation 3.14 considers all corrections that are applied to the cross section in order to give us the real measure of this quantity. This factor is defined in the following way:

$$C_f = f_{dead} \cdot f_{ch.st} \cdot f_{sec} \quad (3.15)$$

The correction factors given in the equation 3.15 in the term C_f were the dead time of the acquisition system f_{dead} , f_{sec} which corrects the secondary reactions in the different material layers in the beam line and $f_{ch.st}$ takes into a count the production of ionic-charge states.

3.5.1 Background subtraction

In order to determinate the background contribution of the beam-line layers of matter we measured the production of the same nuclei without target without target. The actual cross section is written in the following way:

$$\sigma_t = \left(\frac{M_t}{d_t N_A} \right) (p_t - p_{empty}) \quad (3.16)$$

where M_t is the molar mass of the target material (g/mol), d_t is the target thickness (g/cm^2), and N_A is the Avogadro number (mol^{-1}) and p defined in following equation:

$$p = \frac{y}{N_p} \quad (3.17)$$

y is the number production yield of a given fragment and N_p the number of projectiles.

This correction factor represents is less than of 2 % for most of the reaction residues investigated in this work.

In a similar way it is possible it is possible to determine the production cross sections in ion-proton reactions combining the yields obtained with a CH_2 and a C target. In this case the carbon (C) is considered as the background. The principal way to subtract the C is using the following equation

$$\sigma_{proton} = \frac{1}{2} \left[\left(\frac{M_{CH_2}}{d_{CH_2} N_A} \right) (p_{CH_2} - p_{empty}) - \left(\frac{M_C}{d_C N_A} \right) (p_C - p_{empty}) \right] \quad (3.18)$$

where M_C and M_{CH_2} are the molar masses of the carbon a PE , σ_{proton} is the proton cross section.

3.5.2 Dead Time

One of the limitations while using very intense beams is the dead time of the data acquisition system. For this reason not all the events remain registered by the data acquisition. Thus we underestimate the yields the production residues. Dead time f_{dead} factor provides the fraction of accepted events from the ratio between the number of accepted and total triggers. This value was kept below the 30 % in order to obtain trustworthy measures of the number of events.

3.5.3 Secondary Reactions

The factor f_{sec} takes into account the secondary reactions that occur in the different layers of matter in the beam line. The reaction yields produced in the isobaric charge-exchange reaction can suffer secondary reactions after it leaves the target. Due to this fact the count realized in the corresponding focal plane is lower due to the loss of particles. In order to calculate this correction factor it is necessary to determine the total probability of interaction (σ_{tot}) in each material layer . The code Karol [111] was used in order

to obtain each σ_{tot} in each material layer. Hereby the factor of correction for secondary reactions is:

$$f_{sec} = \prod_{i=1}^n P_i \quad (3.19)$$

The factor P_i is the probability of survival in the matter layer i .

The average value of this correction was approximately of the 10 %. It is also possible to consider an additional factor related to the secondary reactions inside the target (f_t). But the nature of the isobaric charge-exchange reaction in this case should be neglected, so for this reaction the value of this factor is $f_t \sim 1$.

3.5.4 Ionic charge states

A nucleus produced in a reaction can change its charge due to the electromagnetic interaction with different atoms in the layers of matter across the beam-line [112]. This effect can alterate the measurement of the A/Q ratio and therefore affect the number of counts necessary for the determination of the cross section.

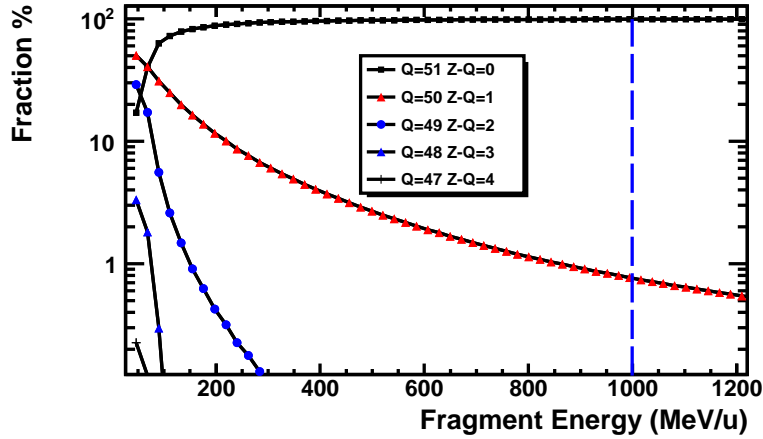


Figure 3.11: ^{112}Sb equilibrium charge distribution in the middle focal plane: Fraction of charge-states configurations as a function of fragment Energy. At 1 A GeV (vertical dashed lined) the charge state $Z - Q = 1$ have a probability around $\sim 1\%$ and the contribution of the other charge states are negligible at this energy.

In order to determine the charge states of the reaction residues in the first and second stages of FRS due to the layers placed in the focal planes we used the code GLOBAL. This is a program that determines the ionic charge-state

distributions of projectiles traversing solid and gaseous targets. The program was developed for the interaction of projectiles having a nuclear charge larger than 28 with any target. Details of the underlying physics as well as of a comparison between experiment and predictions by GLOBAL can be found in [113]. The contribution of ionic charge state correction in our experiment is always less than $\sim 1\%$ (see Fig 3.11).

3.6 Reactions using secondary beams

In the two step configuration the FRS was used as a two independent magnetic spectrometers. In the first stage we separated and identified the secondary beam of exotic projectiles. The second stage was used to investigate the residual nuclei produced in the interaction of the secondary beam with the reaction target at $S2$.

To measure the cross section with unstable beams we used the experimental set up described in the figure 2.7. The number of projectiles that impinges directly on the reaction target located in the intermediate focal plane is determined by the number of counts of a given nucleus in the corresponding identification matrix. To measure the fragments in the intermediate focal plane it is necessary to use different types of *triggers* and *downscaling* factors of these triggers in each focal planes.

One of the triggers was given by the scintillator placed at $S4$ (trigger==3). This trigger corresponds to those ions that arrived to the final focal plane of the FRS. All the detectors were registered by the data acquisition system (DAQ) when receive trigger==3 signal. The other trigger was given by the scintillator placed at $S2$ (trigger==1) which corresponded to particles that arrived to the dispersive focal plane at $S2$. If the DAQ was triggered by trigger==1, only the signals of the detectors of the first part of the experimental set-up were registered. This trigger was necessary for the determination of the number of incident projectiles for the determination of the fragmentation cross sections. Moreover, one has to consider the different dead times induced by these triggers.

We can determine these dead times from the direct comparison with its respective plastic scaler signal. Then in order to determine the cross section in the two step stage it is necessary to use this equation:

$$\sigma = \frac{y \cdot C_f \cdot Dt_{S4}}{N_t N_b \cdot Dt_{S2}} \quad (3.20)$$

where N_b is the number of projectiles, N_t is the number of atoms per unit of area in the target, y the production yield of the final fragments obtained

from the identification matrix at s4. Dt_{S2} and Dt_{S4} are the dead time of acquisition system at S2 and S4 respectively. The factor correction C_f used in the equation 3.20 for the reactions with secondary beams takes into account the particles that are produced in the reaction in S2 and that are identified in S4:

$$C_f = f_{ch.st} \cdot f_{sec} \quad (3.21)$$

The correction factors considered in this term of C_f are f_{sec} that correct the secondary reactions in the different material layers in the beam-line and $f_{ch.st}$ correct the production of the charge states.

CHAPTER 4

Isobaric Charge exchange reactions

As explained in chapter 1, charge exchange reactions manifest in two energy regimes: the low energy regime corresponding to nuclear excitations such as Gamow –Teller, spin-dipole etc, and a high energy regime induced by nucleonic excitations. Charge exchange reactions then constitute a useful tool in nuclear structure research. The (n,p) and (p,n) channels are often used to obtain the Gamow-Teller matrix elements which can not be extracted from β -decay experiments (see for example [76, 77]). At intermediate and high energies, above the pion production threshold, it is possible to use these reactions to excite nucleon resonances. In the particular case of high-energy charge-exchange reactions, the real pion produced must escape in order to preserve the isobar feature of this reaction.

This work offers a novel technique in order to understand the charge exchange with heavy ions with different targets and energies. With this systematic approach it is possible to study the isospin dependence of the charge exchange reactions, in particular for the inelastic channel.

We measured the isobaric proton and neutron charge exchange reactions induced by different Sn isotopes with the subsequent production of Sb and In residues. The high resolution of the FRS made it possible to disentangle the quasi-elastic and resonant processes leading to the formation of those residual nuclei. Moreover, the resolution of the measurement was improved using an unfolding technique. with the response function of the experimental setup.

In this chapter we will describe the results we obtained using two two physical observables: the recoiling energy spectrum of the reaction residues

and the cross section of two charge exchange reaction channels (np and pn).

4.1 Systematic study of isobaric charge exchange reactions at relativistic energies

Using the FRS it is possible to measure the n-p and p-n isobar charge-exchange channels in the same experiment. The isobar charge-exchange reaction of Sn projectiles produces two final residues of antimony and indium having the same number of nucleons as the projectile nuclei. The systematic study of the charge exchange reactions using projectiles with different neutron excess required the use of the one and two step configuration of the FRS that were explained in sections 2.3.1 and 2.3.2. In the one step configuration ^{112}Sn and ^{124}Sn stable beams were used to produce the charge exchange reaction while the two step configuration was used to study charge exchange reactions with unstable tin isotopes.

In the one-step reaction scheme a stable beam impinges a reaction target placed at the entrance of the FRS. In this case it is possible to identify the projectile reaction residues in the middle and the final focal planes of the spectrometer. In the two-step reaction scheme, the unstable isotope is produced at the production target located at the entrance of the FRS, and identified and separated using the first section of the FRS. Then, isobar charge-exchange reactions are induced in a second target placed at the intermediate image plane. The reaction fragments are identified with the second section of the spectrometer.

In addition to the systematic analysis using different projectiles, we studied the dependence of the isobar charge-exchange reactions with the nature of the target and the beam energy. These measures were performed using the one step set-up of the FRS. The objective of the analysis with stable projectiles on different targets is to study the dependence of charge exchange reaction with the target mass [89, 90, 114]. On the other hand, the energy dependence was investigated in order to understand the dependence of the nucleonic resonances excitation with the beam energy. Table 4.1 summarizes the experimental charge exchange reactions measured in this work.

Figure 4.1 illustrates the clear identification plot obtained for the two isobar charge-exchange projectile residues (p,n) and (n,p) produced in the reaction $^{112}\text{Sn} + C$ obtained with the FRS.

This identification allowed us to determine, with high precision, the production cross-sections of all the single charge exchange residues created in peripheral reactions of Sn projectile with different targets following the pro-

Target Place	Beam	E_b (A MeV)	Thickness(mg/cm^2)	Fragment
S0	^{112}Sn	1000	C(100)	$^{112}Sb, ^{112}In$
			PE(95)	
			Cu(373)	
			Pb(255)	
S0	^{124}Sn	1000	C(197)	^{124}Sb
			PE(95)	
			Cu(373)	
			Pb(954)	
S0	^{112}Sn	700 400	C(100)	$^{112}Sb, ^{112}In$
			PE(95)	
S2	^{110}Sn	1000	C(910)	^{110}Sb
	^{120}Sn		C(1400)	$^{120}In, ^{120}Sb$
	^{122}Sn			^{122}Sb

Table 4.1: Charge exchange reactions investigated in this work.

cedure described in section 3.5 .

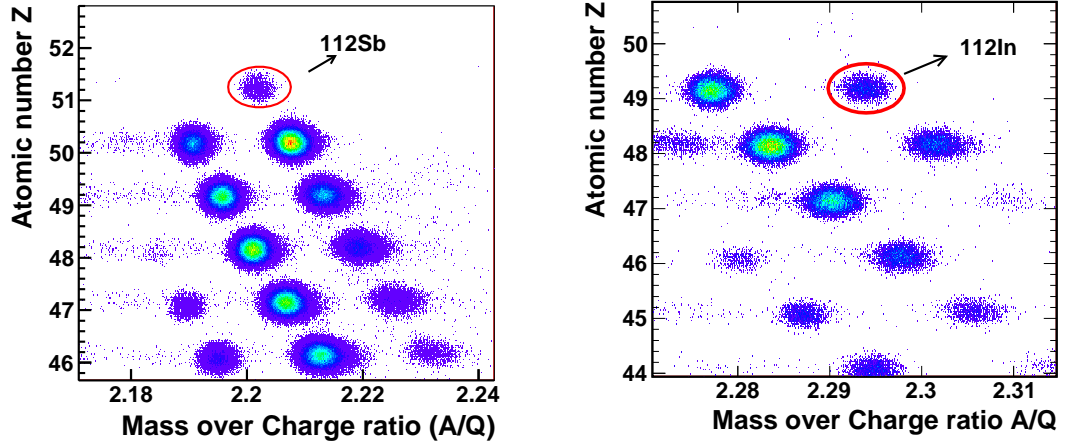


Figure 4.1: Atomic number (Z) as a function mass-over-charge ratio A/Q of fragments produced in the reaction $^{112}Sn + C$ at 1 A GeV. Left panel: n - p channel production (^{112}Sb). Right panel : p - n channel production (^{112}In).

4.2 Recoiling energy distributions of projectile residues

In order to investigate the isobar charge exchange reaction mechanism we propose to use as observable the recoiling energy of the projectile residues in the reference frame defined by the velocity of the projectiles in the middle of the target. Since those spectra represent the kinetic energy lost by the projectiles in the reaction they are called missing energy spectra. Figure 4.2 shows the missing energy spectra for ^{124}Sb . In this figure we can observe two bumps, one around 0 MeV energy value corresponding to quasi-elastic charge exchange processes and a second one around ~ -250 MeV corresponding to charge-exchange processes where the projectile lose quite some kinetic energy.

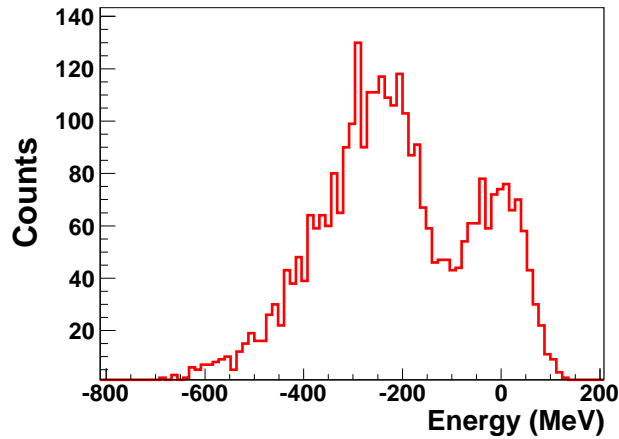


Figure 4.2: Missing energy spectrum for ^{124}Sb in the reaction $^{124}\text{Sn}(C, X)^{124}\text{Sb}$ at 1 A GeV in the beam-particle frame.

The quasi-elastic peak corresponds to nuclear isovector transitions at low energy, as was explained in the chapter 1. The physical process that contribute to the quasi-elastic region are Fermi, Gamow–Teller, spin dipole and giant dipole transitions principally [77]. Figure 4.3 is a schematic representation of the $n - p$ and $p - n$ quasi-elastic channel mediated by the exchange of a the virtual pion exchange in the quaselastic region. These $\Delta T = 1$ transitions are responsible of the excitation of the collective modes excitations mentioned above.

The second contribution in the missing energy spectra corresponding to large values of energy lost in the reaction, corresponds to nucleon excitations.

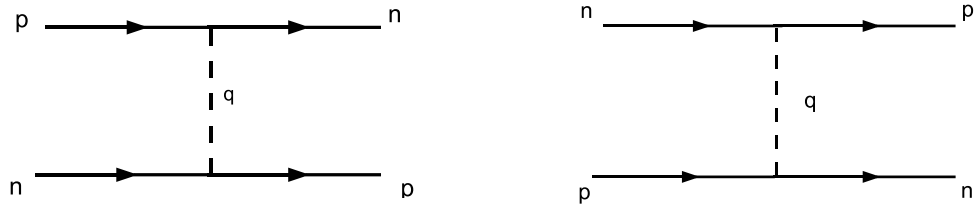


Figure 4.3: Schematic representation of $n - p$ and $p - n$ channel through of the virtual pion exchange in the quaselastic region.

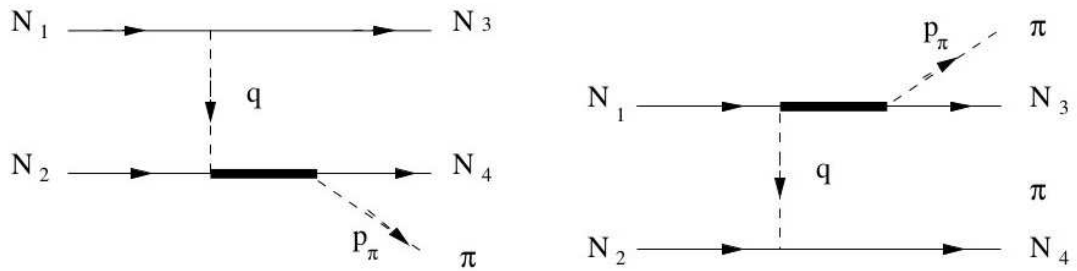


Figure 4.4: Schematic representation of the real pion exchange in the inelastic region. The top part of each the diagram represents the projectile, while the bottom one is the target. Left panel: nucleon resonance excitation in the target (solid line) with the subsequent pion and nucleon emission. Right panel: nucleon resonance excitation in pion the excitation in the projectile.

Figure 4.4 represents the resonance excitation with the real pion production in the target and the projectile. We observe the inelastic region due to the fact that the real pion produced in the nucleon resonance decay leave the nucleus in order to preserve the isobaric condition of this reaction. The pion carries charge and energy. Momentum and energy conservation translates as a projectile charge exchange and recoil leading to negative values in the missing energy spectra.

We measured inclusive cross section of the inelastic channel. Indeed the inelastic peak is a contribution of the different nucleon resonances as shown the tables 4.2 and 4.3. Moreover, we also have contributions from nucleon resonances excited in the target and projectile nuclei.

As discussed in chapter 3, due to our energy resolution around ($\Delta E/E \sim$

Excitation in the Target	I.C.	Excitation in the Projectile	I.C.
$\Delta(1232)$			
$p(n, p)\Delta^0 = p(n, p)n\pi^0$	2/3	$p(n, \Delta^0)p = p(n, p\pi^-)p$	$\sqrt{(2)}/3$
$p(n, p)\Delta^0 = p(n, p)p\pi^-$	$\sqrt{(2)}/3$	$p(n, \Delta^+)n = p(n, p\pi^0)n$	-2/3
$n(n, p)\Delta^- = n(n, p)n\pi^-$	$\sqrt{(2)}$	$n(n, \Delta^0)n = n(n, n\pi^-)n$	$-\sqrt{(2)}/3$
Roper $N^*(1440)$			
$p(n, p)P_{11}^0 = p(n, p)n\pi^0$	-2	$p(n, P_{11}^0)p = p(n, p\pi^-)p$	$-\sqrt{(2)}$
$p(n, p)P_{11}^0 = p(n, p)p\pi^-$	$2\sqrt{(2)}$	$p(n, P_{11}^+)n = p(n, p\pi^0)n$	-2
—	—	$n(n, P_{11}^0)n = n(n, p\pi^-)n$	$\sqrt{(2)}$

Table 4.2: Elementary process for the Δ and Roper resonances produced in (n, p) reaction and its respective isospin coefficients I.C.

Excitation in the Target	I.C.	Excitation in the Projectile	I.C.
$\Delta(1232)$			
$p(p, n)\Delta^{++} = p(p, n)p\pi^+$	$\sqrt{(2)}$	$p(p, \Delta^+)p = p(p, n\pi^+)p$	$-\sqrt{(2)}/3$
$n(p, n)\Delta^+ = n(p, n)n\pi^+$	$\sqrt{(2)}/3$	$n(p, \Delta^+)n = n(p, n\pi^+)n$	$\sqrt{(2)}/3$
$n(p, n)\Delta^+ = n(p, n)n\pi^0$	-2/3	$n(p, \Delta^0)p = n(p, n\pi^0)p$	2/3
Roper $N^*(1440)$			
$n(p, n)P_{11}^+ = n(p, n)n\pi^+$	$2\sqrt{(2)}$	$p(p, P_{11}^+)p = p(p, n\pi^+)p$	$-\sqrt{(2)}$
$n(p, n)P_{11}^+ = n(p, n)p\pi^0$	-2	$n(p, P_{11}^+)n = n(p, n\pi^+)n$	$\sqrt{(2)}$
—	—	$n(p, P_{11}^0)p = n(p, n\pi^0)p$	-2

Table 4.3: Elementary process for the Δ and Roper resonances produced in (p, n) reaction and its respective isospin coefficients I.C.

12 MeV) it is not impossible to disentangle each isovector transitions components in the quasi-elastic region.

It is important to mention that in this experiment the information on reactions induced by a proton was obtained subtracting the contribution of the carbon target from the polyethylene (PE) target. This subtraction includes the scaling of each energy distributions using the procedure explained in the section 3.5.1. Figure 4.5 illustrate this procedure where the proton information is obtained from the subtraction of the two unfolded distributions.

4.2.1 Comparison with previous experiments

The inelastic channel in isobar charge-exchange reactions can be used to investigate the in-medium behavior of the Δ resonance. For these reason, a

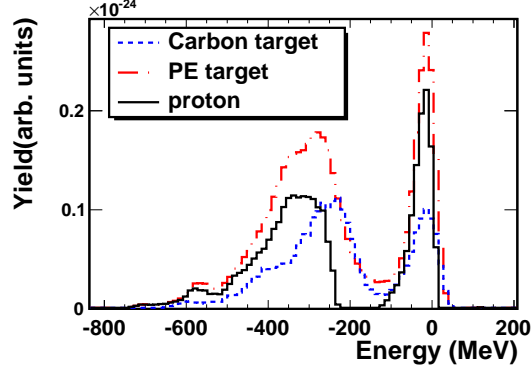


Figure 4.5: Subtraction process of the two unfolded distributions in order to obtain the proton target information in the production of ^{124}Sb at 1 A GeV

complete program to measure the Δ excitation in nucleus-nucleus collisions of different light and medium mass projectiles was carried out at the accelerator SATURNE in Saclay [89]. In this program reactions using ^6Li , ^{12}C , ^{16}O , ^{20}Ne , and ^{40}Ar projectiles at energies around 1 A GeV ([90, 114]) were investigated.

As in our case, the observable used to investigate these reactions was the missing energy spectra of the projectile residues. These missing energy spectra were obtained from the longitudinal momentum of the projectile residues measured with the spectrometer SPES IV with a typical resolution $\Delta p/p = \pm 7 \times 10^{-4}$. More recently, the FRagment Separator (FRS) at GSI (Darmstadt) was also used to investigate charge exchange reaction using heavy ions [115]. In this case, a Pb beam at 1 A GeV was used to induce isobaric charge-exchange reactions in proton, deuterium, and titanium targets, leading to the production of ^{208}Bi . The recoiling nuclei were isotopically identified with the FRS. The corresponding longitudinal-momentum distributions showed two components that were associated to quasi-elastic and inelastic charge-exchange reaction channels.

Figure 4.6 shows a qualitative comparison between missing energy spectra of charge-exchange reaction results obtained in Saturne with a ^{20}Ne beam at 900 A MeV [89, 90, 114] and this work with a ^{112}Sn beam at 1000 A MeV. The figure shows qualitative good agreement between the Saturne results and ours.

In both experiments it is possible to disentangle the quasi-elastic and inelastic charge-exchange channels. It is important to note the absence of the quasi-elastic peak in the pn channel production with the proton targets. This effect is explained by the charge conservation in this reaction.

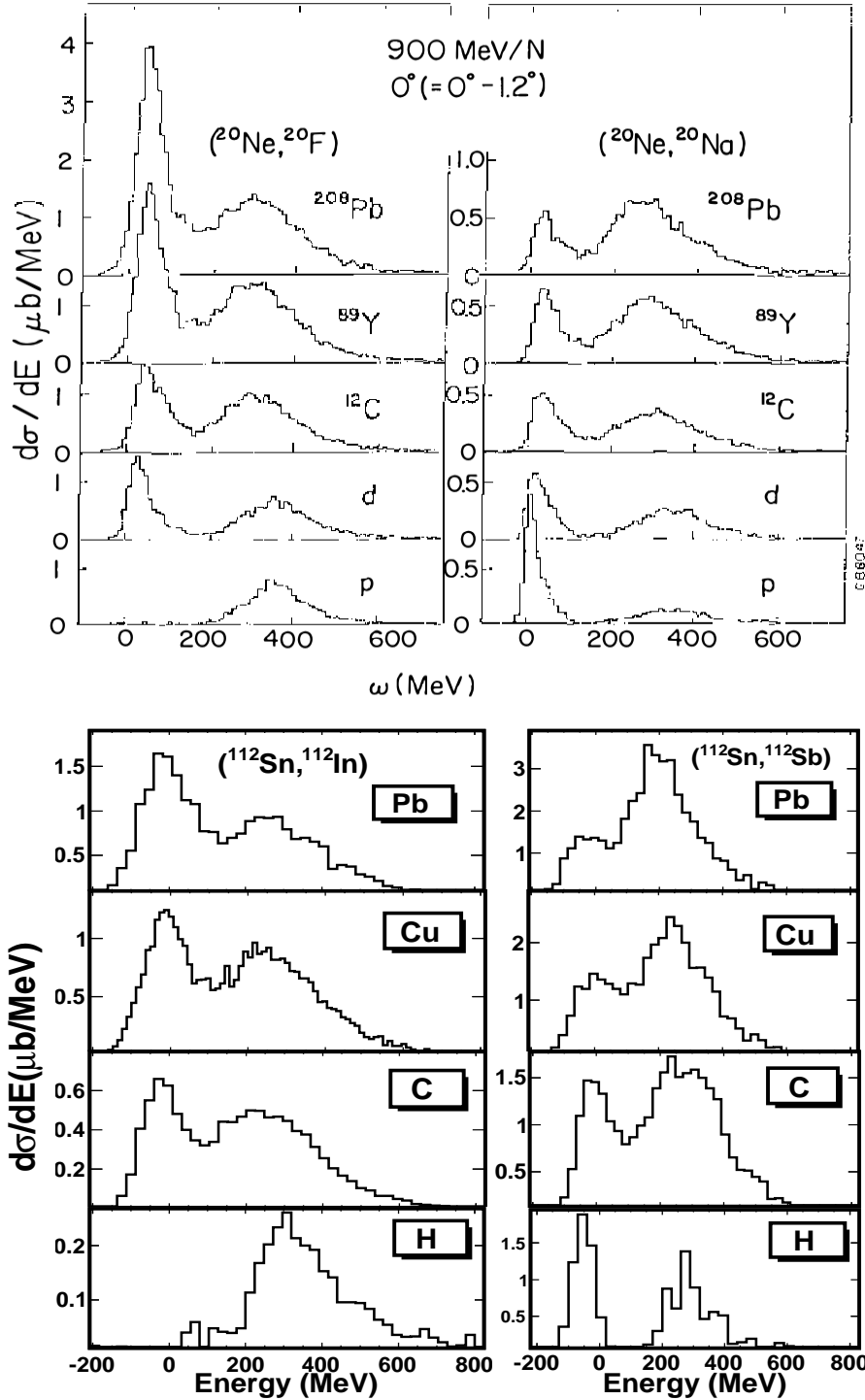


Figure 4.6: Comparison between missing energy distributions from e Saturne [89] and this work results. Top panel: Zero-degree spectra for charge exchange reactions with a ^{20}Ne beam at 900 A MeV. Bottom panel: Missing energy spectra for charge exchange reactions with a ^{112}Sn beam at 1 A GeV.

By direct comparison, it is possible to observe that in the previous Saturne measurements and in the results obtained in this work, the Δ - resonance production represents a significant part of the spectra in each case. In the both experimental results, the pn channel shows a higher contribution of the quasi-elastic channel with respect to the inelastic channel. The opposite effect is seen in the np channel.

The isospin systematic using different targets study shows us a clear dependence with the mean energy of each distribution which looks similar in both sets of data. Moreover, in both cases the peak corresponding to the Δ resonance excitation is downshifted by some 70 MeV with respect to the value obtained in the proton target collisions. This effect will be discussed in the section 4.5.

4.2.2 Results of reactions using stable beams

In this experiment we used beams of two stable isotopes of tin, ^{112}Sn and ^{124}Sn . For these measurements the reaction target was placed at the entrance of the fragment separator. In this case we were not limited by the intensity of the beams, therefore we could use rather thin targets improving the resolution of the measurement as discussed in section 3.2. Table 4.1 shows the complete list of targets and beam energies used in our measurements.

Figs. 4.7 and 4.8 display the missing energy spectra obtained with these two beams on different targets. As can be seen, with the ^{112}Sn beam we could measure the two isobaric charge-exchange channels leading to the production of ^{112}In (p,n) and ^{112}Sb (n,p). However, with the ^{124}Sn beam we only measured the (n,p) channel producing ^{124}Sb . In these figures the black histograms represent the missing energy spectra as obtained from the measured longitudinal momentum distributions following the procedure described in section 3.3.

The dashed line corresponds to the unfolding of the spectra by the response function of the experimental setup defined from measurements with the primary beam using the procedure described in section 3.3.3.

For all the targets and beams we clearly identify the quasi-elastic and inelastic channels of the charge-exchange reaction.

The figures also illustrate the improvement in resolution brought by the unfolding of the response function of the experimental setup.

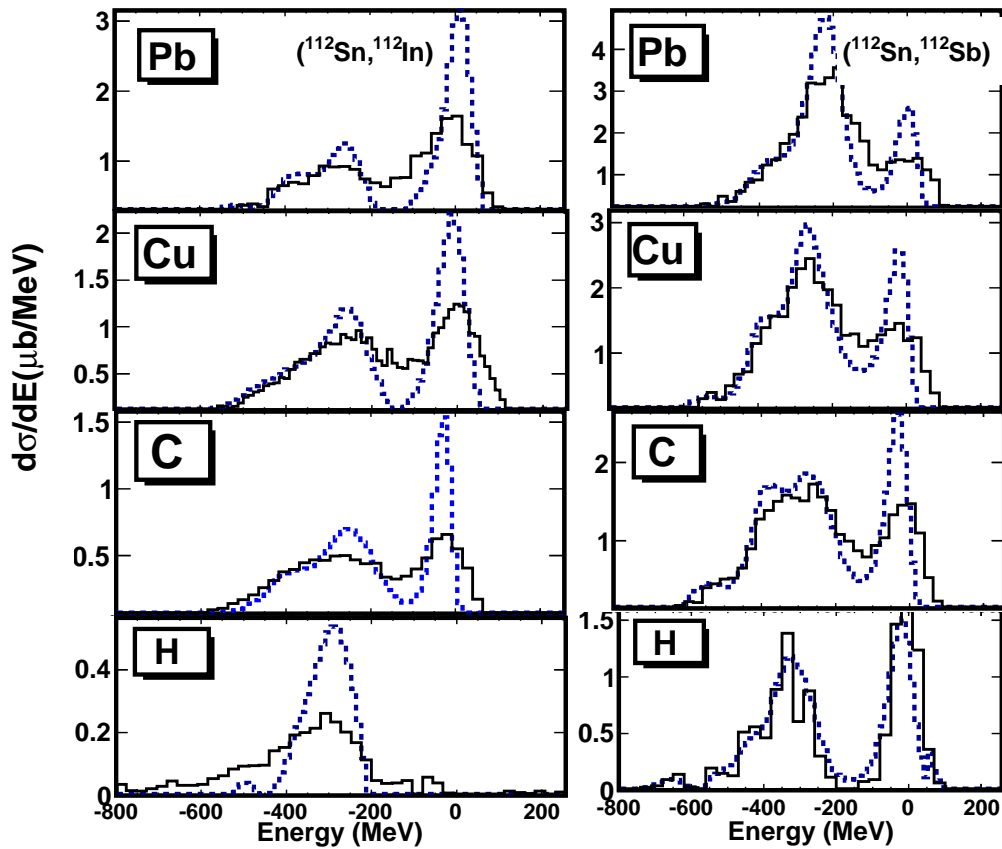


Figure 4.7: Energy missing spectra in the beam particle frame. For (p,n) (^{112}In spectra) and (n,p) (^{112}Sb spectra) isobaric charge-exchange reactions induced by ^{112}Sn projectiles at 1000 A MeV. The solid line represents the measured spectra and the dashed line the unfolded one.

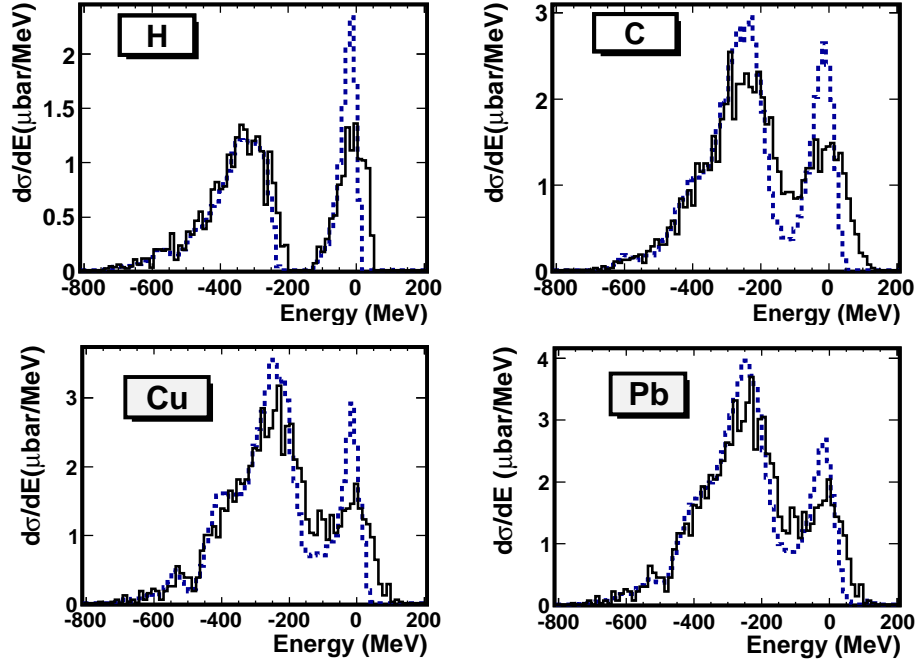


Figure 4.8: Energy missing spectra of ^{124}Sb produced in (n,p) isobar charge-exchange reactions induced by ^{124}Sn projectiles at 1000 A MeV on different targets. The solid line histogram corresponds to the measured spectra and the dashed ones to the unfolded spectra.

The experimental setup also allowed us to determine the cross sections of these reactions channels using the method described in the section 3.5. Indeed, Figs. 4.7 and 4.8 are normalized to the corresponding cross sections that are listed in table 4.4 with the corresponding uncertainties. Moreover, in Fig. 4.9 we depict the evolution of the cross sections of the two isobar charge-exchange channels with the mass number of the target nuclei for the two stable projectiles (^{112}Sn and ^{124}Sn) at 1000 A MeV . The figure shows a clear increase of the charge-exchange reaction cross section with the mass number of the target nuclei for the two isobar charge-exchange channels and for the two projectiles. However, one observes that the cross sections are larger for the (n,p) channel and for the ^{124}Sn projectiles for all the targets.

The larger cross sections for the (n,p) channel (around a factor two larger than the (p,n) channel) could be understood as due to the larger density of neutrons at the surface of both projectiles. The same reason would explain the larger cross sections measured with ^{124}Sn than with ^{112}Sn . The peripheral character of these reactions would correspond to an increase of

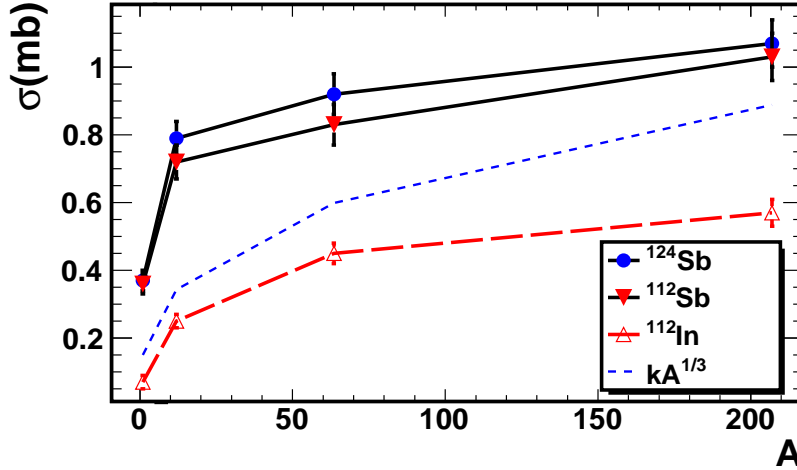


Figure 4.9: Total cross section as a function of the target mass number A .

the cross sections with the radius of the target nuclei and then with $\propto A^{1/3}$. Such an evolution is represented in Fig. 4.9 by the dashed line. However, the measurements show a smoother evolution of the cross sections than expected with this simple model. Therefore, a detailed description of this reaction mechanism is required for a complete understanding of these cross sections.

Using the fitting results explained in the section 4.5.1 it is possible to disentangle each peak and calculate their respective cross section contributions. With these values it is possible to study the evolution with the target mass of each component.

Figure 4.10 shows the evolution of the cross sections with the target mass number for the elastic (upper panel) and inelastic (bottom panel) isobar charge-exchange reaction channels.

The figures show that the elastic and inelastic (p,n) cross sections are rather similar and evolve smoothly with the target mass number. The cross sections for the (n,p) channel (Sb) are however, a factor two to three larger for the inelastic channel than for the elastic one. Here we also observe an important increase of the cross sections between the proton target and the heavier ones. For the heavy targets the evolution of the cross sections with the target mass number increases smoothly.

The large difference in cross section between the (p,n) and the (n,p) inelastic channels could be due to the larger abundance of neutrons at the periphery of the tin projectiles. However, the small difference between the cross sections measured with ^{124}Sn and ^{112}Sn would indicate the role of other

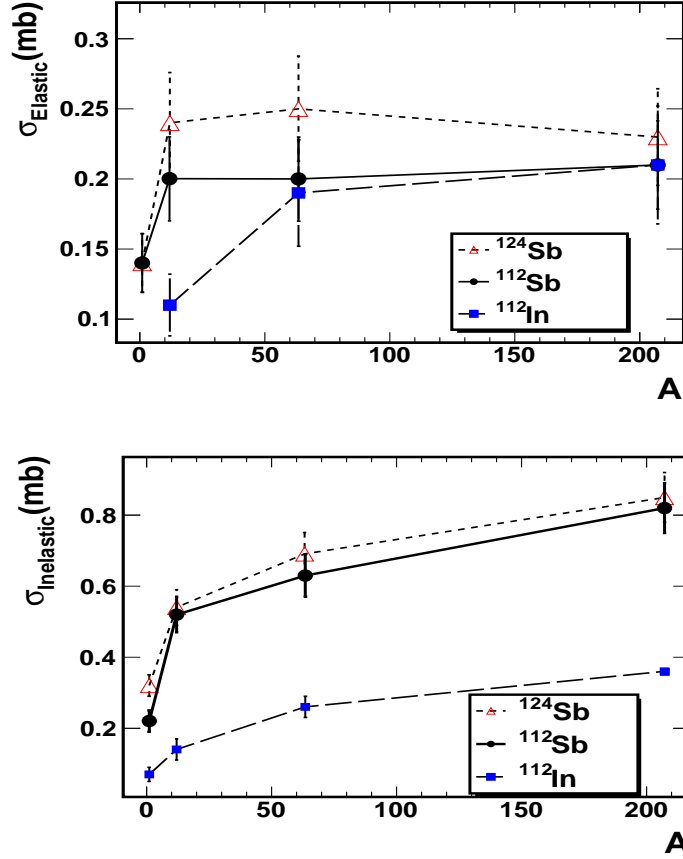


Figure 4.10: Cross section of the elastic (top panel) and inelastic (bottom panel) channels as a function of the target mass A in the reaction of different Sn beams at 1 A GeV.

mechanisms to explain these differences.

4.2.3 Results of reactions using unstable beams

Charge-exchange reactions induced by secondary beams of ^{122}Sn , ^{120}Sn and ^{110}Sn produced by fragmenting ^{124}Sn and ^{112}Sn projectiles were also investigated in this work. The secondary beams were produced in a 4 g/cm^2 beryllium target placed at the entrance of the FRS. The first half of the spectrometer was used to separate and identify the secondary beams. Charge-exchange reactions of these secondary projectiles were induced in C targets (1.4 and 0.92 g/cm^2) located at the intermediate image plane of the spectrometer. The final reaction residues were then identified with the second

section of the spectrometer.

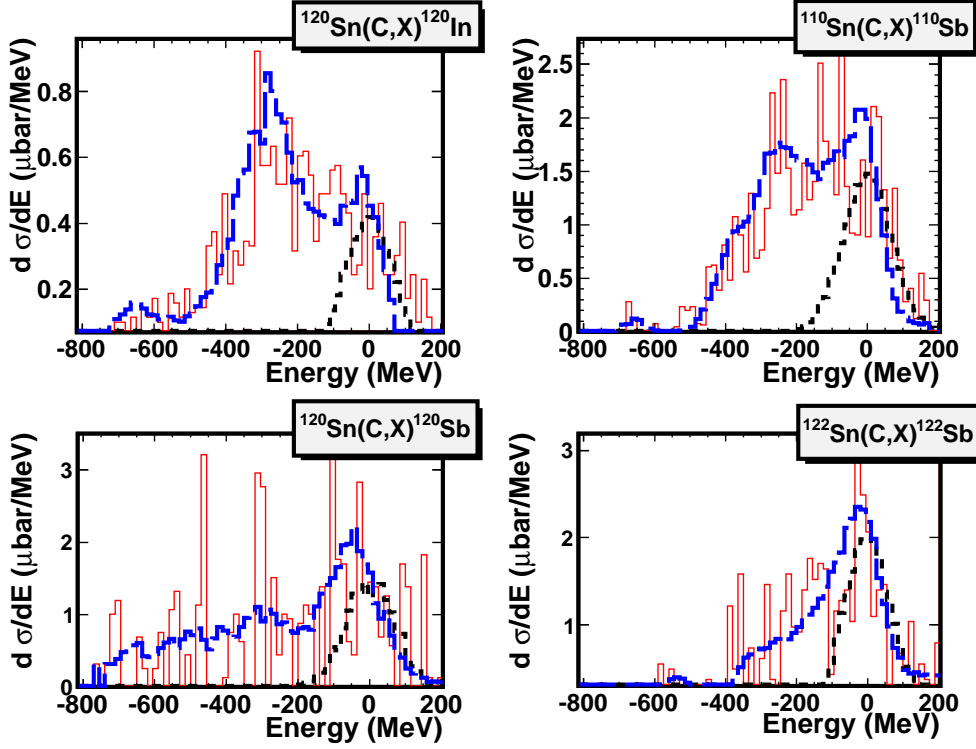


Figure 4.11: Missing energy spectra of Sn secondary beams at 1 A GeV on C target: Total distributions (histograms) and unfolded distribution (dashed line). The beam energy spectrum is also shown in the figure (dotted line).

In this case the longitudinal momentum of the projectile residues were determined taking into account their positions at the intermediate and final image planes and the dispersion in the second section of the spectrometer according to the equation 2.10.

In Fig. 4.11 we display the missing energy spectra (histograms) of several charge-exchange projectile residues produced at the intermediate image plane of the spectrometer by secondary projectiles. These spectra were obtained from measurements of the corresponding longitudinal momenta at the final image plane of the spectrometer as previously explained.

The measurements with secondary beams suffer from the much lower intensities. To compensate this drawback thicker reaction targets are required resulting in a poorer momentum resolution as discussed in section 3.2 .

As a demonstrate the reference [106] critical parameters that affect the deconvolution are the statistical fluctuations and the target thickness. These

effects degrade the unfolding solution.

These measurements demonstrate that the target thickness and the statistics are important factors in order to obtain optimal spectrum measurements. Future experiments using secondary beams will require take into account these experimental factors.

Using the method described in the section 3.6 it is also possible to determine the charge-exchange cross sections with unstable beams impinging on carbon target with a thickness of 1.4 g/cm^2 of thickness placed at the intermediate focal plane S2 of the spectrometer. The results are summarized in table 4.4.

Secondary Beam	Reaction Product	Cross section (mb)
^{120}Sn	^{120}Sb	0.79 ± 0.17
^{122}Sn	^{122}Sb	0.76 ± 0.19
^{110}Sn	^{110}Sb	0.75 ± 0.17
^{120}Sn	^{120}In	0.29 ± 0.07

Table 4.4: Measured charge exchange reaction cross sections using unstable beams at 1 A GeV

The results are compatible with the cross section obtained when a stable beam was impinging a target at S0. Again, the difference between the cross section value of Sb (np channel) is higher than In (pn) cross section value which indicated the strong dependence of the cross section with the content of proton and neutrons in the nucleus of target.

4.3 Quasielastic channel

At low energy , charge exchange reactions excite collective spin-isospin modes as was presented in chapter 1. There are several methods to measures these excitations modes. One of them is to reconstruct the missing energy spectrum of the fragment produced in the reaction. This technique requires energy resolutions better than $\sim 1 \text{ MeV}$ as shown in [81, 88]. Another possibility is measuring the de-excitation energy spectrum of the nucleus produced in the isovector transition as shown the reference in the reference [77] and references cited therein. We will further discuss the first method that is the one followed in this work.

DWIA (Distorted Wave Impulse Approximation) approach allows to identify the initial and final states of this isovector transition (spin and parity). The angular momentum (L) transferred in the transition can be deduce from

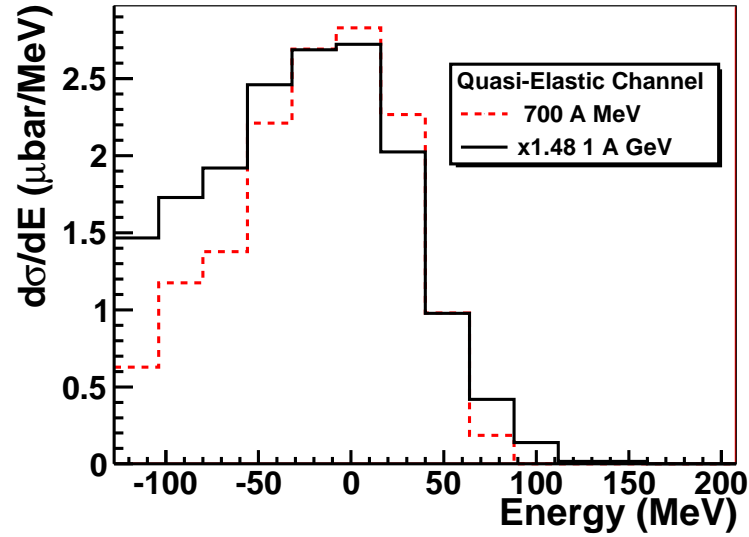


Figure 4.12: Comparison missing energy distribution of the two quasielastic energy distributions at two different energies (700 A MeV and 1 A GeV).

the comparison between the experimental differential cross-sections as a function of the angle with the theoretical calculations (DWIA).

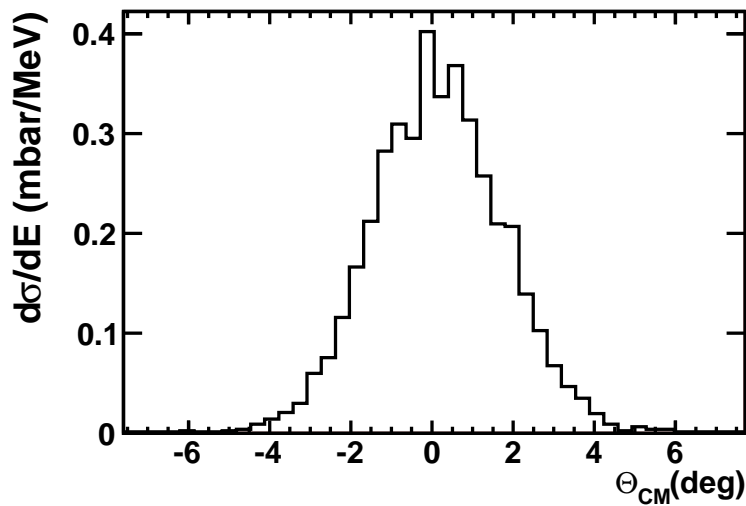


Figure 4.13: Angular Distributions of $^{112}\text{Sn}(C, X)^{112}\text{Sb}$ at 1 A GeV in the CM frame

Figure 4.12 shows missing energy distributions at two different beam energies obtained in our work. In this plot, it is impossible to observe any substructures associated with isovectorial transitions due to the limited energy resolution that we could achieved ($\Delta E/E \sim 12$ MeV). Moreover, we do not have access to the complete angular distributions but only to the inclusive total cross-section around 0 degrees as shown in Fig. 4.13 for the reaction $^{112}\text{Sn}(C, X)^{112}\text{Sb}$ at 1 A GeV. Those effects prevent us to exploit the information of the quasi-elastic channel in the way it was shown in reference [77]. The figure 4.13 shows the angular distribution in the reaction $^{112}\text{Sn}(C, X)^{112}\text{Sb}$ at 1 A GeV.

4.4 Sensitivity to the radial distributions of proton and neutrons

As previously discussed, the isobaric character of the charge-exchange reactions investigated in this work represents an important selection of the impact parameter. The strong absorption characterizing the nuclear interaction at relativistic energies and the propagation of pions in the nuclear medium guarantee the peripheral nature of this reactions. Moreover, the possibility of measuring both charge-exchange channels in the same experiment may give access to the relative content of protons and neutrons at the nucleus surface.

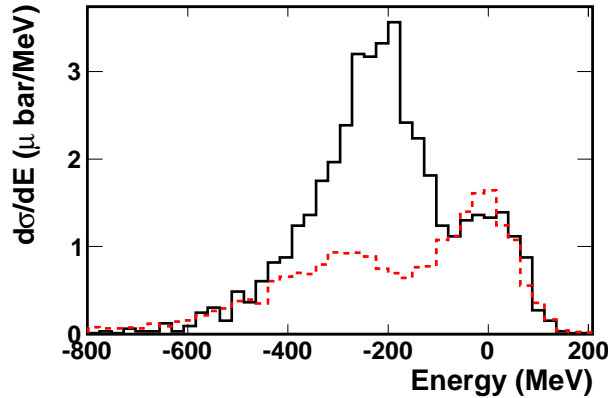


Figure 4.14: Comparison between the np channel: ^{112}Sb (solid line), and pn channel: ^{112}In (dashed line) energy distributions in the reaction of the ^{112}Sn on carbon target at 1 A GeV.

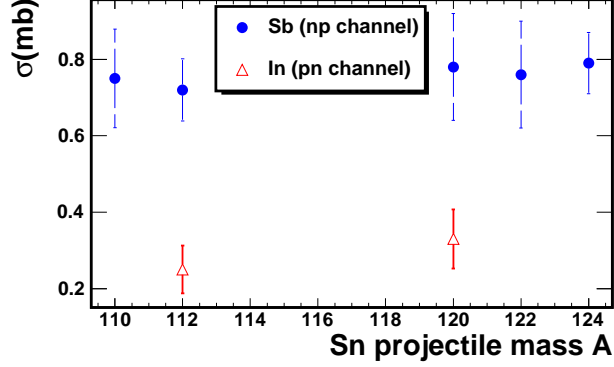


Figure 4.15: Cross section of the Sb (np channel) and In (pn channel) produced by the Sn beams reaction on carbon target as a function of the target mass.

In the inelastic channel it is more sensible to the target mass dependence. It is clear that the inelastic cross section it is more sensible to the proton an neutron number in the projectile and the target. With the difference between the projectile nucleon in the projectile we observe by direct comparison the change cross section in the ^{112}Sn and ^{124}Sn . For example in the figure 4.14, by direct comparison between the p-n and n-p channels we notice the n-p inelastic peak is lower that p-n channel. The reason is that the Pb target is a reach neutron nucleus and it has fewer proton interaction with the projectile. This fact is a signature that the charge exchange reactions are sensible to the nucleons quantity in the periphery where the nuclear density is lower.

Figure 4.15 shows a clear difference between total cross section the Sb and In production in the reaction of the different Sn projectiles on carbon target. The average ratio between this cross sections is around $R_{\frac{np}{pn}} = 2.4$. This fact reveal again the sensibility that the charge exchange reaction to the proton and neutron content in the nucleus. A qualitative analysis of the relative resonance production for each channel (see tables 4.2 and 4.3) calculated as the ratio of the respective np and pn channels $R_{\Delta-N^* \frac{np}{pn}} = 1.19$ and the effect neutron/proton ratio ($R_{\frac{n}{p}}$) provide us information about of the effects in the periphery. For example in the carbon target case is $R_{\frac{n}{p}} = 1$ and the ratio of the respective np and pn channels do not explain the experimental factor observed in the experiment. A plausible hypothesis is the existence of the nuclear skin. Theoretical calculations in this way will clarify this effect.

4.5 Excitation of baryon resonances in the nuclear medium

In this section we will analyze in detail the energy missing spectra of the inelastic charge-exchange channel in order to characterize the corresponding subnucleonic excitations.

4.5.1 Evidences for the excitation of different resonances

The inelastic charge-exchange channel corresponds to nucleon excitations as was explained in chapter 1.

Using the unfolding technique it is possible to improve the resolution of the missing energy spectra measured with the FRS. As can be seen in Fig 4.16, the improved resolution not only allow us to disentangle the two energies regions (the quasi-elastic and inelastic peak), but also reveal additional structures in the inelastic region that we will associate to different nucleon excitations or resonances.

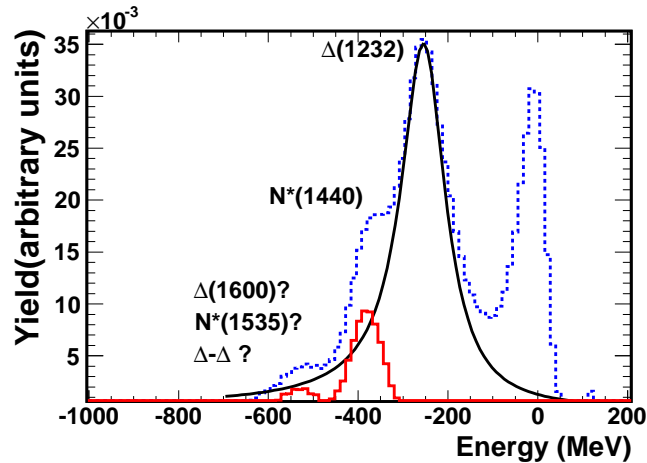


Figure 4.16: Unfolded energy spectrum in the $^{112}\text{Sn}(\text{Cu}, X)^{112}\text{Sb}$. Additional resonant components in the inelastic channel are shown. The Δ resonance (solid line) subtraction give us an idea of additional baryon resonant (dashed line). In this work was not possible to assign the third peak from the possible formation of $\Delta(1600)$, $N^*(1535)$, or a double Δ production.

The analysis of these structures in terms of mean energy and width allow us to clearly identify the Δ resonance as the main contribution to the inelastic

charge-exchange peak, but we also identify the contribution of the Roper resonance and even a third contribution that we could not yet attribute to any known resonance. These data could then contribute to investigate in-medium effects in baryons.

In the following subsections we will present the arguments supporting the identification of these nucleonic resonances. These arguments are the mean energy and width of the resonances obtained fitting the inelastic charge-exchange missing energy spectra and the evolution of these contributions to the spectra with the energy of the projectile and the nature of the target.

Fitting Procedure

The identification of the nucleon excitations contributing to the inelastic charged-exchange reactions requires the determination of its mean and width energy obtained fitting the inelastic part of the measured missing energy spectra.

To perform this fit we choose based on generalized Breit-Wigner functions. A detailed description of this method appears in [116]. This method works with asymmetric Breit Wigner functions and it is possible to extract the fit parameters with high accuracy.

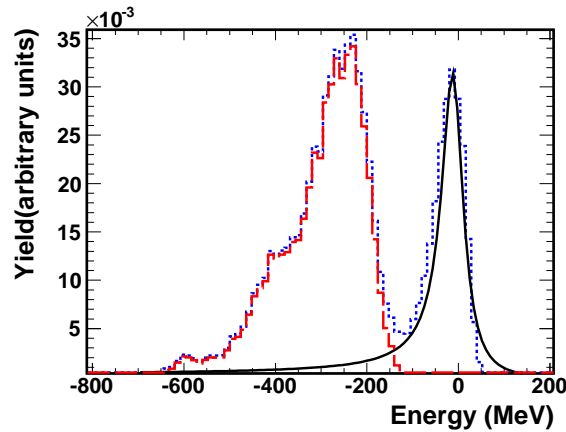


Figure 4.17: Subtraction of the elastic region in the unfolded energy-recoil nucleus spectrum (dotted line) in the reaction $^{124}\text{Sn}(C, X)^{124}\text{Sb}$ at 1 A GeV. The solid line indicate the elastic fit and the inelastic energy region (dashed line) is a distribution without elastic component.

In our case, the generalized Breit-Wigner $f(E)$ applied to the the unfolded distributions (see section 4.2) is:

$$f(E) = A \cos^2(\beta + \delta) \quad (4.1)$$

with $\beta = \arctan(2(E - E_0)/\Gamma)$. E_0 and Γ are the of the resonance and width of the Breit-Wigner distribution. A is the amplitude of the distribution and δ is a parameter describing the asymmetry of the fit function. When this parameter has a value $\delta = 0$ the distribution has a Lorentz-shape function.

Equation 4.1 gives us a powerfull tool in order to investigate the elastic and inelastic regions. When performing the fit of the distribution it is important to note that the elastic channel can affect the inelastic region. To minimize this contribution, first, we fitted the elastic region, and with the resulting function, we subtract the elastic component to the total missing energy spectra. Figure 4.17 illustrates an example of subtraction of the elastic channel with the objective to obtain the inelastic channel without elastic interference component. Using this fit function we found the results that appear in the figure 4.18 and 4.19.

Then, we can fit the inelastic part using the combination of three generalized Breit-Wigner functions. Each individual component is interpreted as a different nucleon excitation. As we already said, the main component is the Δ resonance. We also have clear evidences for the presence of the Roper N(1440) resonance.

Finally we observed a third contribution not fully identified that can be a double Δ resonance excitation or another resonance close to the Roper e.g. $\Delta(1600)$ $N^*(1535)$. The table 4.5 summarizes the fit parameters of $f(E)$ (equation 4.1) obtained from the fit of the energy distributions 4.18 and 4.19.

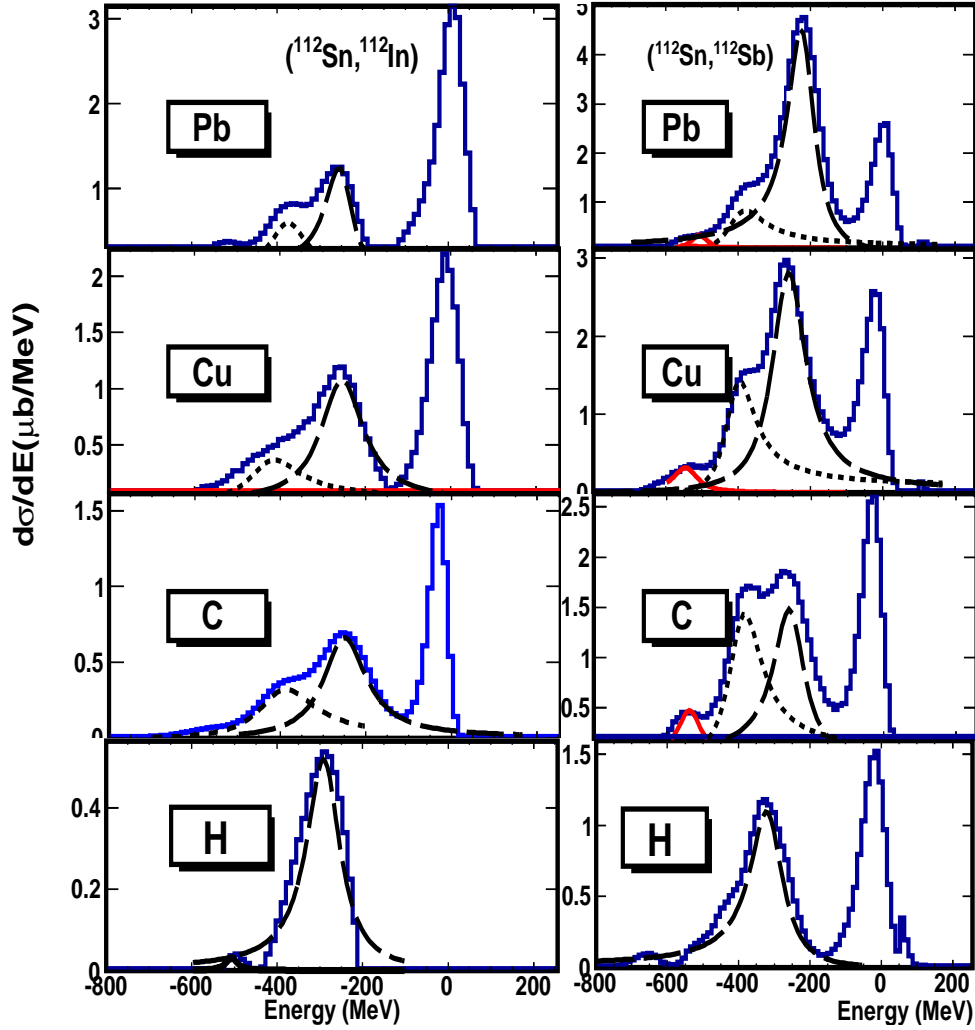


Figure 4.18: Breit Wigner fits for ^{112}Sn charge-exchange reaction products: These plots represent the recoil energy distribution (solid line) of the charge exchange reaction residues in the beam particle frame. In the inelastic region, above the pion production threshold, it is possible to excite the Δ and the Roper resonances. In each plot, the contribution of each resonant component is shown. The dashed line is corresponded to Δ - resonance while the dotted line represents the Roper resonance.

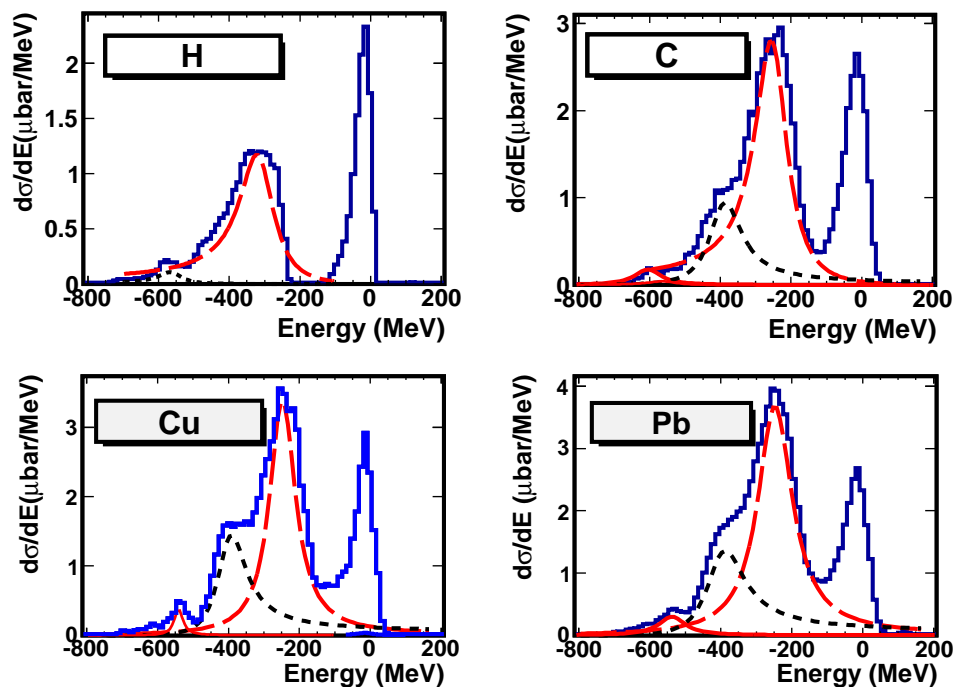


Figure 4.19: Breit Wigner fits for the (n,p) channel of ^{124}Sn : These plots represent the recoil energy distribution (solid line) of the ^{124}Sb in the beam particle frame. The dashed line is the Δ^- resonance component and the dotted line represents the Roper resonant component.

Resonance	$E_0(MeV)$	$\Gamma(MeV)$	\mathbf{A}	δ
$^{124}Sn(H, X)^{124}Sb$				
Δ	-320±23	131±26	1.19	0.03
Roper	-562.±40	86± 30	0.011	0.13
$^{124}Sn(C, X)^{124}Sb$				
Δ	-238±24	112± 25	0.03	0.35
Roper	-393±30	110± 25	0.01	-0.11
3rd peak	-599±40	67±18	0.0015	0.087
$^{124}Sn(Cu, X)^{124}Sb$				
Δ	-245±23	110±25	0.041	-0.018
Roper	-407±43	95± 22	0.017	-0.19
3rd peak	-538±79	35±10	0.005	-0.094
$^{124}Sn(Pb, X)^{124}Sb$				
Δ	-248±27	92±22	0.045	-0.0014
Roper	-391±38	123± 28	0.0179	-0.1336
3rd peak	-548±82	43±10	0.0022	-0.086
$^{112}Sn(H, X)^{112}Sb$				
Δ	-314±26	124± 29	1.200	0.0001
$^{112}Sn(C, X)^{112}Sb$				
Δ	-257± 23	104±22	0.0179	0.083
Roper	-389±58	109± 25	0.0174	-0.172
3rd peak	-555 ±83	86±20	0.0038	0.185
$^{112}Sn(Cu, X)^{112}Sb$				
Δ	-247±22	110± 25	0.041	-0.0176
Roper	-407±43	95± 22	0.0164	-0.194
3rd peak	-538±81	35 ±10	0.0047	-0.094
$^{112}Sn(Pb, X)^{112}Sb$				
Δ	-239± 21	119± 27	5.05984	1.18e-01
Roper	-389±37	76± 18	0.0094	-0.526
3rd peak	-559 ±84	54±12	-0.031	-0.523641
$^{112}Sn(H, X)^{112}In$				
Δ	-298±27	109±25	0.52	0.0002
Roper	-507±47	46± 18	0.0032	0.0003
$^{112}Sn(C, X)^{112}In$				
Δ	-240±22	128± 28	6.97311e-01	1.05032e-01
Roper	-404±36	123± 28	0.202733	-7.36053e-02
3rd peak	-567±65	74± 17	0.066	2.36420e-02
$^{112}Sn(Cu, X)^{112}In$				
Δ	256± 23	136± 31	0.0130	-0.0175
Roper	-427 ±40	145± 33	0.00440	-0.1939
3rd peak	-580±54	105 ± 16	0.0011	-0.094
$^{112}Sn(Pb, X)^{112}In$				
Δ	-250±23	95±22	0.0152	0.1406
Roper	-386±35	103± 24	0.00729349	-0.0249
3rd peak	-535±56	63±16	0.0031	-0.193

Table 4.5: Breit-Wigner Fit parameters of the charge exchange reactions products

Role of the reaction energy

The excitation of baryon resonances in isobar charge-exchange reactions can also be proved by looking at their dependence with the kinetic energy of the reaction. According to the dependence of the nucleon-nucleon cross section with energy shown in Fig. 4.20 the threshold for the excitation of baryon resonance should be slightly below 400 MeV.

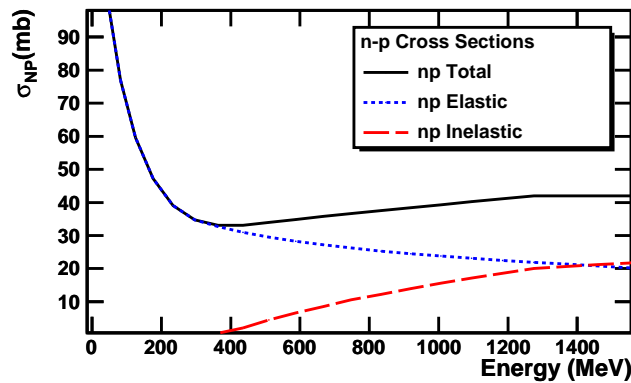


Figure 4.20: Total Cross section (solid line) as a function of the energy in the n - p scattering. The elastic (dotted line) and inelastic (dashed line) are nucleon-nucleon cross sections according to the Cugnon parameterization [117].

In heavy-ion collisions this threshold is even smaller. Figure 4.20 the first baryon resonance we should observe is the Δ resonance. Further increases in the reaction kinetic energy should allow the excitation of heavier resonances such as the $N(1440)$ or even heavier resonances. In Fig. 4.21 we depict the missing energy spectra of ^{112}Sb projectile residues produced in isobar charge-exchange reactions induced by ^{112}Sn projectiles impinging a carbon target at 400 (dashed line), 700 (solid line) and 1000 A MeV (dotted line). These measurements were obtained placing the reaction target at the entrance of the FRS and using the two sections of the spectrometer to identify and analyze the reaction products.

The evolution of the missing energy spectra with the energy of the reaction shown in Fig. 4.21 clearly follows the evolution of the elastic and inelastic nucleon-nucleon cross sections shown in Fig. 4.20. The elastic cross section decreases with energy while the inelastic one increases. Moreover, one can also observe how the inelastic peak at 400 and 700 A MeV presents a single contribution corresponding to the Δ resonance, while at 1000 A MeV two additional resonances are clearly seen.

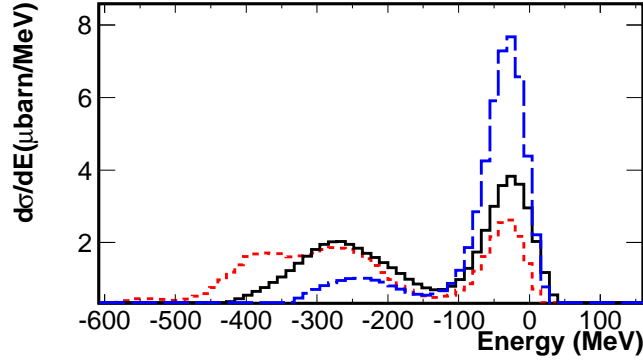


Figure 4.21: Energy dependence of the inelastic channel in the reaction $^{112}\text{Sn}(\text{C},\text{X})^{112}\text{Sb}$: The charge exchange reactions at 400 A MeV (blue line), 700 A MeV (black line) and the 1 A GeV (red line) in the beam particle frame.

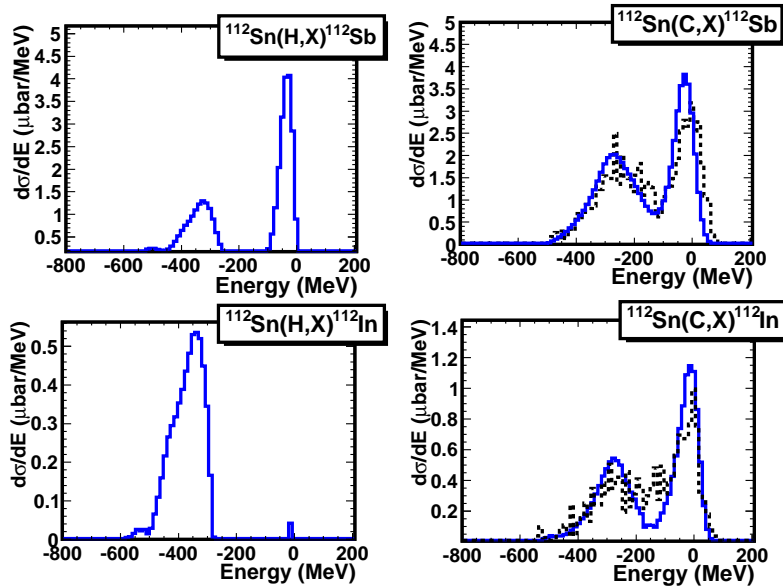


Figure 4.22: Energy Distributions of ^{112}Sb and ^{112}In at 700 A MeV (dotted line) their respective deconvolution (blue line). In the case of the proton target only the unfolded subtraction appears.

Figures 4.22 and 4.23 show the measured missing energy spectra for isobar charge-exchange reactions induced by ^{112}Sn projectiles on proton and carbon targets at 700 and 400 A MeV, respectively. These spectra follow the same pattern discussed for Fig. 4.21 .

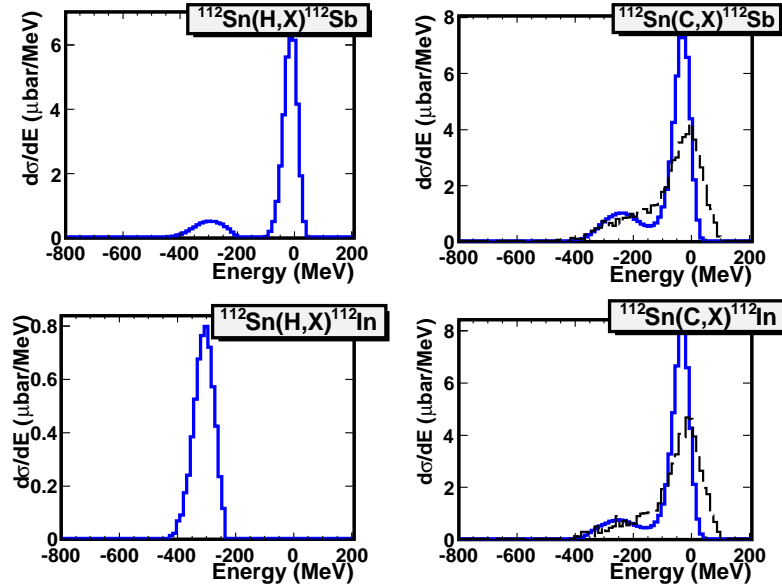


Figure 4.23: Energy Distributions of ^{112}Sb and ^{112}In at 400 A MeV (dashed line) and their respective deconvolutions (solid line). In the case of the proton target only the unfolded subtraction appears.

Role of the projectile neutron-excess

In order to evaluate the possible dependence of the Δ resonance formation with the projectile, we used the same target and change the projectile. In this way it is possible to check the possible isospin dependence with the projectile.

Figure 4.24 shows the energy distributions for different Sn projectiles and it is clear that each distributions present Δ and N(1440) resonance peaks contributions. In the case of ^{112}Sb , the relative Roper production is higher than others cases. Furthermore, the third peak present a shift in the mean value of energy.

Role of the target mass

The investigation of the Δ -resonance excitation in (p,n) and (3He,t) charge-exchange reactions has revealed how this process is affected by nuclear in-medium effects.

The main observation was a downward energy shift of the Δ -resonance peak position by around 70 MeV when using heavy targets ($A > 10$) as compared to the mean energy of the Δ resonance produced in free nu-

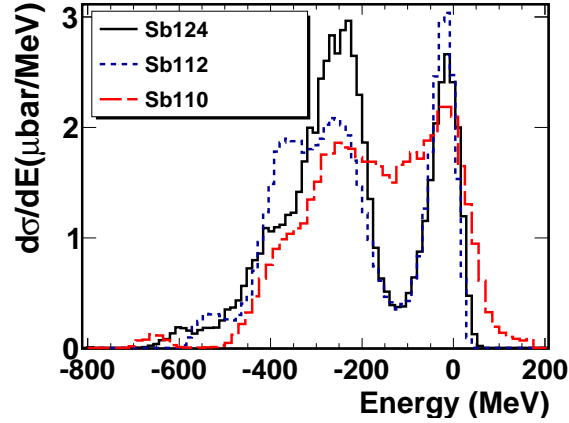


Figure 4.24: Dependence of the inelastic region with the projectile isospin for the different Sb residues produced in the np reaction of the $^{124,112,110}\text{Sn}$ beams that impinging on carbon target at 1 A GeV.

cleon–nucleon collisions.

Further experiments ([87] and references cited therein) investigating the Δ -resonance excitation in charge-exchange reactions using heavy ion collisions also have shown a clear dependence of the magnitude of the downward energy shift in the Δ resonance with the mass of the target nucleus.

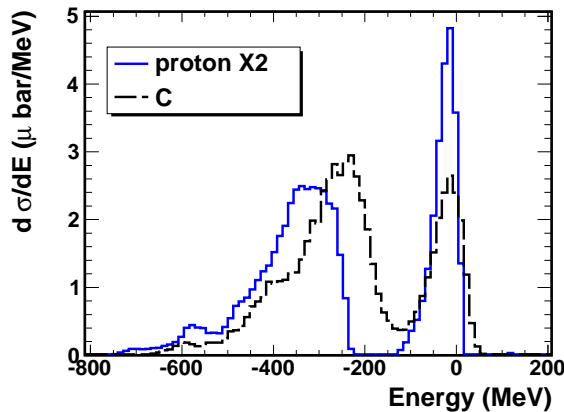


Figure 4.25: Missing energy spectra of the ^{124}Sb in the reaction of ^{124}Sn beam impinging on proton and carbon target at 1 A GeV. We can observe the energy shift of the Δ -resonant peak produced in the carbon target (dashed line) with respect to Δ -resonant production at proton target (solid line). The value of this shift is around ~ 70 MeV.

In the figure (see fig. 4.25) shows this effect observed in our experimental data.

In others experiments using different probes ([87]) such as leptonic and electromagnetic probes this shift was not observed with the probes, so this fact shows that the hadron probes are sensible to the isovector component of the nuclear force. For this reason, when we used the hadron projectile we could obtain an excellent tool to understand the nuclear force.

4.5.2 Model Calculations

Several models based on isobar-hole assumptions (see *e.g.*, Ref. [88] and references therein) have been used to interpret the charge-exchange reactions, as well as the production of the Δ and other nucleonic resonances. In this section, we briefly present the preliminary calculations made by Vidaña [118] used in this thesis to analyze the experimental results obtained. According to this model, quasi-elastic and inelastic processes are described in terms of an exchange of a virtual pion between the interacting nucleons. The effect of short range correlations is also included in the case of the quasi-elastic processes by means of the well-known Landau-Migdal parameter g' . In the inelastic case, the excitation of the Δ and N^* resonances is considered both in the target and in the projectile. The basic ingredients to compute the cross sections of these elementary reactions are the $NN\pi$, $N\Delta\pi$, and $NN^*\pi$ vertices.

The cross section for a charge-exchange (${}^Z A, {}^{Z\pm 1} A$) reaction is calculated using the following equation:

$$\frac{d^2\sigma}{dE_{ejectile}d\Omega_{ejectile}} = \frac{d^2\sigma}{dE_3d\Omega_3} \times |F(q)|^2 \times S_P \times P_{abs} . \quad (4.2)$$

As the product of the elementary process cross section, a projectile-ejectile transition form factor ($|F(q)|^2$) that takes into account the spatial extension of the nucleons in the projectile/ejectile nucleus, and a survival probability S_P that accounts for the fact that when nuclei interpenetrate many, less energetic, collisions will take place between the nucleons and degrade the initial available energy. In the case of the inelastic processes should be included also a factor P_{abs} that takes into account the reduction of the cross section if the pion produced in the reaction is absorbed.

We end this section by showing in Figs. 4.26 and 4.27 the contributions of the Δ excitations to the total double differential cross section of the elementary charge-exchange (p,n) and (n,p) reactions. Similar calculation was made for the Roper resonance but is not presented in this discussion. The relative

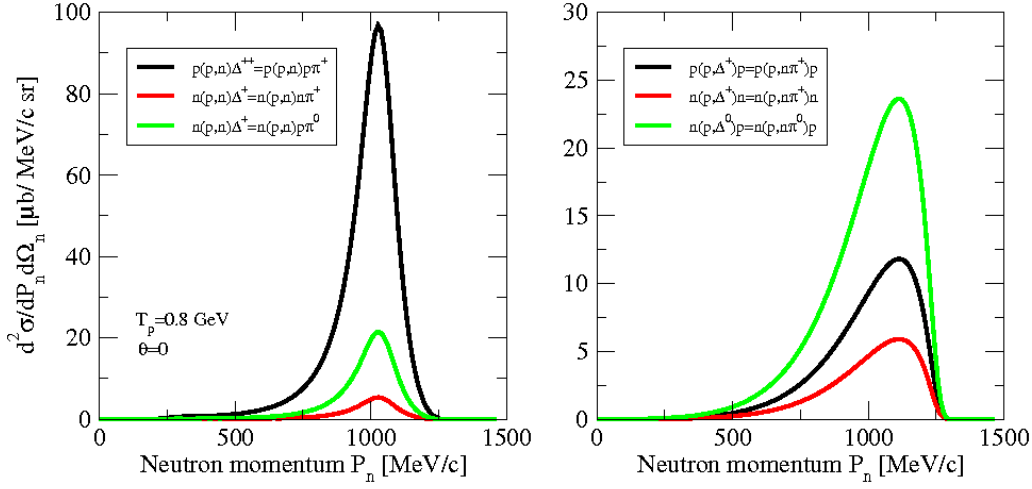


Figure 4.26: Contributions of the Δ excitation to the total double differential cross section of the elementary charge-exchange (p,n) reaction [118]. Left panel shows the Δ^- excitation in the target and right panel Δ^- excitation in the projectile.

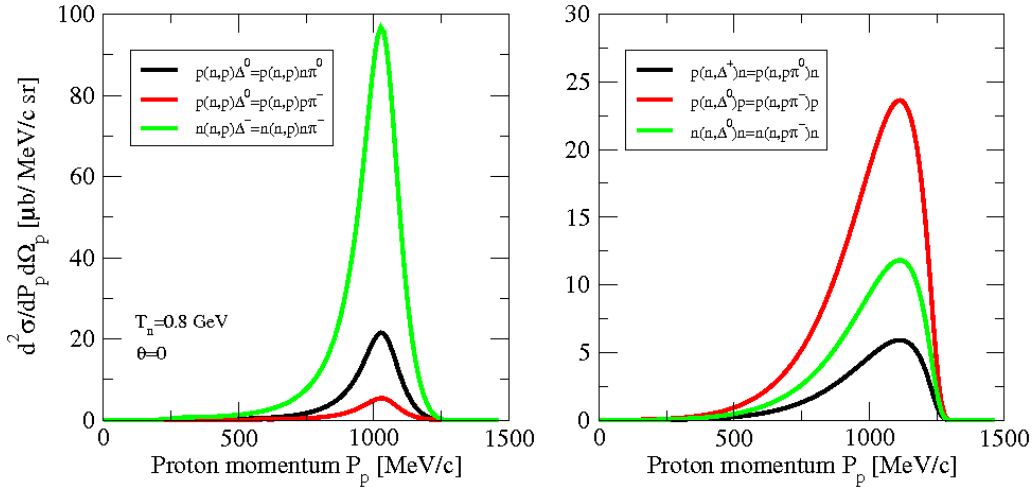


Figure 4.27: Contributions of the Δ excitation to the total double differential cross section of the elementary charge-exchange (n,p) reaction [118]. Left panel shows the Δ^- excitation in the target and right panel Δ^- excitation in the projectile.

weight of the different processes can be easily understood by looking at their isospin factors of the given in Tables 4.3 and 4.2. It is also interesting to note that the shape and the position of the resonance is more symmetric and close to the value of its rest mass when it is excited by means of the process shown

in Fig. 4.4 (left panel), where the resonance excitation occur in the target. On the other hand when the excitation mechanism is that of Fig. 4.4(right panel) the shape of the resonance becomes asymmetric and its position is shifted. This is a kinematical effect related with the different values of the resonance invariant mass calculated in the target or in the projectile.

4.5.3 In-medium production of the Δ resonance

The figure 4.28 shows the behavior of the Δ -resonance production cross section as a function of the target mass (A). It is clear that the Δ -resonance cross section is increased when the number of nucleons, and the difference between the np and pn channel is that each channel is sensitive to the number of nucleons in the nuclear periphery.

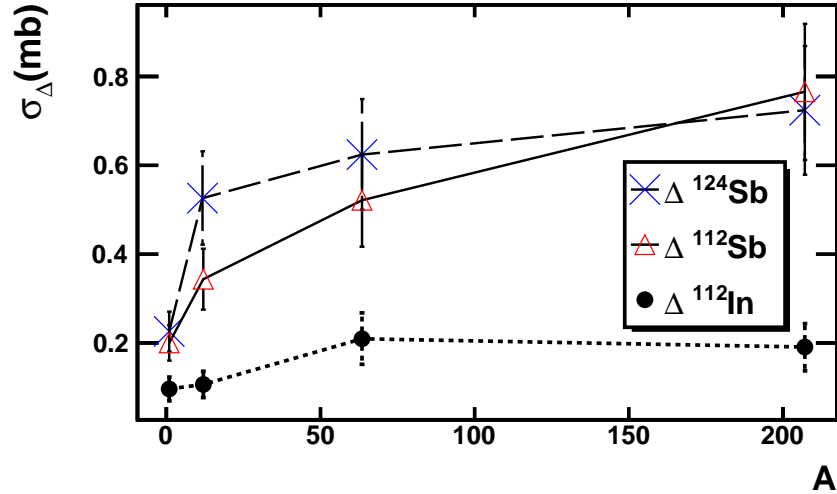


Figure 4.28: Δ -resonance cross section as a function of the target mass (A). The cross section in the case of the n-p channel is bigger than p-n channel.

The inelastic peak appears above Δ energy production threshold at 300 MeV. At this energies the production probability of inelastic peak grows with the energy beam. The quantification of each energy peak of the reaction is important in order to understand the in medium properties and isospin dependence of the isobaric charge-exchange reaction with heavy ions.

The inclusive measures in our experiment do not allow to distinguish each resonance multiplet and their respective origin (target or projectile) by a direct method.

The ^{112}In production on proton target is a special case that allow us to compare the individual resonance excitations and their origin in the projectile or target with the experimental data obtained in this work. Figure 4.29 shows the theoretical calculations of pn channel on proton [118] in the inelastic channel. The Δ resonance production is shown in the distributions with

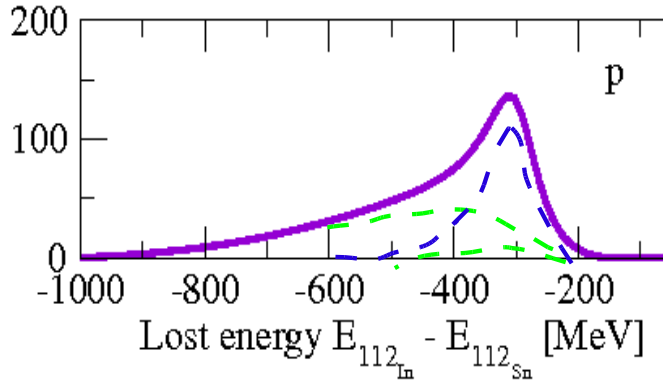


Figure 4.29: Theoretical calculations of pn channel on proton [118] in the inelastic regime. Resonance excitations in the target (blue line) and excitations in the projectile (green line) are presented.

meanvalue close to 300 MeV and the Roper resonance is presented as a broad distribution. This calculation shows us the production of Δ^{++} in the target and Δ^+ in the projectile. Moreover, the same calculation indicates that the Δ^{++} production is higher than the Δ^+ . Table 4.6 shows a comparison with the previous experimental results .

Mass(MeV)	Width(MeV)	Reaction	Data Reference
1231 to 1233 (≈ 1232)	116 to 120 (≈ 118)	N-N (free case)	PDG. [86]
1229 ± 27	109 ± 25	$^{112}\text{Sn}(H, X)^{112}\text{In}$	This Work

Table 4.6: Experimental values for the mass and width values for the Δ resonance.

4.5.4 In-medium production of the Roper resonance

Figure 4.30 shows the Δ resonant peak as a prominent component in the missing energy, but it is possible to observe a additional component: the Roper ($N(1440)$) resonant. This component is independent of the binning variation that proves that is not a mathematical artefact.

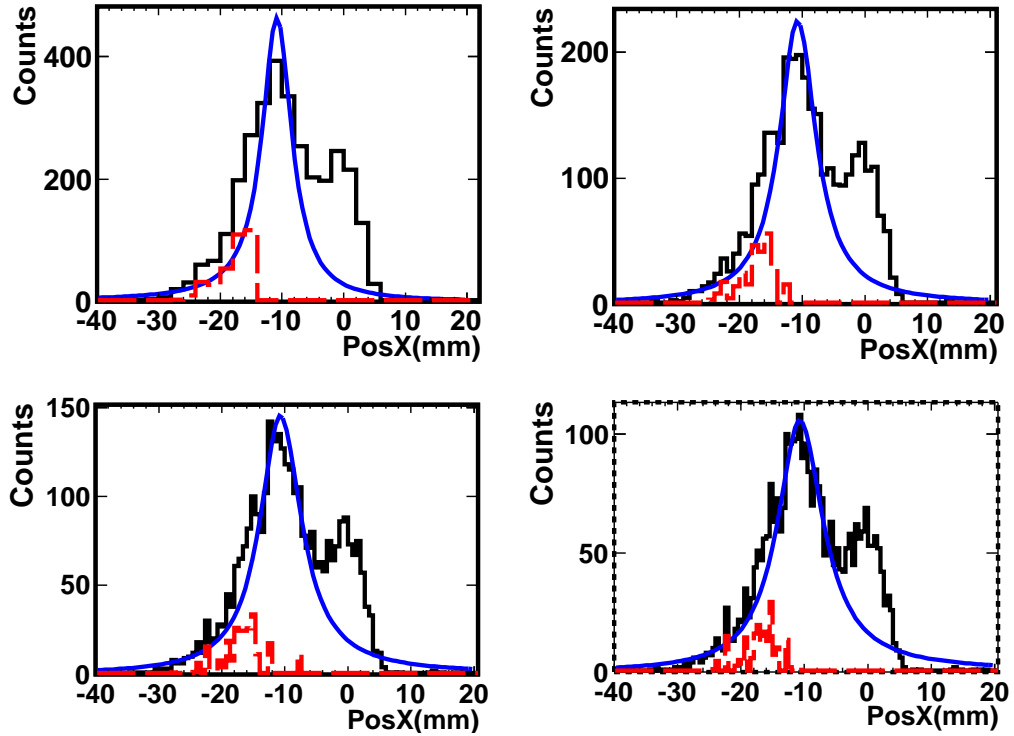


Figure 4.30: Binning dependence of the charge exchange reaction energy distribution in the position picture. In the inelastic peak it is possible disentangle the Roper resonance (dashed line) subtracted the Δ resonance (solid line) contribution. The result is independent from the binning (N_b). In this case the left top plot is the energy spectra at $N_b=100$, the right-top plot $N_b=200$ and the following plots are $N_b=300$ and $N_b=400$ respectively.

Using the results in the figures 4.30 and 4.31 it is possible to assure that the other resonances are sensible at target mass and consequently the nucleon content is described in the nucleus. A theoretical description of this behavior require a detailed study of the fundamental interaction in order to understand the meson interaction and the probability of excitation of each resonant.

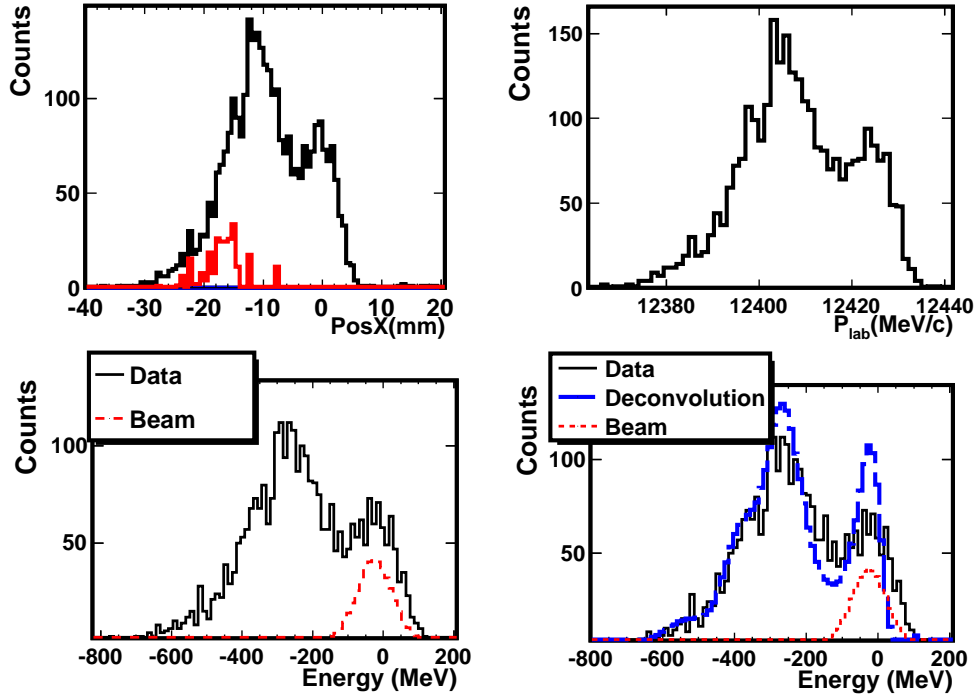


Figure 4.31: Spectrum of ^{112}Sb using different quantities pictures in the reaction $^{112}\text{Sn}(\text{Cu}, X)^{112}\text{Sb}$ at 1 A GeV. Left top: elastic and quasi-elastic peaks and the the Roper ($N(1440)$) resonance in position (red line). Right-top figure: ^{112}Sb spectrum in momentum representation. Left-bottom: beam and energy distribution in the beam particle frame. The right-low plot shows the unfolding procedure (dashed line) in the beam particle frame.

Figure 4.32 represents the deconvolution of ^{110}Sb and ^{120}In spectra, in each case it is possible to separate the inelastic and quasi-elastic peaks but it is more complicated to disentangle the roper resonant.

Figure 4.33 shows the $N(1440)$ resonance cross section as a function of the target mass (A). The cross section in the case of the n-p channel is bigger than p-n channel. Each component grows with the nucleon content in the periphery.

Using the calculations [118] represented in the Fig. 4.29 it is possible to observe the Roper resonance only the P_{11}^+ is produced in the projectile. The experimental results show that this component have a relative small production in comparison with the obtained with the calculation.

The systematic study of the Roper resonant is complemented by the heavy ion data. The experimental data using heavy ions is scare and for this rea-

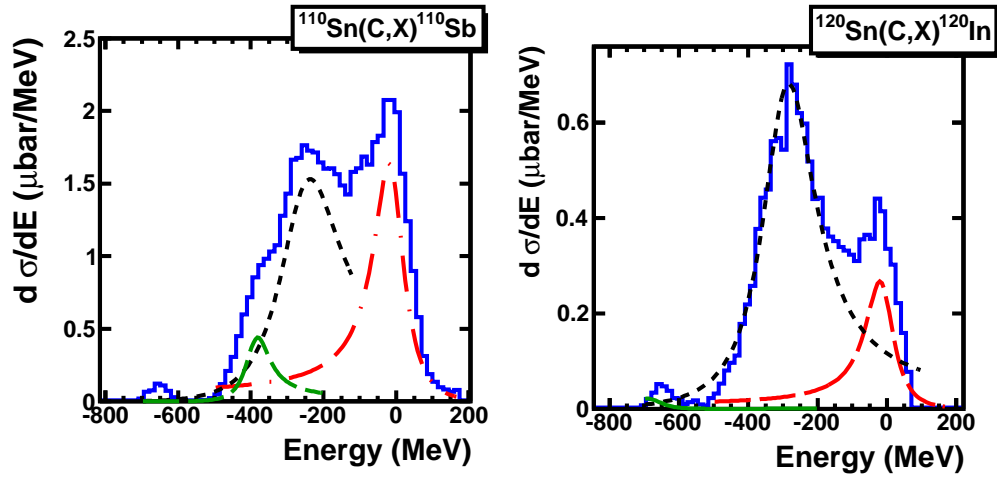


Figure 4.32: Fit of unfolded distributions in the two step configuration. Left panel corresponds to the ^{110}Sb production ; in this case it is possible to identify the quasi-elastic channel (dash-dotted line), the Δ resonant (dotted line) and the Roper resonant (dashed line) and the total unfolding (solid line). Right panel: In the case of ^{120}In the Roper does not appear. The ^{120}Sb and ^{122}Sb productions do not appear because of the low statistics.

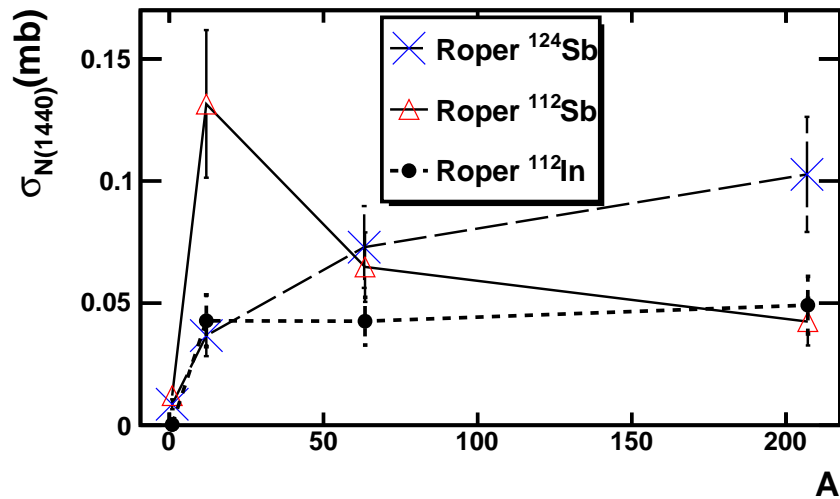


Figure 4.33: Roper resonance cross section as a function of the target mass (A). Each component grows with the nucleon content in the periphery.

son the data that provides this work shed light on the Roper resonant production in heavy ions. Figure 4.34 shows the $N(1440)$ contribution in the

inelastic reaction $\alpha(p, X)\alpha'$ at 4.2 GeV. The results obtained by $\alpha + p$ reaction [119] and its comparison with the C+C collisions at 4.2 GeV/c [120] per nucleon demonstrate that width of N(1440) decrease in presence of the nuclear medium.

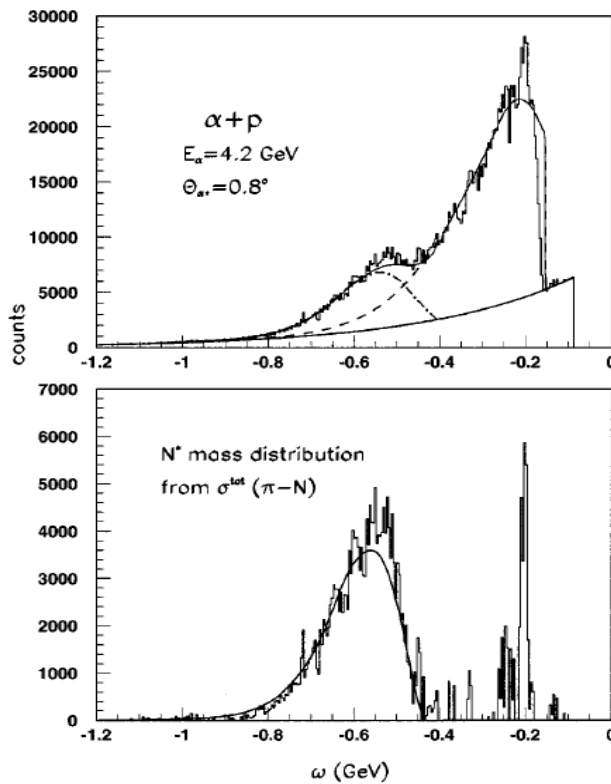


Figure 4.34: Missing energy spectra of the reaction $\alpha(p, X)\alpha'$ at 4.2 GeV. The Roper P_{11} appears in inelastic reaction [119].

Third resonance

The third peak that appear in the unfolding results might correspond to possibilities: $N(1530)$ or $\Delta(1600)$. Other possibility is a double Δ -resonance production. Unfortunately, we cannot distinguish between these two situations resonances with only the average value of the energy.

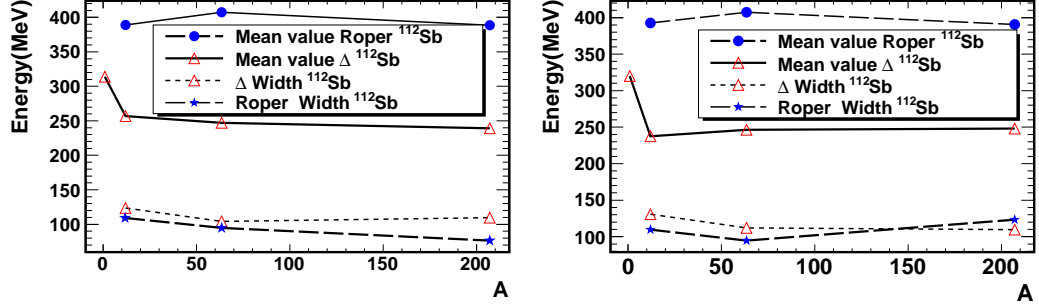


Figure 4.35: Energy dependence of a mean value of the $\Delta(1232)$, $N(1440)$ and $\Delta(1600)$ resonances as a function of target mass. The left panel represents the results of $^{124}\text{Sb}(\text{target}, X)^{124}\text{Sb}$ and right panel $^{112}\text{Sb}(\text{target}, X)^{112}\text{Sb}$. The width of the Δ -resonance is represented with a black solid line. The mean value and width of the Δ -resonance is almost constant and it is clear the energy shift with respect to proton target.

Figure 4.35 shows the energy dependence of a mean value of the $\Delta(1232)$, $N(1440)$ resonances as a function of target mass. In this plot it is clear that the energy shifts with respect to proton target, and we can observe that it is almost constant in the carbon, copper and lead targets.

The theoretical calculations give as an idea of the elementary processes involved in this work. It is clear that our results are inclusive measures, for this reason it is complicate to determine the contribution of each resonance excitation depending of their production in target or projectile. In order to disentangle these contributions it is necessary to use a more sophisticated experimental set up that included the produced pion detection. Since the energy and charge identification of the produced pion it is possible determine the origin of each resonance.

CHAPTER 5

Knockout reactions induced by Sn isotopes

In the present chapter we explore another peripheral reaction channel in relativistic heavy-ion collisions which is the projectile knockout process. These are reactions where projectile nuclei lose few nucleons while the residual nucleus remains bound.

Knockout reactions have been largely used to investigate the structure of nuclei far from stability and their spatial distributions. The main observables used to investigate these reactions are the cross sections of this reaction channel and the longitudinal momentum distributions of the reaction residues.

In this work we take advantage of the several tin isotopes used as projectiles to systematically investigate these reactions. On top of the scan in isotopic composition of the projectiles we will investigate proton and neutron knockout and in some cases we will measure the knockout of several nucleons. With these measurements we will address several interesting issues such as the energy dissipated in peripheral fragmentation reactions, the role of nuclear excitations in nucleon knockout and the evolution of this process with the neutron excess.

5.1 Measurements

In order to cover a large range in projectile neutron excess we combined stable tin projectiles (^{112}Sn and ^{124}Sn) with secondary beams of non stable tin isotopes (^{120}Sn and ^{110}Sn) produced by fragmenting the stable ones.

Therefore, the measurement of the cross-sections of neutron and proton

Target Place	Beam	Target(mg/cm^2)	Fragment
S0	^{112}Sn	C(978)	$^{110}Ag, ^{109}Ag, ^{108}Ag$ $^{107}Pd, ^{106}Pd$ $^{106}Rh, ^{105}Rh, ^{104}Rh$
	^{112}Sn	C(100)	^{110}Cd $^{108}Ag, ^{105}Pd$ $^{103}Rh, ^{102}Rh$
S2	^{110}Sn	C(910)	$^{109}In, ^{109}Sn$
	^{112}Sn		$^{111}In, ^{111}Sn, ^{108}Cd$
	^{120}Sn	C(1400)	$^{119}In, ^{119}Sn, ^{118}Cd$
	^{124}Sn		$^{123}In, ^{123}Sn$

Table 5.1: List of fragments obtained by the reaction of Sn beams at C targets at 1 A GeV. It is important that the complete data set is a mix of the one and two steps set-up

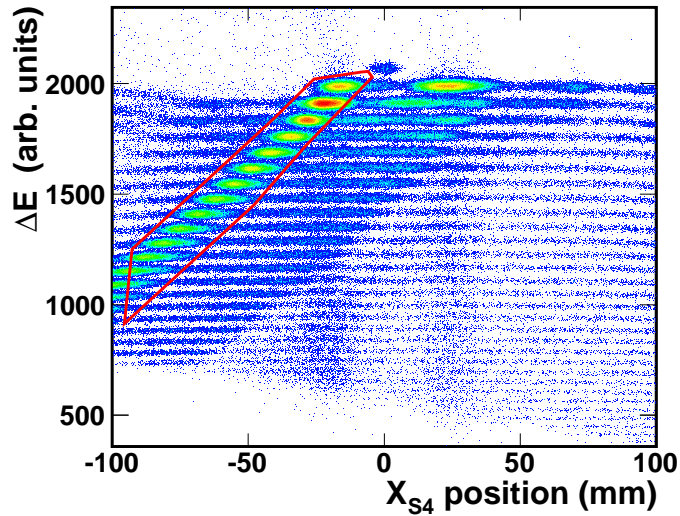


Figure 5.1: Energy loss as a function of position in the final focal plane of the spectrometer. The solid line represent a charge states cut. This is an identification plot at the final focal plane in a setting centered in ^{112}In .

removal channels was performed by using the one and two step experimental setup explained in section 2.3.

The identification procedure follows the method presented in section 3.1.

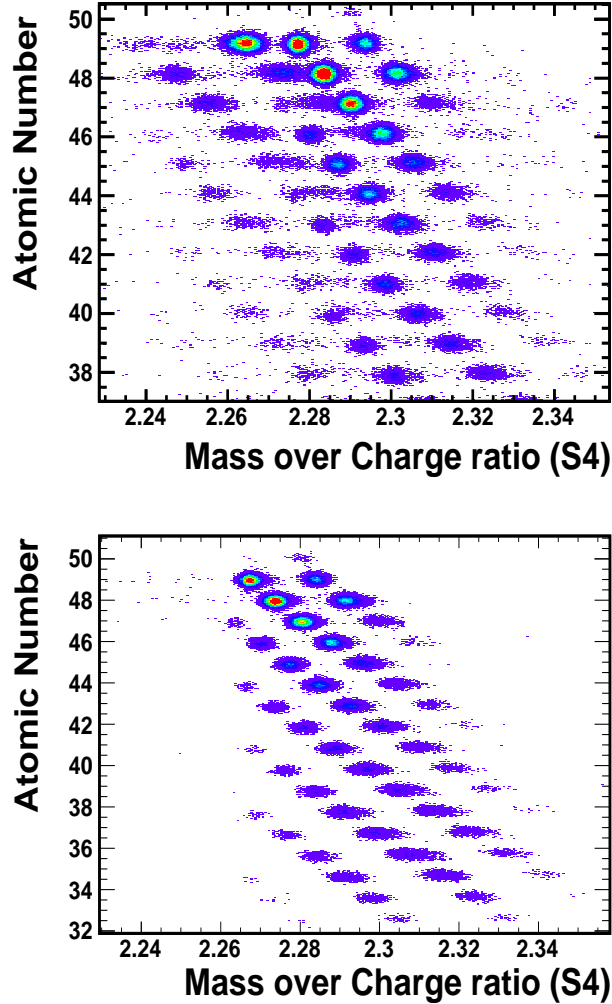


Figure 5.2: Identification plot at the final focal plane in a setting centered in ^{112}In without charge states correction (top panel) and the identification plot corrected by charge states (bottom panel).

Table 5.1 summarizes the measurements done in this work.

As can be seen in table 5.1 we could measure for all the tin isotopes used as projectiles in this work the one proton and neutron knockout channels. Moreover, for the ^{110}Sn beam we measured the two-proton removal channel and for ^{112}Sn projectiles up to the four-proton removal channel.

Other important effects that affect the identification is the charge state contribution in each MUSIC. In order to clean the identification plot it is necessary to remove the charge states using a suitable selection of fully stripped

reaction residues according to their energy loss and position at the final image plane as shown in the figure 5.1. This correction is only applied to the reactions induced at S0 . The result of this correction is shown in figure 5.2.

In the case of reactions induced by secondary beams using the two step set-up, it is necessary to identify the beam at the middle focal plane in order to select the correspondent event reactions at S4.

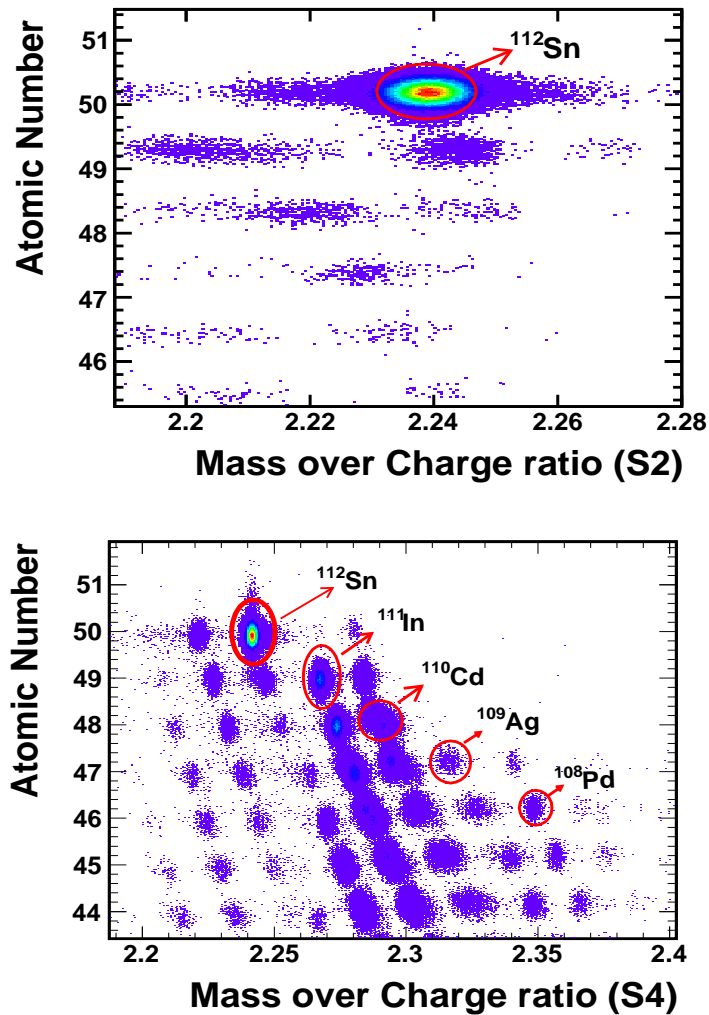


Figure 5.3: Identification plot of a setting centered in ^{112}Sn at the middle focal plane (S2) (left panel). The right panel shows the identification matrix at the final focal plane (S4) produced in the reaction of ^{112}Sn impinging on the carbon target (right panel). The figure is a overlapping of several magnetic settings of the FRS.

Fragment	f_T	f_d	f_s	Fragment	f_T	f_d	f_s
^{123}Sn	1.00	1.30	1.17	^{123}In	1.68	1.20	1.17
^{119}Sn	1.00	1.30	1.17	^{119}In	1.68	1.20	1.17
^{118}Cd	1.00	1.30	1.17	^{107}Pd	1.68	1.20	1.17
^{111}In	1.3	1.22	1.09	^{106}Pd	1.83	1.25	1.17
^{111}Cd	1.45	1.20	1.17	^{105}Pd	1.27	1.30	1.17
^{110}Cd	2.70	1.25	1.17	^{104}Pd	20.0	1.30	1.17
^{109}Cd	4.35	1.25	1.17	^{107}Rh	1.63	1.25	1.17
^{110}Ag	1.85	1.03	1.17	^{106}Rh	4.34	1.25	1.17
^{109}Ag	1.00	1.03	1.17	^{105}Rh	1.00	1.20	1.17
^{108}Ag	2.58	1.20	1.17	^{104}Rh	66.6	1.20	1.17
^{107}Ag	1.43	1.25	1.17	^{103}Rh	1.39	1.20	1.17
^{108}Pd	1.00	1.25	1.17	^{102}Rh	4.81	1.30	1.17

Table 5.2: Correction factors for each nucleus. The transmission correction factor f_T estimation for each fragment for each set-up that appear in the table 5.1 calculated using the LISE code. f_d , f_s are the dead time and secondary reactions correction factors respectively. The charge states correction factor $f_{ch.st}$ is around $\sim 1\%$ and this value do not appear in the table

Table 5.2 shows the corrections factors applied to each isotope production in order to correct the production and use this value with the objective of determine the cross section. The same technique described in the chapter 3 is used in order to determined the cross section of the fragmentation residues. Corrections factors such as the dead time f_d , secondary reactions f_s and $f_{ch.st}$ charge states were explained in the section 3.5. Nevertheless, it is important to note that the selection of a specific non-centered fragment require an additional correction factor depending on its *transmission*. As it was explained in the section 2.2, the FRS has a limited momentum acceptance for this reason the complete momentum distributions, and consequently the number of total number of residues were not fully transmitted in a determined magnetic setting. Table 5.2 shows the transmission value estimation for the different settings that appear in the table 5.1. By comparison with the MOCADI and LISE codes we can associate to the transmission calculation an accuracy around 15%

5.2 Nucleon removal cross sections

The identification of the projectile knockout residues, it is a first for step for the determination of the cross section of these processes. In the case of

reactions investigated using direct beams, we have two focal planes where it is possible to identify the final residues. However, when using unstable beams, the two step configuration must be used where the secondary the secondary beam is separated using the first stage of the FRS, impinging on a reaction target placed at the middle focal plane. Figure 5.3 shows an example of selection of ^{112}Sn beam at the intermediate focal plane (top panel) that produce by fragmentation a the identification plot in in the final focal plane S4 (bottom panel). The list of the Sn beam projectiles at S2 is presented in the table 5.3.

The procedure presented in the section 3.5 allows us determinate the cross section of each produced fragment. A important input in order to determine the cross section it is the number of projectiles N_b . In the case of the direct reactions this quantity is determined using the SEETRAM detector, on other hand, the number of unstable projectiles is obtained from the corresponding identification plot at S2 by the direct selection in the interest fragment. The yield of final fragments identified at S4 are corrected by the factors that appear in the table 5.2.

Beam	Product	Cross section (mb)
^{110}Sn	^{109}In	69.20 ± 15.87
	^{109}Sn	141.33 ± 29.68
	^{108}Cd	5.38 ± 1.24
^{112}Sn	^{111}In	56.6 ± 13.02
	^{111}Sn	142.02 ± 29.82
	^{110}Cd	3.01 ± 0.69
	^{109}Ag	0.61 ± 0.15
	^{108}Pd	0.03 ± 0.01
^{120}Sn	^{119}In	24.47 ± 5.14
	^{119}Sn	125.57 ± 26.37
	^{118}Cd	1.03 ± 0.24
^{124}Sn	^{123}In	25.62 ± 5.89
	^{123}Sn	138.03 ± 28.99

Table 5.3: Measured cross sections produced by nucleon removal in the reaction of different Sn beams on carbon target.

In table 5.3 we summarized the cross sections results. In this table it is possible to observe the results obtained for the proton an neutron removal induced by the Sn projectiles at 1 A GeV.

5.2.1 Model calculations

As was mentioned in the chapter 1, peripheral heavy-ion collisions at relativistic energies can be described using theoretically microscopic [7, 10, 11] or macroscopic model descriptions as the abrasion-ablation model [8, 16, 17, 18].

In general these reactions are understood as a two-step process. First the fast interaction between projectile and target nuclei leading to prefragments that have lost some nucleons and gained excitation energy and angular momentum. In the second stage the prefragments de-excite by emitting additional nucleons, clusters of nucleons or eventually fissioning.

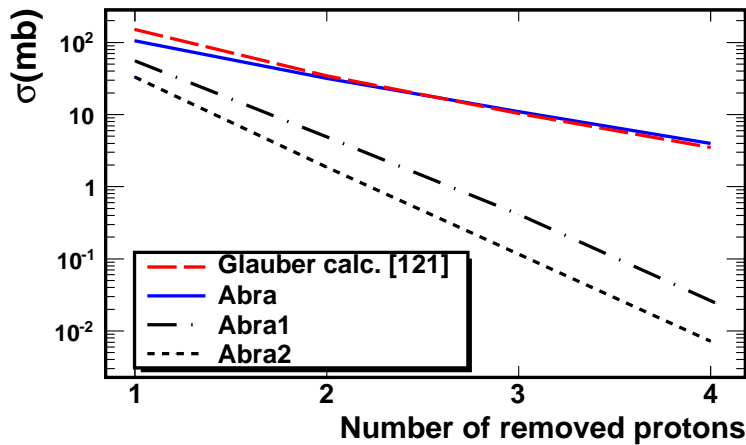


Figure 5.4: Different codes calculations of the proton removal induced by ^{112}Sn projectiles on carbon target.

The first stage of the reaction can be described using a macroscopic abrasion model or a microscopic Glauber model [2]. The abrasion model determines the number of abraded nucleons from the superposition volume between projectile and target nuclei defined by the impact parameter.

In the Glauber model the probability to abrade or knock-out n nucleons in a heavy-ion collision is given by the probability of occurrence of n nucleon-nucleon collisions as was explained in the chapter 1.

In Fig. 5.4, the solid and dashed lines represent the probably for removing up to five protons from a ^{112}Sn nucleus as calculated using the abrasion model in the code ABRABLA [20] and a Glauber calculation performed by C. Bertulani [121], respectively. As can be seen in the figure, both calculations yield very similar results validating thus all the calculations we will perform with the abrasion model.

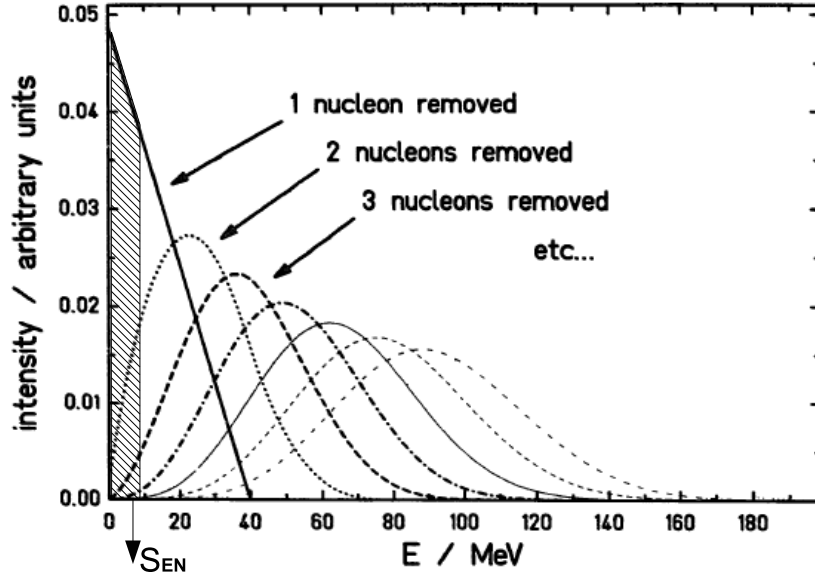


Figure 5.5: Excitation-energy distributions as calculated with the diabatic model [18] for different prefragments, after the abrasion of 7 nucleons from the projectile nucleus. Neutron evaporation threshold (S_{EN}) is shown.

The excitation energy gained by the prefragments can be obtained from the energies respect to the Fermi level of the holes created by the knockout nucleons in the Fermi distribution of nucleons in the nucleus. This model yields a linear distribution of excitation energy in the knockout of a single nucleon as shown in Fig. 5.5. This distribution corresponds to the fact that most of the nuclear levels in the Fermi distribution are close to the Fermi level and less and less when we move down in the nuclear potential well. The excitation energy distribution for collisions removing more than one nucleon can be obtained by convolution of the single knockout energy distribution with itself as many times as nucleons are removed. These excitation energy distributions are also shown in Fig. 5.5. As can be seen in the figure, the larger the number of abraded nucleons the higher the excitation energy gained by the pre fragments. The figure also reveals large fluctuations in the energy distributions corresponding to the removal of several nucleons. The de-excitation of these hot pre-fragments during the second stage of the reaction can be described using a statistical model.

The basis of this model is the compound hypothesis [122] which explain the statistical equilibrium in terms of the excitation energy and angular mo-

mentum of the prefragment.

In this assumption, the de-excitation process is described by the emission of nucleons, clusters of nucleons, gammas or eventually fissioning according to the statistical weight of each decay channel.

The probability of a certain de-excitation channel it is proportional to the decays widths are obtained using the Weisskopf-Ewing [123, 124, 125] statistical model In order to evaluate the absolute decays values it is necessary to apply the principle of detailed balance between two systems a and b in statistical equilibrium. This systems are described by the level densities ρ_a and ρ_b and time reversal invariance is imposed. Then the relation between these states is given by the following equation:

$$\rho_a \Gamma_{ab} = \rho_b \Gamma_{ba} \quad (5.1)$$

here Γ_{ab} is the decay width for the transition $a \rightarrow b$, Γ_{ba} is its time reversed process.

In this model the decay width for this process can be calculated using the following equation:

$$\Gamma(U_i, J_i; U_f, J_f, s_\nu) = \frac{(2s_\nu + 1)k_f^2}{2\pi^2} \sigma_f(U_i, J_i) \frac{(2J_f + 1)\rho(U_i, J_i)}{(2J_i + 1)\rho(U_i, J_i)} \quad (5.2)$$

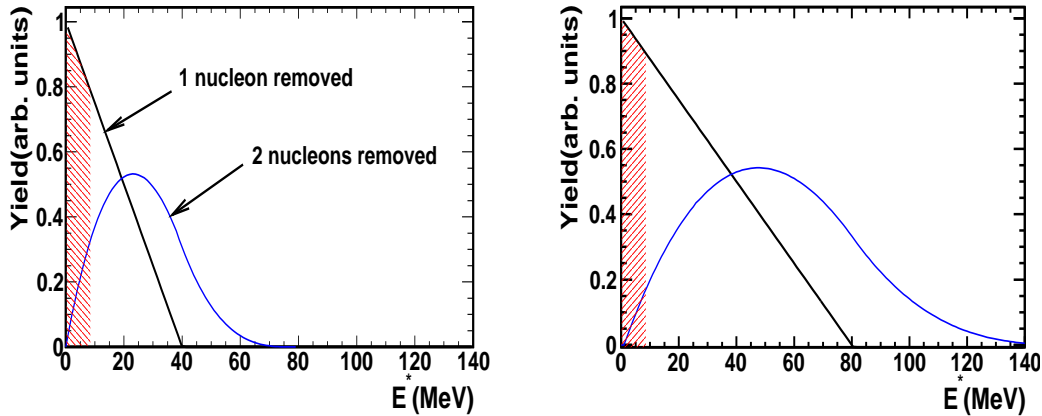


Figure 5.6: Comparison between the excitation energy distribution in the single particle level calculation. The left panel represent calculations made with an average excitation value about 13.5 MeV per abraded nucleon, the right panel represent calculation made with a double average excitation. The shaded area represent the nucleon evaporation threshold

where U_i and J_i are the initial nucleus excitation and total angular momentum, respectively. This initial stage reaches the final state (U_f, J_f) emitting a nucleon or cluster of nucleons with a kinetic energy ϵ_ν , spin s_ν , separation energy S_ν and B_ν the Coulomb barrier. The excitation energy after a single de-excitation step will be obtained by energy conservation as follows:

$$U_i = U_f + \epsilon_\nu + S_\nu + B_\nu$$

An alternative statistical model to describe the fission decay channel was proposed by the Bohr and Wheeler [126].

The benchmark of these model calculations with measurements of the production cross sections of residual nuclei produced in knockout reactions and in general in fragmentation reactions, shows a clear overestimation of the measurements. In Ref. [127] it was shown that the model better describe the data by increasing the single-particle excitation energy of the model by a factor 2 as illustrated in Fig. 5.6. In this figure the dashed area represents the fraction of nucleon removal reactions below the nucleon evaporation threshold describing the knockout processes.

In order to interpret the data measured in this work we will benchmark them with three types of calculations. Calculations where the cross sections of the final residues is obtained from the abrasion model with no nuclear excitation that we will call Abra0. Calculations where the excitation energy is obtained from the single-particle holes produced by the abraded nucleons, Abra1, and the same model but increasing the excitation energy by a factor 2, Abra2. In Fig. 5.4 we show estimations of the cross sections of proton-removal reactions for a ^{112}Sn projectile with the three calculations we have described.

5.2.2 Results and discussion

In this section present a comparative analysis of the cross section presented in the section 5.1 with the model calculations.

In these figures we also include proton and neutron knockout cross sections in reactions induced by ^{104}Sn and ^{112}Sn projectiles at 150 A MeV measured by Audirac and collaborators [128]. The good agreement for the cross sections obtained for the knockout of ^{112}Sn in both experiments indicates that the difference in kinetic energy does not affect significantly this reaction channel.

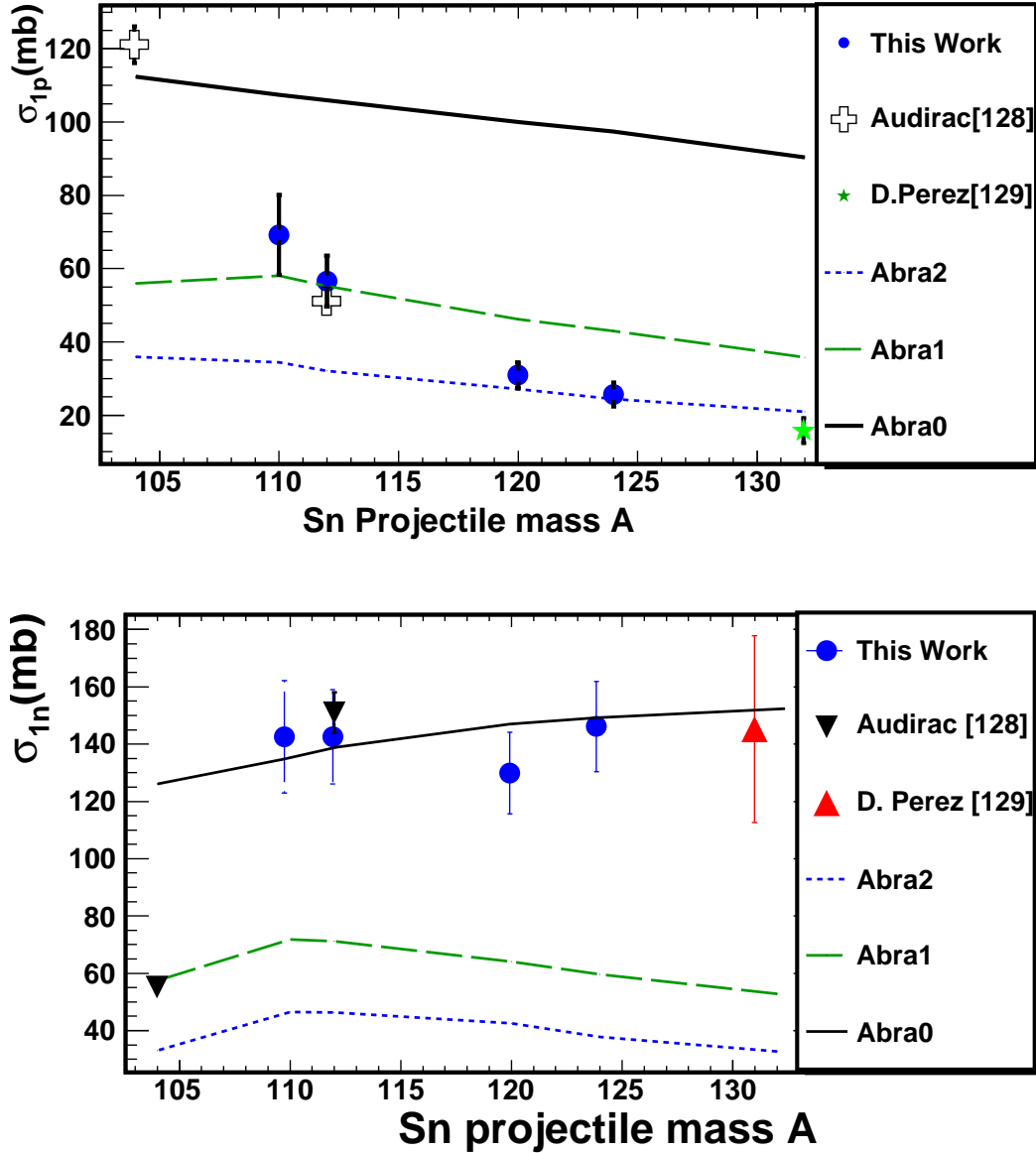


Figure 5.7: Top panel: One-Proton removal channel cross section as a function of Sn projectile mass. The general behavior of the experimental cross sections do not fit with the different Abra calculations. The Abra2 (dotted line), Abra1 (dashed line) are the Abra code using $2x, 1x$ factors in the energy excitation. Abra0 (solid line) correspond to geometrical model without include energy excitation. Bottom panel: Comparison between Abra calculations (solid line) and the experimental cross section measures of the one neutron removal channel in the reaction of ^{112}Sn on carbon target.

Figure 5.7 (top panel) shows the cross section of the one proton removal channel as a function of the mass number of the Sn projectile impinging on a carbon target. It is clear that in this reaction the cross section decreases with the projectile mass number A increases. Moreover, the different types of calculations performed with the code ABRABLA do not reproduce the evolution of the experimental one-proton removal channel.

A more detailed analysis indicates that results obtained with ^{132}Sn [129], ^{120}Sn and ^{112}Sn projectiles present a good agreement with the ABRABLA code with the enhanced value of the excitation energy (x2). On the other hand, calculations with the standard single-particle excitation energy reproduces the measured cross section for ^{112}Sn proton removal channels. However in the case of ^{104}Sn projectiles, the experimental cross sections are only described by calculations with the abrasion model without considering nuclear excitations.

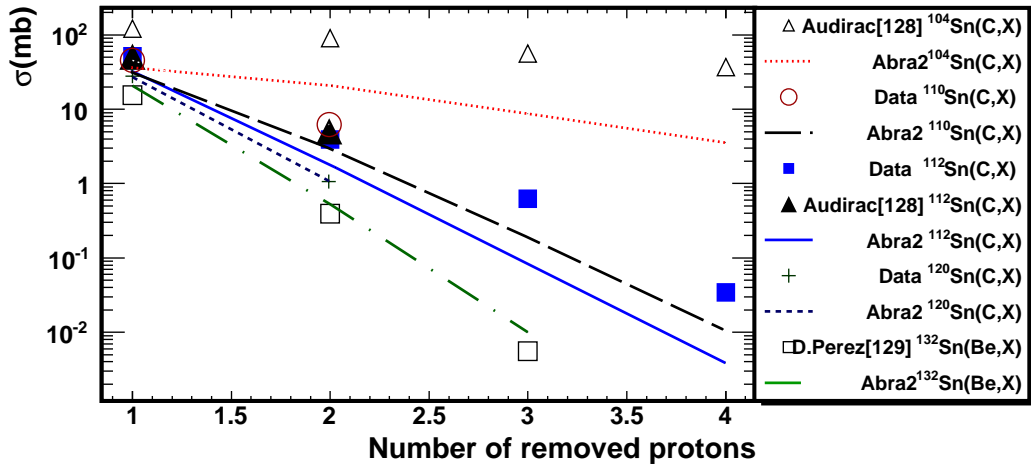


Figure 5.8: Cross sections of the proton removal channels produced by the fragmentation of Sn beams into carbon target. The experimental data are compared with the calculations of the Abrabla code with 2x modification in the energy excitation.

In the bottom panel from Fig. 5.7 we compare neutron knockout cross sections with similar model calculations as the ones shown in the upper panel. In this case we observe the opposite behavior as obtained in the proton knockout channels. The neutron knockout from neutron-rich projectiles can be described with abrasion model calculations without nuclear excitations. When decreasing the neutron excess of the projectiles we need to consider

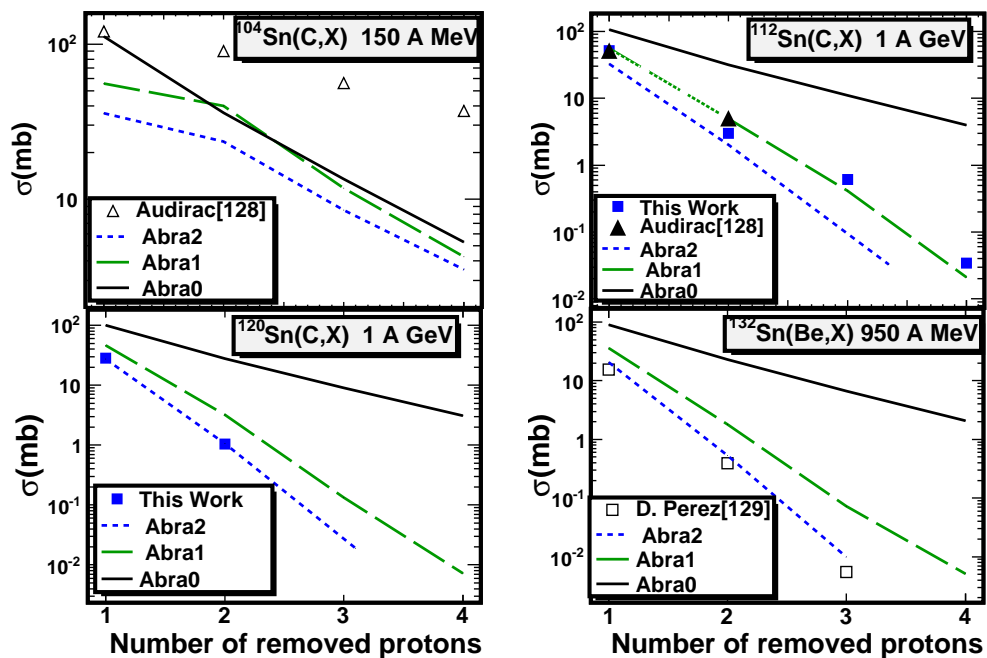


Figure 5.9: Measured cross sections in the reaction of Sn beams in different proton removal channels. The experimental data are compared with the prediction of ABRABLA code for different versions of excitation energy. The solid line correspond with the abrasion model without energy excitation (geometrical model). The dashed and dotted lines correspond to ABRABLA with $2x$ and $1x$ energy excitation respectively.

nuclear excitations and for the most neutron-deficient case, ^{104}Sn we even need to double the excitation energy estimated with the single-particle model.

This benchmark of measured and calculated proton and neutron knockout cross sections with projectiles covering a large range in excitation energy clearly indicates that nuclear excitations play an important role in knockout processes. More particularly we observe that nuclear excitations increases with the binding energy.

The role of nuclear excitations can also be investigated by looking at the multiple nucleon knockout cross sections as shown in Figs. 5.8 and 5.9. In these figures we compare multiple proton-removal cross sections measured with tin projectiles with different isospin with the model calculations previously described. Again the removal of protons from neutron-deficient nuclei, ^{1104}Sn , can be described without considering nuclear excitations. However for nuclei where protons are deeply bound we need to consider nuclear excitations.

Finally, in Fig. 5.10 we depict the production cross sections of the most neutron-rich reaction residues produced in collisions induced by ^{112}Sn projectiles impinging a beryllium target at 1000 A MeV. In this figure we also benchmark measured data and model calculations reaching similar conclusions as previously discussed. The most deeply bound nucleons induce more excitation energy than the loosely bound.

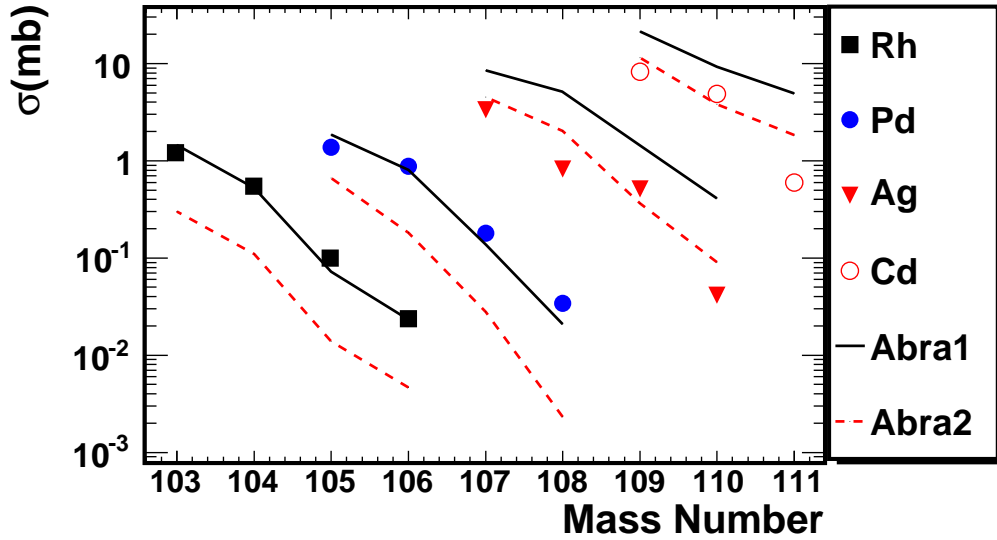


Figure 5.10: Isotopic distributions of the production cross section of residual nuclei measured in the fragmentation of ^{112}Sn on carbon target at 1 A GeV. The lines correspond to different Abra calculations using excitation energy.

5.3 Missing energy spectra

Finally we investigated the missing-energy spectra of the residual nuclei produced in knockout processes. The idea behind was to check the role of subnuclear excitations in this reaction channel.

In figure 5.11 we compare the missing energy spectra of ^{119}In residual nuclei produced in the one-proton knockout of ^{120}Sn projectiles impinging a beryllium target. In the figure we also include for comparison the same spectrum obtained with the beam nuclei. The beam spectrum represents the energy broadening induced by the experimental setup.

As can be seen in the figure, the one-proton knockout spectrum is rather broad because of the Fermi momentum of the knockout proton. However we

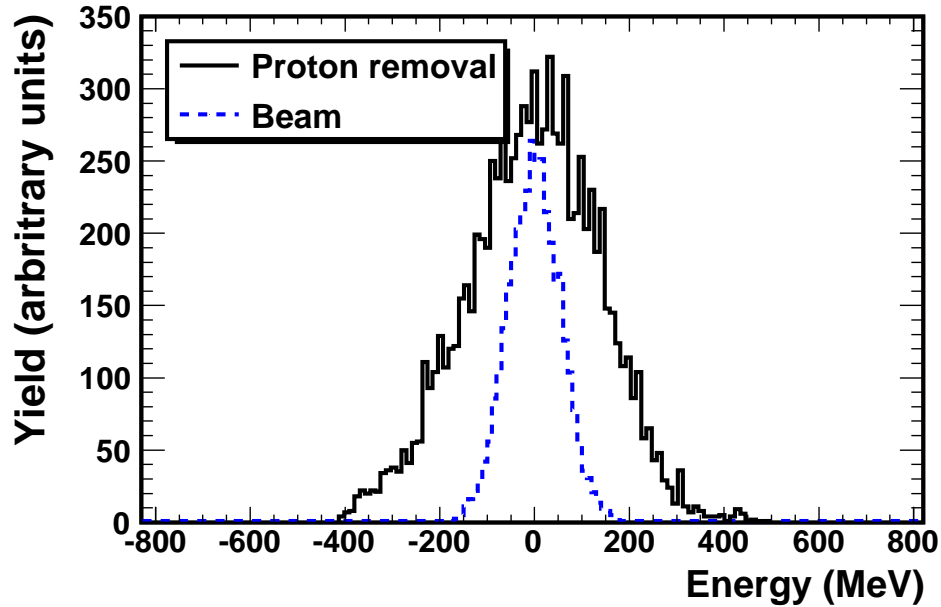


Figure 5.11: Missing energy distributions of ^{119}In (solid line) produced in the reaction of the ^{120}Sn (dotted line) at 1 A GeV impinging on carbon target.

do not observe any sizable contribution at large values of the energy missed in the reaction as it was the case for the isobar charge-exchange reactions investigated in chapter 4. We can therefore conclude that contrary to nuclear excitations, subnuclear excitations do not seem to play any relevant role in the knockout reaction channels.

Conclusions

In this doctoral work we have investigated nuclear and sub nuclear excitations by means of peripheral heavy-ion reactions at relativistic energies. In particular we have used isobaric charge-exchange and knockout reactions. The experimental technique is based on the inverse kinematics approach to induce these reactions. This technique allows the unambiguous identification of the projectile residues and the accurate determination of its longitudinal momentum by using a zero-degree high-resolving power magnetic spectrometer. Using this technique we proposed to use as observables for our investigations the production cross sections and the missing-energy spectra of the projectile residues issued in the reaction channels we propose for these investigations.

The experiment was performed in the GSI facilities in Darmstadt (Germany). The residues obtained in each reaction were analyzed using a magnetic spectrometer FRS (FRagment separator). The high resolution of the spectrometer combined with a detection system allowed us to unambiguously identify the projectile residues residues. This identification is the cornerstone for the determination of our physical observables : the cross section and the energy recoil spectrum of each fragment. In this experiment ^{112}Sn and ^{124}Sn beams induced reactions in different targets such as carbon, copper, lead and hydrogen at 1 A GeV energy. Moreover, a systematic study of the energy dependence of the charge exchange reaction was made using the ^{112}Sn beam accelerated to 1000, 700 and 400 A MeV. Using fragmentation reactions it was possible to produce ^{110}Sn , ^{120}Sn and ^{120}Sn secondary beams from the stables beams at 1 A GeV. This secondary beams induced reactions in a carbon target placed at the middle focal plane of the FRS.

In the case of the charge exchange reactions a complete systematic study

was performed. The dispersion of the FRS and the targets thickness were optimized in order to improve the resolution of the energy recoil distribution. The accuracy of these spectra was further improved unfolding from the measured spectra the response function of the experimental setup. This response function was determined from measurements with the primary beam. This unfolding was improved using a regularization method [106]. The missing energy spectra of the projectile residues produced in charge exchange reaction spectra show clearly the two components: at small and large values of the energy lost in the reaction by the projectile residues. We associate these two components to the quasi elastic and inelastic charge-exchange processes induced by nuclear and sub nucleon spin-isospin excitations.

The detailed analysis of the missing energy spectra and cross sections measured for the isobaric charge-exchange reactions investigated in this work allowed us to reach the following conclusions:

- The measured missing-energy spectra for the two isobar charge-exchange channels, (p,n) and (n,p), are in qualitative good agreement with previous measurements performed at SATURNE in France [89].
- The unfolding and regularization methods developed within this work made it possible to distinguish up to three substructures in the so called inelastic charge-exchange peak in the missing-energy spectra. The dependence of the intensity of these substructures with the beam energy and comparisons with other measurements allowed us to identify the two main substructures as the excitation of the Delta and Roper resonances.
- Taking advantage of model calculations performed by I. Vidaña, we could also identify the contributions of several members of the Delta and Roper isobar multiplets to the substructures in the missing-energy spectra we assigned to these nucleon resonances. Moreover, we also identified contributions from charge-exchange processes in the projectile and target nuclei. Therefore, the detailed investigation of the in-medium baryon resonances using isobar charge-exchange reactions will require exclusive measurements by means of pion detection in coincidence. These measurements would allow to identify excitations in the projectile or target nuclei but also the nature of the isobar multiplet member producing the excitation.
- The systematic analysis of reactions induced by unstable beams show us the limitation of the unfolding method. The thicker targets used

in these measurements and the lower statistics clearly affect the final resolution.

- The systematic study using different targets and its respective comparison with the proton target showed a clear shift of the inelastic peak toward the quasielastic region. This observation confirm previous results obtained in Saturne . The explanation of this effect could be interpreted in terms of in-medium effects [88, 87, 89] or kinematical effects as suggest the theoretical calculation of [118].
- A clear energy dependence of the intensity of the inelastic peak according to the evolution of the inelastic nucleon-nucleon cross section was observed in the reactions induced by the ^{112}Sn beam on carbon and proton targets.
- The evolution of the measured cross sections for the two isobar charge-exchange channels, (p,n) and (n,p), according to the neutron excess of the tin projectiles and in the different targets shows a clear dependence of this observable with the relative presence of neutrons and protons at the periphery of the colliding nuclei. However, in order to obtain the density of protons and neutrons at the nuclear periphery one would need model calculations not yet available.

In this work we have also performed a systematic investigation of projectile knockout reactions according to the neutron excess of the projectile tin nuclei. We obtain the following conclusions from these measurements:

- The single-proton knockout cross sections decreases by increasing the neutron excess of the projectiles. The behavior of the single-neutron knockout follows the opposite trend.
- The comparison of the measurements with abrasion-ablation calculations using the code ABRABLA indicates that the knockout of loosely bound nucleons (neutrons from neutron-rich nuclei and protons from neutron-deficient nuclei) does not induce any relevant excitation in the residual nuclei. However, the knockout of deeply bound nuclei induces significant excitations of the remnants .
- The same conclusions are valid for the multiple nucleon knockout.

APPENDIX A

List of layers in the experiment

Place	Layer	Material	Thickness(mg/cm^2)
S0	SIS window	Ti	4.5
	SEETRAM	Ti	13.5
Target	PE		95
	C		103,197
	Cu		373
	Pb		954
S2	Scintillator	C	370.44
	Scintillator	H	34.54
	TPC1 wind.	C	2.59
	TPC1 wind.	O	0.78
	TPC1	Ar	18.29
	MUSIC1	Ar	107
S2 Targets	Scintillator	C	475.45
	Scintillator	H	44.02
	C		978,1400
	TPC2 wind.	C	2.59
	TPC2 wind.	O	0.78
	TPC2	Ar	18.29
	Air gap	N	60.55
	TPC3 wind.	C	2.59
	TPC3 wind.	O	0.78
	TPC3	Ar	18.29
S4			
	TPC4 wind.	C	2.59
	TPC4 wind.	O	0.78
	TPC4	Ar	18.29
	MUSIC2	Ar	107
	TPC5 wind.	C	2.59
	TPC5 wind.	O	0.78
	TPC5	Ar	18.29

Table A.1: List of layers of matters used in the FRS beam line

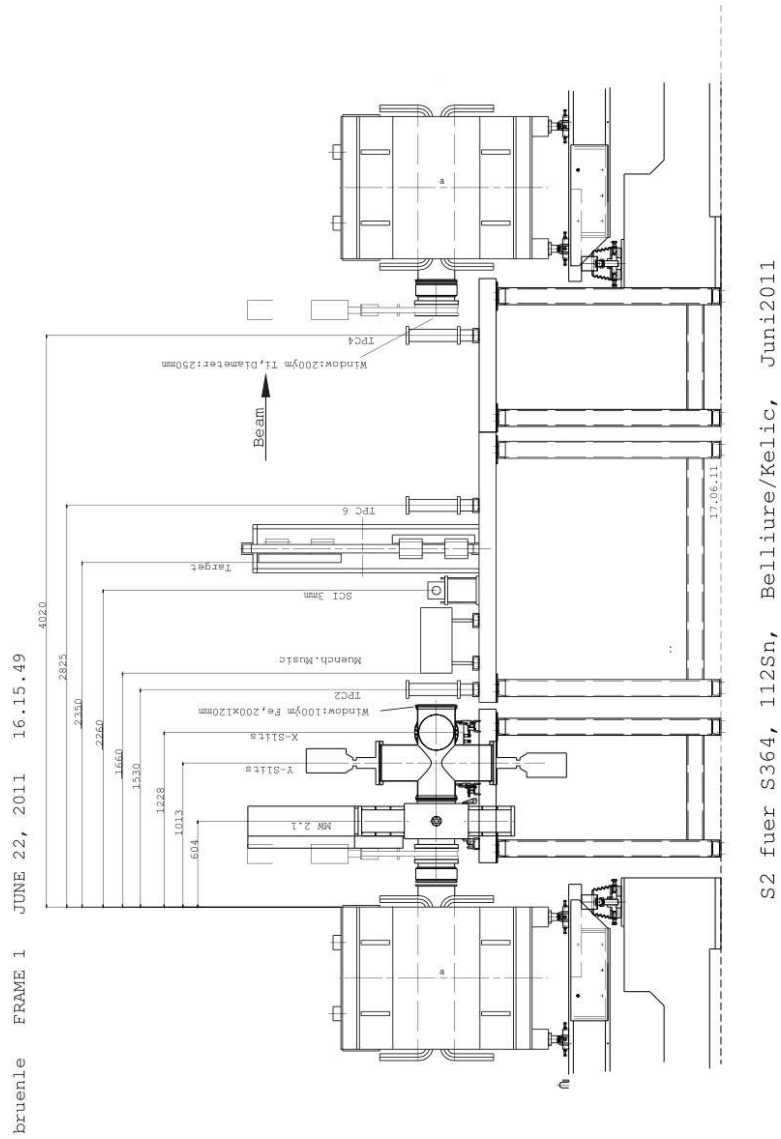


Figure A.1: Schematic view of experimental set up at S2

For more technical details see [99, 130, 131]

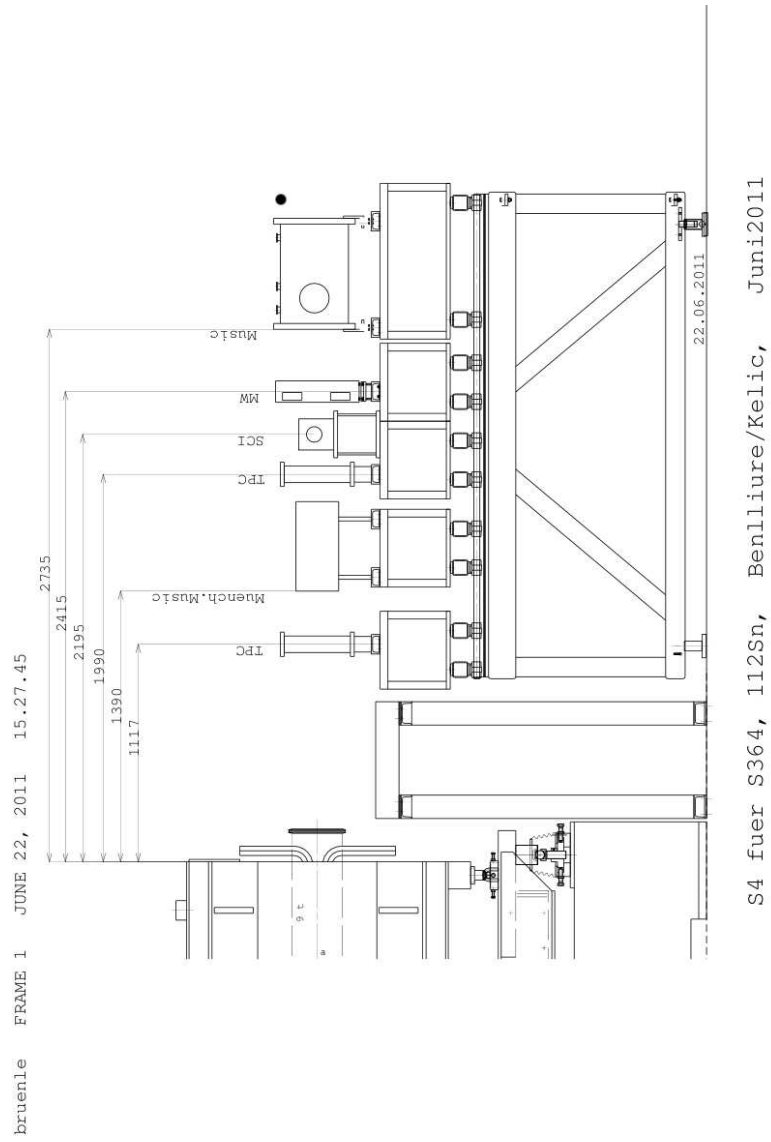


Figure A.2: Schematic view of experimental set up at S4

APPENDIX B

Deconvolution Method applied to the Energy Distributions

The magnetic spectrometer FRagment Separator at GSI has been used to investigate the in-medium Δ -resonance excitation in peripheral heavy-ion reactions. The resolving power of this spectrometer makes it possible to disentangle the longitudinal-momentum loss induced by the excitation of the Δ resonance in the projectile residues produced in isobaric charge-exchange collisions. However, beam emittance, electromagnetic interactions of projectile and residual nuclei in the target, and the accuracy of the tracking detectors limit the final resolution. The characterization of the Δ resonance requires then to unfold the measured longitudinal-momentum distribution from the response of the spectrometer. In this work, we use an unfolding procedure based on the Richardson-Lucy method with a regularization technique to optimize the stability of the solution against statistical fluctuations. In present appendix we included a publication wherein this unfolding method and its regularization method is explained in detail.



Unfolding the response of a zero-degree magnetic spectrometer from measurements of the Δ resonance

J. Vargas, J. Benlliure*, M. Caamaño

Universidade de Santiago de Compostela, 15782 Santiago de Compostela, Spain

ARTICLE INFO

Article history:

Received 2 June 2012

Received in revised form

12 December 2012

Accepted 14 December 2012

Available online 26 December 2012

Keywords:

Unfolding

Regularization

Magnetic spectrometer

Delta resonance

ABSTRACT

The magnetic spectrometer FRagment Separator at GSI has been used to investigate the in-medium Δ -resonance excitation in peripheral heavy-ion reactions. The resolving power of this spectrometer makes it possible to disentangle the longitudinal-momentum loss induced by the excitation of the Δ resonance in the projectile residues produced in isobaric charge-exchange collisions. However, beam emittance, electromagnetic interactions of projectile and residual nuclei in the target, and the accuracy of the tracking detectors limit the final resolution. The characterization of the Δ resonance requires then to unfold the measured longitudinal-momentum distribution from the response of the spectrometer. In this work, we use an unfolding procedure based on the Richardson–Lucy method with a regularization technique to optimize the stability of the solution against statistical fluctuations. The method is validated using measurements of isobaric charge-changing collisions with a ^{136}Xe beam at 500 A MeV.

© 2012 Elsevier B.V. All rights reserved.

1. Introduction

The investigation of the Δ -resonance excitation in (p,n) and ($^3\text{He,t}$) charge-exchange reactions has revealed how this process is affected by nuclear in-medium effects. The main observation is a downward energy shift of the Δ -resonance peak position by around 70 MeV when using heavy targets ($A > 10$) as compared to the mean energy of the Δ resonance produced in free nucleon–nucleon collisions [1,2].

Further experiments investigating the Δ -resonance excitation in charge-exchange reactions using heavy ion collisions also have shown a clear dependence of the magnitude of the downward energy shift in the Δ resonance with the mass of the target nucleus [3]. In these experiments, performed at the Laboratoire National Saturne in France, the longitudinal-momentum of projectile residues produced in isobar charge-exchange reactions was measured with the spectrometer SPES IV [4] with a typical resolution $\Delta p/p = \pm 7 \times 10^{-4}$.

More recently, it was demonstrated that the magnetic spectrometer FRagment Separator (FRS) [5] at GSI (Darmstadt) can also be used for this purpose [6]. In this case, a ^{208}Pb beam at 1 A GeV was used to induce isobaric charge-exchange reactions in proton, deuterium, and titanium targets, leading to the production of ^{208}Bi . The recoiling nuclei were isotopically identified with the FRS. The corresponding longitudinal-momentum distributions showed two components that were associated to quasi-elastic and inelastic charge-exchange reaction channels. The quasi-elastic

channel peak corresponds to Gamow–Teller transitions. The inelastic channel in isobar charge-exchange reactions is understood to be due to the excitation of a Δ resonance in a nucleon–nucleon collision, where the subsequently emitted pion escapes from the nuclear medium. Because of the large pion absorption cross-section, these processes correspond most likely to extremely peripheral collisions. Under such conditions, one can expect that the properties of the excited Δ resonance could provide not only information on the in-medium modifications of the hadron masses, but also on the nucleon–nucleon cross-section at low densities. Moreover, at GSI one can produce beams of nuclei far from stability [7]. Measuring the properties of the excited Δ resonance in isobaric charge-exchange reactions induced via projectiles with a different neutron excess, one could expect to deduce information on the iso-vector component of the nuclear force.

These possibilities depend, however, on the accuracy obtained for the measurement of the Δ -resonance properties, in particular, its average mass and width. The measurements not only depend on the resolving power of the magnetic spectrometer but also on the beam emittance, the position resolution of the tracking detectors, and the electromagnetic interactions of projectile and residual nuclei in the target material and other layers of matter in the beam line. These effects can be corrected via deconvolution of the measured longitudinal-momentum distribution from the response function of the experimental device.

The main advantage of the use of deconvolution methods (rather than, for example parametric models) is the fact that no assumptions on the features of the physical distribution and the response function are needed, avoiding any bias on the final result. In our particular case, the shape of the response function is

* Corresponding author.

E-mail address: j.benlliure@usc.es (J. Benlliure).

measured, and the number of peaks in the momentum distributions and their characteristics are obtained as a result of the deconvolution method. In this work, we adapt a well-known deconvolution technique to unfold the response of a magnetic spectrometer from measured longitudinal-momentum distributions. This procedure is based on Richardson–Lucy’s technique [8,9] with an additional method to optimize the stability of the result against statistical fluctuations. In the first section of the paper, we discuss the intrinsic resolving power of a magnetic spectrometer and how it can be degraded by the experimental conditions. Then, we describe the unfolding procedure we use. In the final section, we validate the method using measurements of the longitudinal-momentum of residual nuclei produced in isobaric charge-exchange reactions induced by ^{136}Xe projectiles at 500 A MeV in a liquid hydrogen target, obtained with the FRS at GSI.

2. Measuring the longitudinal-momentum of recoiling projectile-like residues in relativistic heavy-ion collisions

The accurate determination of the longitudinal-momentum of nuclei traversing a zero-degree magnetic spectrometer, such as the FRS, depends on the measurement of the corresponding magnetic rigidities. The FRS is an achromatic spectrometer with two symmetric stages and a dispersive intermediate image plane. Under such conditions, the dispersion in magnetic rigidity ($B\rho$) of the trajectories around the central one can be obtained according to the following equation:

$$\frac{\Delta B\rho}{B\rho} = \frac{(x|x)_{24}\Delta x_4 - \Delta x_2}{(x|\delta p)_{24}} \quad (1)$$

where Δx_2 and Δx_4 represent the positions along the dispersive coordinate of the trajectories at the intermediate and final image planes with respect to the central one, $(x|\delta p)_{24}$ represents the dispersion, and $(x|x)_{24}$ the magnification between the intermediate and final image planes.

If one considers incident particles with the same magnetic rigidity, the same expression will provide us the accuracy in the magnetic rigidity determination according to the dispersion in the measurement of the positions of the trajectories at the intermediate and final image planes. The dispersion in the measurement of the positions can be due to the resolution of the tracking detectors, the initial emittance of the beam, or the energy, angular and reaction location straggling of the transmitted particles in the different layers of matter located along the spectrometer, in particular, the target and the detectors placed at the intermediate image plane.

Fig. 1 represents the estimated contributions to the final resolution in the measurement of the magnetic rigidity of ^{136}Cs , produced in the reaction $^{136}\text{Xe} + \text{Al}$ at 500 A MeV, due to the resolution of the tracking detectors, the beam emittance, and the electromagnetic interactions of the nuclei with an aluminium target as a function of its thickness. In these calculations, we have taken as reference the nominal values of the dispersion and magnification of the Fragment Separator ($(x|\delta p)_{24} = 6.8 \text{ cm}/\%$ and $(x|x)_{24} = 1.16$) and we assume that no matter is located at the intermediate image plane.

In this figure, the thin horizontal lines stand for the contribution to the resolution due to the beam energy dispersion $\Delta E/E = \pm 5 \times 10^{-4}$ (dotted line) and the tracking detector resolution considering $\Delta x_2 = \Delta x_4 = 2 \text{ mm}$ (dashed line). The thick lines evolving with the target thickness represent the contribution to the magnetic rigidity resolution due to the electromagnetic interactions of the incoming nuclei with the target material, the energy straggling (dashed-dotted line), the angular straggling (dotted line), and the reaction location straggling (dashed line). The thick solid line represents the final resolution considering all the above mentioned effects.

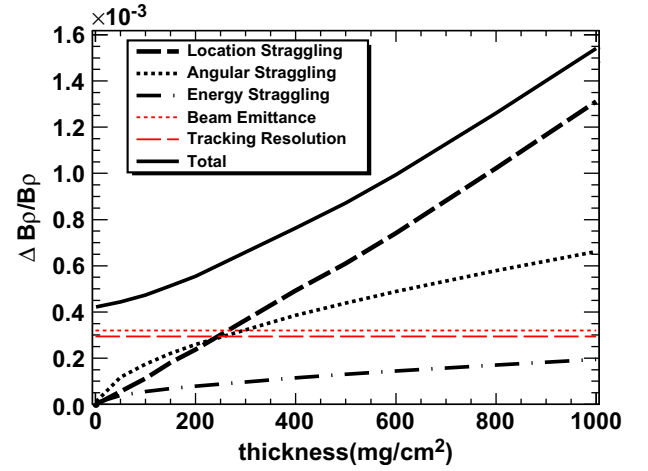


Fig. 1. Simulated contributions to the resolution in magnetic rigidity measurement of ^{136}Cs , produced in the reaction $^{136}\text{Xe} + \text{Al}$ at 500 A MeV, with a magnetic spectrometer as a function of the target thickness. The thin horizontal lines represent the energy spread of the beam (dotted line) and the effect due to the position resolution of the tracking detector (dashed line). The thick lines represent the effect due to the electromagnetic interactions of the projectile and residual nuclei with the target: energy straggling (dashed-dotted line), angular straggling (dotted line), the reaction location straggling (dashed line). The thick solid line represents the final resolution considering all the contributions.

line) and the reaction location straggling (dashed line). The solid line corresponds to the final resolution considering all the above mentioned effects.

As can be seen in the figure, the position resolution of the tracking detectors and the beam emittance limit the magnetic rigidity resolution for aluminium targets thinner than $250 \text{ mg}/\text{cm}^2$. For thicker targets, the resolution is limited by the electromagnetic interactions of the transmitted nuclei with the target material.

Unfortunately, the target thickness is very often defined by statistical considerations. In the particular case of measurements with secondary beams of nuclei far from stability, having low intensities, the feasibility of the measurements requires the use of thick targets. In those cases, the possibility of unfolding the contribution of those effects degrading the magnetic rigidity resolution could be an option for accurate measurements. Moreover, the measurement of the momentum dispersion of non-interacting beam nuclei provide an optimal definition of the experimental response function required by the unfolding procedure. Indeed, beam nuclei experience electromagnetic interactions in the target and the layers of matter placed along the spectrometer in a similar manner to the isobar charge-exchange residual nuclei.

3. Unfolding method and numerical calculations

From a mathematical point of view, the measured distribution in the spectrometer \mathbf{Y} can be described as the convolution of the true distribution of the observable of interest \mathbf{X} and the response function of the experimental setup \mathbf{H}

$$\mathbf{Y} = \mathbf{H} \otimes \mathbf{X} \quad (2)$$

In the case of a histogram representation, a discrete formulation is used

$$Y(i) = \sum_{j=1}^{n_{bins}} H(i-j) \cdot X(j) \quad (3)$$

where $X(j)$ and $H(j)$ are the representations of \mathbf{X} and \mathbf{H} as histograms with a n_{bins} number of bins, and $Y(i)$ is the measured

distribution \mathbf{Y} as a histogram with the same n_{bins} . This holds correct as long as the effect of the response function is a random perturbation of the collection of data within the true distribution [10]. The deconvolution, a special case of unfolding, is then the inverse operation of this process, and it can be used to obtain the true distribution.

Several methods have been developed to calculate the $X(j)$ vector from known $Y(i)$ and $H(j)$ distributions. Unfortunately, no method is free from drawbacks, and the selection of an algorithm depends on the particular conditions of the problem to solve. Some methods, such as the Fast Fourier Transform, produce fast results with a non-iterative procedure but with a poor management of background noise [11]. These spurious effects can be avoided with methods based on the maximum entropy principle [12] but with a fair increase of computing time and a strong dependence on the input parameters. The use of iterative techniques raises the concern about the convergence and/or stability of the solution with the successive iterations. As an example, the Van Cittert method [13] is found to yield oscillating solutions [14]. Other techniques such as Gold [15] or Richardson–Lucy [8,9] produce more stable solutions but they require regularization techniques for selecting the optimal output. A summary of recent unfolding techniques can be found in Ref. [16]. More specifically, different iterative unfolding techniques have been studied in Refs. [8,9,17]. In this work, the Richardson–Lucy deconvolution method is chosen over other techniques. The relatively short computing time it uses to yield a stable solution makes it suitable to repeat several tests with varying conditions in a reasonable time frame. However, the study presented here is not exclusive of this method and it may be applied to other techniques.

3.1. The Richardson–Lucy method and regularization

The Richardson–Lucy deconvolution algorithm is an iterative technique that converges to the maximum likelihood solution for Poisson statistics in the data. This deconvolution algorithm uses the measured distribution and the response function as input to calculate the true distribution. The mathematical formulation of the relationship between a measured value $X(i)$ and the measured distribution in the spectrometer $Y(i)$ is

$$X^{(m)}(i) = X^{(m-1)}(i) \sum_{j=1}^{n_{bins}} H(j-i) \frac{Y(j)}{\sum_{k=1}^{n_{bins}} H(j-k)X^{(m-1)}(k)} \quad (4)$$

where m is the iteration number, n_{bins} is the number of bins of vectors $X(i)$, $Y(j)$, and $H(i)$ is the response distribution; i , j , and k are bin indexes.

As with other deconvolution techniques, the output of this method is iteration-dependent. This issue must be addressed carefully, particularly in those cases where the width of the distribution of a given observable is of interest, as in the case of nucleon resonances. Tests performed with this method revealed that the width of peaks in the true distribution become narrower in successive iterations (see inset in Fig. 2).

In order to minimize the uncertainties associated with the oscillations or degradation of the solution in an iterative deconvolution, a method of regularization is necessary to define the optimal number of iterations. A comparative study of regularization methods and their application to different unfolding techniques can be found in Ref. [18]. As an example, D'Agostini uses a deconvolution algorithm similar to the Richardson–Lucy method, with a regularization technique based on comparison between consecutive iterations [17]. However, as it was mentioned before, such methods relying on the convergence of the solution may yield unreasonable solutions, particularly when determining the widths of the peaks, as it is our case. Techniques, such as the

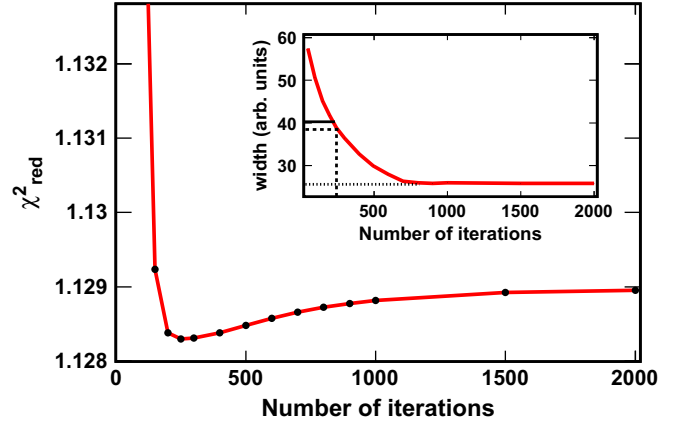


Fig. 2. Typical dependence of χ^2_{red} calculated between the measured distribution and the result of the Richardson–Lucy method with the number of iterations. The minimum χ^2_{red} and the corresponding iteration number N_{min} are indicated with a dotted line. The inset shows the behaviour of the resulting width of a peak contained in a measured distribution with the number of iterations. The true value of the width is indicated with a triangle mark. The deconvolution result converges to a minimal width (dotted line). The result from the application of the χ^2_{red} regularization method is indicated with a dashed line.

regularization matrix [19], compare small variations in the measured distribution \mathbf{Y} with the calculated $\mathbf{H} \otimes \mathbf{X}$ to assure no loss of information. A drawback of this method is the long computing time required; particularly for a systematic study of various distributions in different conditions.

In order to optimize the computing time, a relatively simple regularization method based on the χ^2 is proposed in this work. Regularization methods and stopping criteria based on the standard χ^2 are well-known in other applications such as image reconstruction techniques [20]. In some of these methods, the feasibility of the solution is measured with the χ^2 , and the process is stopped when this reaches a certain limit, preventing the solution to degrade. In the present case, we look for a minimum of the χ^2 in order to halt the deconvolution process. In addition, the collection of minima resulting from different measurements of the same observable should be centred at $\chi^2_{red} = 1$, where χ^2_{red} is the standard χ^2 normalized to the number of degrees of freedom, and correlated with the true value of the measured observable.

For each iteration of the Richardson–Lucy deconvolution, a χ^2_{red} likeness test between the measured distribution \mathbf{Y} and the convolution of both the solution \mathbf{X} and the response function \mathbf{H} is performed. Due to the histogram-nature of the three distributions, this test is done on a bin-by-bin basis

$$\chi^2_{red} = \frac{1}{(n'-1)} \sum_{i=1}^{n_{bins}} \left(\frac{Y(i) - Y^{Conv}(i)}{\varepsilon(i)} \right)^2 \quad (5)$$

where $\varepsilon(i)$ is the error associated to the measured value of $Y(i)$, and n' is the number of bins with $\varepsilon(i) > 0$. In this case, Y^{Conv} is the histogram resulting from the convolution of H and the calculated X^{Calc}

$$Y^{Conv}(i) = \sum_{j=1}^{n_{bins}} H(i-j) \cdot X^{Calc}(j). \quad (6)$$

As a side note, the method requires that the three histograms $Y(i)$, $H(i)$, and $X^{Calc}(i)$ possess identical binning.

The resulting χ^2_{red} values are evaluated as a function of the number of iterations until a minimum is found at N_{min} . The corresponding $X^{Calc}(i)$ calculated after N_{min} iterations is chosen as the optimal solution. Fig. 2 shows a typical behaviour of χ^2_{red} as a function of the number of iterations, for a numerical case with two Gaussian peaks (see Section 3.3). Right after the minimum and

N_{min} , the value of χ_{red}^2 converges around a constant value. However, the effect in the features of the resulting $X^{Calc}(i)$ can be important. The inset of the same Fig. 2 reveals the evolution of the width of a peak, with a true width of 39.7 MeV, contained in the X distribution. Its value descends and converges around 26.8, which is an underestimation of some 30%. On the other hand, the value corresponding to the minimum χ_{red}^2 is close to 39, which results in a difference of less than 2%.

In our particular unfolding problem, the nature of the experimental observables measured in the FRS spectrometer determine the conditions under which the measured distributions are to be treated: the number of detected events rules the overall statistics of the distributions, and the systematic uncertainties restrict the smallest binning to build the relevant histograms. In order to use the χ_{red}^2 as a regularization criteria, the goodness of this method must be explored against different conditions of statistics and histogram binning. In the next sections, two numerical cases are used to perform this study. These cases are chosen to resemble expected measurements in the production of Δ resonances.

3.2. First numerical test: one Gaussian-peak case

In the first case, we simulated a single peak describing the Δ resonance with a Gaussian distribution. In order to reproduce a realistic peak, the resonance distribution is centred at $E_o = -326.6$ MeV with a width of $\sigma_o = 29.9$ MeV, distributed in a histogram with limits -5860 MeV and 2428 MeV. The response function is also a Gaussian of $\sigma_{Resp} = 106.3$ MeV width. The measured distribution is the discrete convolution of both Gaussian functions.

A collection of simulated measured distributions Y is produced by varying the statistics and the binning of the histogram. Statistical fluctuations are taken into account applying Gaussian fluctuations in the contents of each bin with a variance equal to the square root of the bin content. These fluctuations are simulated with normal distributions in order to mimic the nature of the experimental measurements, where a collection of systematic uncertainties add to the statistical fluctuations, resulting in an overall Gaussian behaviour. It is important to note that, although the Richardson–Lucy method is based on Poisson distributed statistics, we assume that for a reasonable number of counts the differences between the Poisson and measured distributions reduce and therefore have a small impact on the result. On the other hand, variations on the histogram binning change the number of points available to calculate the true distribution. This effect is equivalent to changing the width of the distribution for a fixed bin size. The Richardson–Lucy deconvolution and the χ_{red}^2 -based regularization method are applied to this collection of

distributions. For each distribution, the difference between the mean value of the original peak E_o and the one obtained with the deconvolution method E_o^{Calc} is defined as

$$\delta E_o = E_o - E_o^{Calc}. \quad (7)$$

The error in the estimation of the width of the peak is calculated as a percentage

$$\delta \sigma_o = 100 \left(\frac{\sigma_o - \sigma_o^{Calc}}{\sigma_o} - 1 \right). \quad (8)$$

The panels in Fig. 3 show the behaviour of δE_o and $\delta \sigma_o$ as functions of the number of bins in the histograms for samples with different statistics. The evolution of δE_o with the histogram binning suggests a fairly constant dispersion for each set of statistics. This can be interpreted as the result of the balance between the reduction of the statistics contained in each bin as its size decreases. On the other hand, the dispersion, as expected, depends on the statistics: the figure shows this behaviour. In the case of $\delta \sigma_o$, the situation is similar: the dispersion for each set of statistics is found to be quite independent on the bin size. In both, δE_o and $\delta \sigma_o$, the overall statistics play a more important role than the bin size.

The precision and accuracy of both E_o^{Calc} and σ_o^{Calc} improve with statistics, except for low number of bins. In these cases, Fig. 3 shows that the overall better precision and accuracy of the set with largest statistics is spoiled by the behaviour of the method with larger bin sizes or, equivalently, fewer bins contained in the distribution. Table 1 summarizes the average values and dispersions of δE_o and $\delta \sigma_o$ are listed for the different sets of statistics.

3.3. Second numerical test: two Gaussian-peaks case

The measurement of distributions with more than one peak, and particularly a distribution with two peaks, is among the expected experimental cases (see Section 4). This situation can be simulated with two Gaussian distributions: one placed close to 0 MeV, and another one shifted toward negative values.

Table 1

Average deviations in the mean value (δE_o) and width ($\delta \sigma_o$) obtained unfolding a single Gaussian distribution for samples with different statistics.

Counts	$\langle \delta E_o \rangle$ (MeV)	$\langle \delta \sigma_o \rangle$ (%)
10^3	-1.8 ± 3.6	3.7 ± 8.6
10^4	0.0 ± 1.7	3.9 ± 8.8
10^5	-0.4 ± 2.3	1.7 ± 2.5
10^6	-1.4 ± 2.4	3.3 ± 6.1

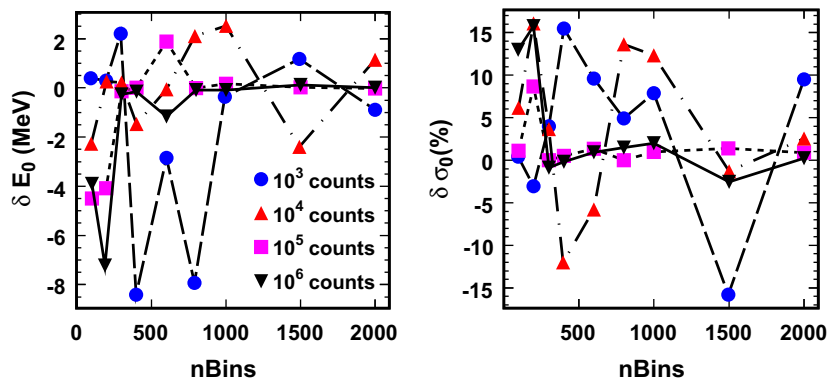


Fig. 3. Deviations in the mean value (δE_o) and width ($\delta \sigma_o$) obtained unfolding a single peak distribution as a function of the bin size and for samples with different statistics.

The response function is again a Gaussian distribution with $\sigma_{Resp} = 106.3$ MeV, and the limits of the histograms are the same as in the case of the single-peak distribution. The positions and widths of both peaks are summarized in Table 2.

As in the previous one-peak case, a collection of experimental \mathbf{Y} distributions were created by changing the statistics and the histogram binning. Again, random variations of the contents of each bin were applied according to the $Y(i)$ values in order to simulate statistical fluctuations. The statistics were equally shared by the two peaks. The Richardson–Lucy method was then applied to each \mathbf{Y} distribution to calculate the corresponding \mathbf{X}^{Calc} with the χ^2_{red} regularization test.

Fig. 4 shows the evolution of the previously defined δE_i and $\delta\sigma_i$ of each peak as a function of the bin size and for samples with

Table 2
Input parameters of the test with two Gaussian distributions.

E_1 (MeV)	E_2 (MeV)	σ_1 (MeV)	σ_2 (MeV)
−4.8	−326.6	25.1	39.7

Table 3
Average deviation in the mean values (δE_i) obtained by unfolding a two-peak distribution and average distance between the mean values of both peaks ($\delta\Delta E_i$) for samples with different statistics.

Counts	$\langle\delta E_1\rangle$ (MeV)	$\langle\delta E_2\rangle$ (MeV)	$\langle\delta\Delta E\rangle$ (%)
10^3	-0.2 ± 1.8	-0.2 ± 8.2	0.0 ± 2.6
10^4	-0.2 ± 1.1	-2.0 ± 1.9	-0.6 ± 0.7
10^5	0.1 ± 1.1	-1.3 ± 1.9	-0.4 ± 0.7
10^6	-0.1 ± 0.6	0.2 ± 0.8	0.2 ± 0.3

different statistics. The deviations in mean energy for both peaks are similar to that of the single-peak case: the behaviour shows again a stronger dependence on the statistics than on the bin size. Since the \mathbf{H}^{Calc} distribution contains two peaks, a useful information is the uncertainty on the distance between the two peaks. This deviation can be studied independently of the units of distance by making the ratio to the original distance as

$$\delta\Delta E = 100 \left(\frac{E_1^{Calc} - E_2^{Calc}}{E_1 - E_2} - 1 \right). \quad (9)$$

Table 3 shows the average deviations δE_i in the mean energy of the peaks and in the relative distance between both peaks $\delta\Delta E$, while Table 4 summarizes the average deviations $\delta\sigma_i$ in the calculated widths. In general, the accuracy and precision of the results increase with the statistics contained in the histogram \mathbf{Y} . The range of the overall variations in the width determination is within a window of $\pm 6\%$. In the case of the mean energy E_i , the least favourable test gives a result within a range of ± 8 MeV, which improves for larger statistics. The same applies to the relative distance ΔE , which is calculated within a window of less than $\pm 3\%$ in the worst case, and it reduces down to ± 0.3 for the set with 10^6 counts.

Table 4
Average deviation in the widths ($\delta\sigma_i$) obtained by unfolding a two-peak distribution for samples with different statistics.

Counts	$\langle\delta\sigma_1\rangle$ (%)	$\langle\delta\sigma_2\rangle$ (%)
10^3	-4.6 ± 7.5	-1.3 ± 15.4
10^4	-3.4 ± 6.3	-1.4 ± 5.9
10^5	2.8 ± 9.5	-1.0 ± 6.7
10^6	1.1 ± 2.1	0.6 ± 4.0

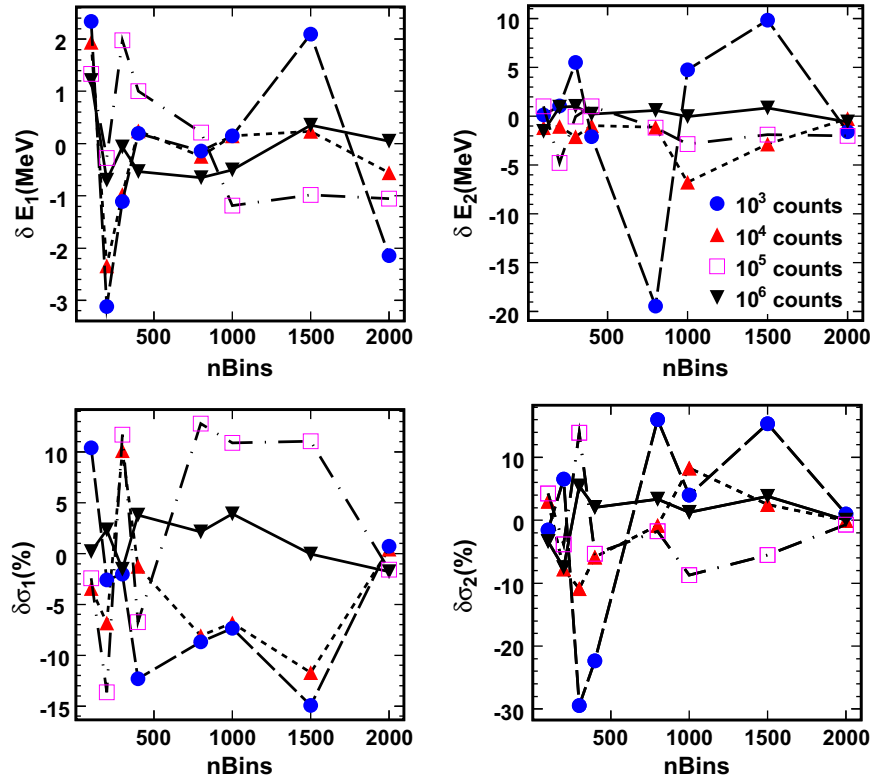


Fig. 4. Deviations in the mean value (δE_i) and width ($\delta\sigma_i$) obtained unfolding a two Gaussian-peaks distribution as a function of the bin size of the distributions and for samples with different statistics. The subscripts 1 and 2 correspond to centred and shifted Gaussian, respectively.

Fig. 5 shows a typical result of the unfolding procedure with a statistical sample of 10^6 counts at 800 bins. The true distribution (solid line) is folded with the response function used in this section, producing the folded distribution (dotted line). Using the deconvolution and the regularization methods it is possible to disentangle the original two peaks from the folded distribution. The resulting function of the deconvolution (dashed-dotted line) presents a good agreement with the true distribution.

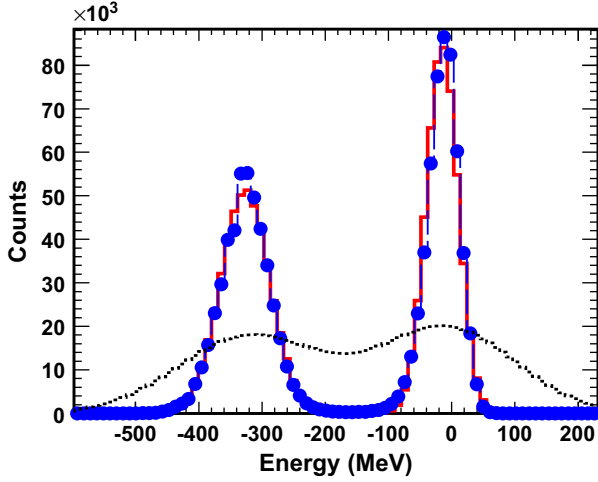


Fig. 5. Comparison between a true distribution and the result of the Richardson–Lucy and χ^2_{red} regularization procedure. The true distribution (solid line) is produced as the sum of two Gaussian-shaped peaks with a total of 10^6 counts. Then convoluted with a response function (not shown) to obtain a simulated experimental energy distribution (dotted line). The Richardson–Lucy and χ^2_{red} regularization methods are applied to this experimental distribution in order to extract the result (dotted-dashed line).

3.3.1. Correlations of calculated parameters

In general, the χ^2 value should be an indicator of the goodness of the result. In order to test this, we represent in Fig. 6 the correlation between the value of the χ^2_{red} from the deconvolution method and the deviation of the result of each parameter in the case of two Gaussian peaks (mean values and widths) respect to their corresponding true values. The panels show that the resulting values concentrate in the vicinity of the true distribution and χ^2_{red} around 1. Interestingly, there seems to be no particular correlation between the value of χ^2_{red} and the accuracy of the results at this stage.

Based on the results shown in Fig. 6, a simple mean value of each parameter would be a good approximation to the results of the deconvolution process. However, a further stage can be applied in order to improve the quality of the results: it is not unusual for deconvolution methods to yield mathematical artifacts within the set of solutions. In order to separate these anomalies, we perform a robust average of the parameters describing the peaks found in the distribution. This procedure, based on the algorithm proposed by Rousseeuw and Van Driessen [21], searches within the set of solutions the subset that minimizes the sum of the standard deviations of the parameters. The minimum size of the subset is fixed at $number\ of\ points + number\ of\ parameters + 1/2$.

3.3.2. Application on a simulated case

In the case of actual data, the true distribution X is unknown. In the particular case of isobaric charge-exchange reactions, the method extracts the widths and mean energies of the peaks associated with different reaction channels. The procedure for actual data follows a systematic application of the deconvolution and regularization methods on variations of the same set of data. The variations are performed in two ways: (a) the bin size of the $H(i)$ and $Y(i)$ histograms is changed, and (b) the content of each

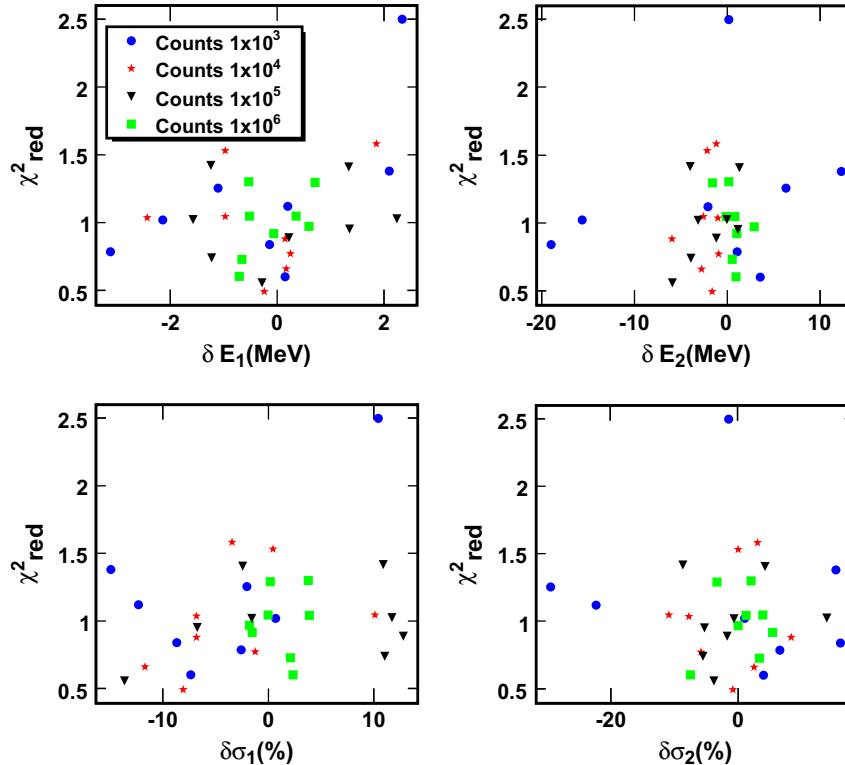


Fig. 6. Correlation between the value of the χ^2_{red} resulting from the deconvolution and regularization methods and the deviations in the mean value (δE_i) and widths ($\delta \sigma_i$) in the case of the two Gaussian-peaks distributions. Each point corresponds to the correlation for a particular binning and number of counts in the histogram.

bin is randomly modified with a variance equal to the square root of its contents, simulating statistical fluctuations. For each of these versions of the histograms, the method is applied and a set of parameters (widths and mean energies in this case) is extracted with the corresponding χ_{red}^2 .

In order to test the full procedure, this method is applied to a simulated experimental distribution. As in previous examples, two Gaussian peaks, representing the elastic and inelastic peaks are produced. To simulate a realistic situation, the inelastic peak has four times lower statistics than the elastic one. The histogram contains a total of 2000 counts (400 and 1600 counts each peak). In this practical case, the variations in the histogram binning were 100, 300, 600, and 800 bins; and for each case, a set of 12 versions of the histogram following random statistical fluctuations were performed. Fig. 7 shows the correlations between the widths of the two peaks and the resulting χ_{red}^2 for the ensemble of trials. The result after applying the preceding method is represented by the cross-point, while the dot marks the true value of the widths. Both, the result and true value are contained in a region with $\chi_{red}^2 \sim 1$, indicated by the dashed area. The final ensemble of trials converge to $\chi_{red}^2 = 1.02$, reflecting a connection between the goodness of the result and the χ_{red}^2 value. The obtained values for each parameter are summarized in Table 5.

As it can be observed in Table 5, the parameters of the first peak, E_1 and σ_1 , profit from the larger statistics, compared to the second peak. However, the true values are all within 2σ of the calculated results.

As a benchmark, the ensemble of trial histograms were also fitted to the sum of two Gaussian functions by standard χ^2 minimization. The effect of the response function was extracted from the resulting $\sigma_{Fit,i}$ by a simple subtraction of the widths

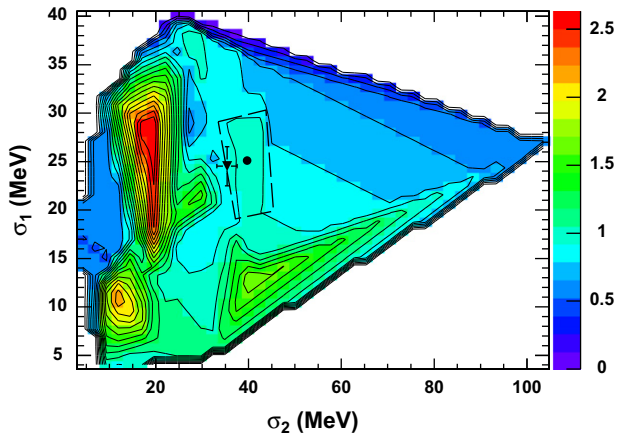


Fig. 7. Distribution of χ_{red}^2 obtained by the deconvolution and regularization methods of a two Gaussian distribution changing the binning and statistical fluctuation in the histogram as a function of the resulting widths of the two peaks σ_2 and σ_1 . The area enclosed with the dashed-line indicates the region where $\chi_{red}^2 \approx 1$. The dot inside of the dashed-line area marks the true value and the triangle correspond to the deconvolution result.

Table 5

Comparison between the final results of the deconvolution method, the results from a standard fit, and the input values (true values) in the case of two Gaussian peaks. See text for details.

Parameter	Deconvolution	Fit	True value
E_1 (MeV)	-13.8 ± 1.9	-21.2 ± 3.0	-14.6
E_2 (MeV)	-330.9 ± 4.1	-333.4 ± 3.0	-326.6
σ_1 (MeV)	25.6 ± 2.4	23.9 ± 5.7	25.1
σ_2 (MeV)	35.2 ± 3.3	39.2 ± 6.1	39.7

squared: $\sigma_i^2 = \sigma_{Fit,i}^2 - \sigma_{resp}^2$. The comparison is also summarized in Table 5. The performance of both approaches are similar. However, the main advantage of the method presented here is that no assumptions on the shape of the peaks or their relative weight are needed. On the other hand, the effect of the response function is not removed based on assumptions on its shape (as in the case of a standard fit), but by using the deconvolution method with whatever shape the response function may have (see Section 2).

4. Characterization of the Δ resonance excited in isobar charge-exchange reactions induced by ^{136}Xe projectiles at 500 A MeV

The excitation of the Δ resonance in isobar charge-exchange collisions between protons and ^{136}Xe nuclei at relativistic energies was investigated as a validation case. This particular reaction has the interest that the production of ^{136}I is only possible via the excitation of the Δ resonance, while the production of ^{136}Cs may occur via the quasi-elastic or the resonant charge-exchange channels. Therefore, the unfolding of the single-peak momentum or energy distribution of ^{136}I could be done using an analytical method that will serve to benchmark the numerical procedure proposed in this work.

4.1. Experiment

This reaction was investigated at the GSI facilities in Darmstadt taking advantage of the inverse-kinematic technique. The SIS100 synchrotron was used to accelerate a beam of ^{136}Xe up to an energy of 500 A MeV. These projectiles impinged on a liquid hydrogen target encapsulated by a container with 36.3 mg/cm² titanium windows. The thickness of liquid hydrogen was 87.3 mg/cm². Thanks to the kinematics, projectile residues flying forward were identified in atomic and mass number, but also analyzed in momentum using the magnetic spectrometer FRS described in Section 2.

The identification of the projectile residues was obtained from the combined measurement of their magnetic rigidity, time of flight, and energy loss. In the particular case of the FRS, two plastic scintillators [22], located at the intermediate and final image planes, and covering the full acceptance window of the spectrometer, provided not only the time-of-flight of the nuclei but also their positions along the dispersive coordinate. These two measurements were then used to determine the velocities and the magnetic rigidities of the transmitted nuclei. Moreover, an ionization chamber [23], placed at the exit of the separator, provided the energy loss measurement of the nuclei and, from there, its atomic number. From the magnetic rigidity, velocity and atomic number, one could directly deduce the mass number. A detailed description of the experimental technique and data sorting can be found in Ref. [24].

The resolving power of the spectrometer, together with the resolution in position (~ 2 mm) and time of flight (~ 150 ps FWHM) provided by the plastic scintillators, yielded an excellent separation of the different projectile fragments, as shown in Fig. 8. In this figure, we display in a cluster plot the atomic number versus the mass-over-charge ratio for the nuclei transmitted in two magnetic tunings of the FRS centred on ^{122}Cd and ^{119}Cd . In this figure, each spot corresponds to a different nucleus or an atomic charge state. Using the primary beam as reference one could then identify the transmitted nuclei. In particular, we can clearly observe in this identification plot the primary beam, ^{136}Xe , but also the production of ^{136}Cs and ^{136}I , the two isobar charge-exchange channels produced by the projectile nuclei impinging on the hydrogen target.

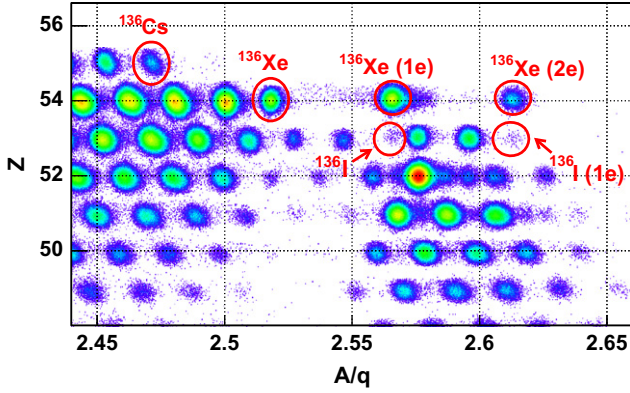


Fig. 8. Cluster plot of atomic number (Z) versus the ratio mass-over-charge (A/q) of the projectile residues transmitted by FRS in two magnetic tunings centred in ^{122}Cd and ^{119}Cd .

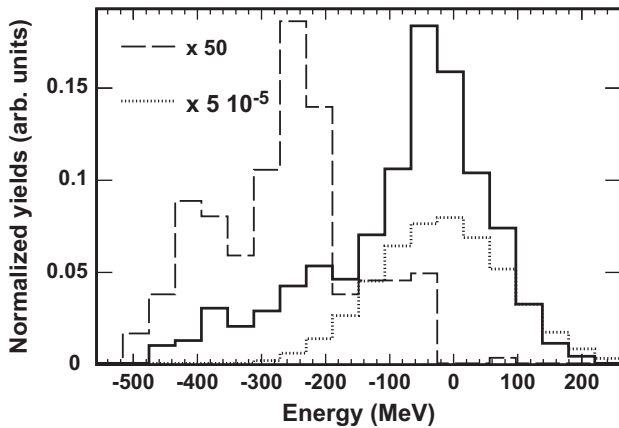


Fig. 9. Energy distribution in the frame of incoming projectiles in the middle of the target for the two residual nuclei produced in the isobar charge-exchange reactions investigated in this work: ^{136}Cs (solid line) and ^{136}I (dashed line). The energy distribution of beam of particles ^{136}Xe (dotted line) is also shown.

4.2. Energy distributions

In order to investigate the excitation of the Δ resonance, we reconstructed the recoiling energy of the projectile residues produced in the two isobar charge-exchange channels investigated in this work, ^{136}Cs and ^{136}I . Energies were obtained from the magnetic rigidities of the events corresponding to these reaction channels. As already mentioned in Section 2, the intrinsic resolution in magnetic rigidity obtained with the FRS is of the order of 6×10^{-4} and, when considering the electromagnetic interactions in the hydrogen target, the final resolution achieved is of the order of 3×10^{-3} . In any case, this resolution is better than the one obtained from time-of-flight measurements.

To correct from reactions in the titanium windows of the hydrogen container, measurements with empty target were also performed and the corresponding energy spectra were subtracted bin per bin from the measurements with the full target (windows plus hydrogen). Fig. 9 shows these energy spectra transformed into the reference frame defined by the energy of the incoming projectile in the middle of the hydrogen target.

The energy distribution of ^{136}Cs shown in Fig. 9 (solid line) presents a dominant contribution around energy zero, compatible with a quasi-elastic (n,p) charge-exchange, and a long tail of events with negative energy. This tail corresponds to collisions where the produced ^{136}Cs nuclei have lost a significant amount of kinetic energy when compared to the one of the incoming

projectiles. In the case of ^{136}I (dashed line) the main features are the small amount of events around energy zero and a bump at energies between -200 and -400 MeV. This last spectrum is fully compatible with the (p,n) charge-exchange in reactions between ^{136}Xe and protons, where the quasi-elastic channel is forbidden by charge conservation, and the only possibility would be the charge-exchange via the excitation of the Δ resonance. In order to be more quantitative, the resolution in energy obtained in these measurements could be improved by unfolding the measured spectra from the response function of our experimental device. In this experiment, the measured energy distribution of the primary beam (dotted line in Fig. 9) provide us with the response function of the FRS and its associated detection setup. Indeed the ^{136}Xe projectiles traverse the spectrometer in identical conditions as the charge-exchange residues. The difference by one unit in atomic or mass number represents a negligible effect.

4.3. Characterization of the Δ resonance

The measured energy distributions of ^{136}Cs and ^{136}I were unfolded from the response function of the spectrometer, represented by the energy distribution of ^{136}Xe . We followed the procedure described in Section 3 to unfold the two humped energy distribution of ^{136}Cs , using the regularization technique based on a χ^2 -likeness test between the measured energy distribution and the convolution of both the solution and the response function, as a function of the number of bins in the three histograms. The result of this test is shown in Fig. 10, which is an analogue to Fig. 7. The number of bins used for the test were 100, 300, and 600. The statistics per bin was changed as random fluctuations of a Gaussian distribution with a variance equal to the sum of statistical and systematic uncertainties. In the figure, the dashed line delimits the region with $\chi_{red}^2 \approx 1$, representing the set of solutions that best describe the measured distributions. Moreover, in the same figure, the point inside of the dashed area is the result extracted from the correlation between the four parameters, i.e. the mean values and widths of each peak. After applying the correlation between the parameters, the χ_{red}^2 of the final ensemble of trials converge to $\chi_{red}^2 = 1.13$.

The single humped energy distribution from ^{136}I was unfolded using a similar procedure and regularization technique. In this particular case, and assuming Gaussian distributions for the measured energy distribution for ^{136}I and for the response function of the experimental device, one can also perform an analytical unfolding via the simple quadratic subtraction of the widths of both distributions.

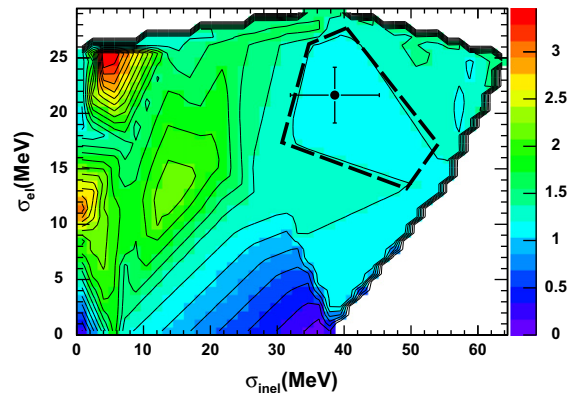


Fig. 10. Distribution of χ_{red}^2 obtained by the deconvolution and regularization methods of a experimental distribution changing the binning and statistical fluctuation in the histogram as a function of the resulting widths of the two peaks σ_2 and σ_1 . The area enclosed with the dashed-line indicates the region where $\chi_{red}^2 \approx 1$. The point inside of the dashed-line area marks the result extracted from the correlation between the four parameters.

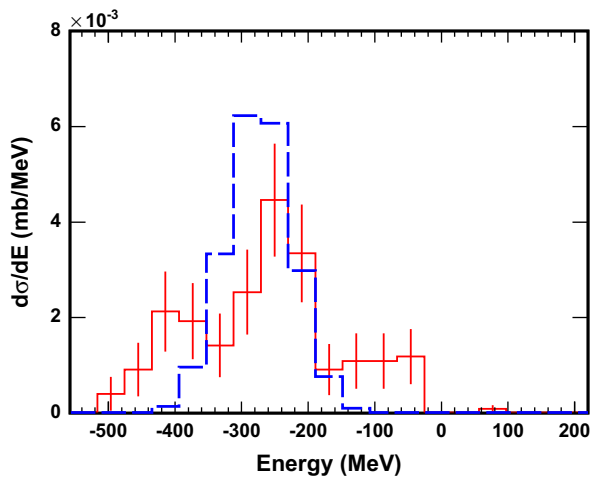


Fig. 11. Measured (solid line) and unfolded (dashed line) energy distribution in the reference frame defined by the energy of the projectiles in the middle of the target for ^{136}I nuclei produced in isobar (p,n) charge exchange reactions induced by ^{136}Xe at 500 A MeV. Error bars represent statistical and systematic uncertainties.

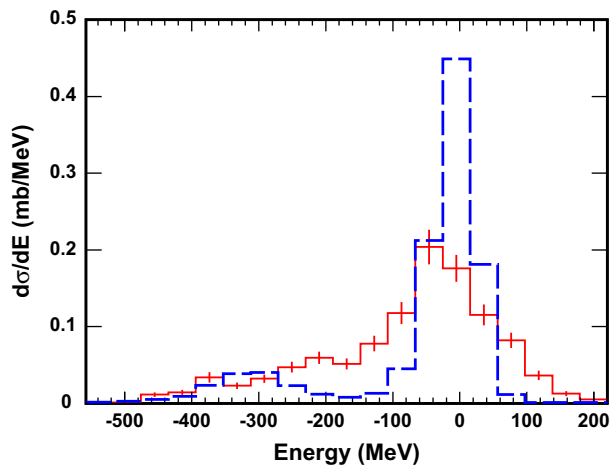


Fig. 12. Measured (solid line) and unfolded (dashed line) energy distribution in the reference frame defined by the energy of the projectiles in the middle of the target for ^{136}Cs nuclei produced in isobar (n,p) charge exchange reactions induced by ^{136}Xe at 500 A MeV. Error bars represent statistical and systematic uncertainties.

Table 6

Mean energy and full widths at half-maximum for the quasi-elastic and inelastic peaks of the recoiling energy distribution for ^{136}Cs and the single humped distribution for ^{136}I as obtained using the unfolding technique but also analytical Gaussian fits in the case of the $^{136}\text{I}_G$.

Channel	E_{el} (MeV)	E_{inel} (MeV)	Γ_{el}	Γ_{inel}
$^{136}\text{I}_G$	–	-274.3 ± 17.5	–	95.3 ± 18.4
^{136}I	–	-276.2 ± 23.8	–	127.1 ± 30.7
^{136}Cs	-24.1 ± 1.1	-343.7 ± 12.7	50.9 ± 13.8	90.7 ± 30.9

In Figs. 11 and 12 are displayed the measured and unfolded energy distributions for ^{136}I and ^{136}Cs , respectively. In the case of ^{136}Cs , the unfolded distribution shows two well separated components: one around zero and the second one around -300 MeV. In Fig. 11, the unfolding of the ^{136}I energy distribution yields a single peak centred also around -300 MeV. We can then conclude that both peaks at negative energies in the two distributions should be produced by the same reaction mechanism. Moreover, the fact that the quasi-elastic component around

energy zero is not present in the ^{136}I distribution clearly indicates that the peaks we observe at negative energies are due to the excitation of the Δ resonance. In order to be more quantitative, in Table 6 we present the parameters characterizing the energy distributions of ^{136}Cs and ^{136}I , corrected by the resolution of the experimental device used in this experiment. The uncertainty in the determination of the mean value and width of the distributions was around 5% and 30%, respectively. It is worthy to note that these uncertainties are also a consequence of the relatively low-statistics. In this table we also present the results obtained for the energy distribution of ^{136}I using two different unfolding techniques: the one proposed in this work and the result ($^{136}\text{I}_G$) of the analytical unfolding of two Gaussian functions representing the Δ peak and the spectrometer response function. The good agreement between the two results can be used as validation of the unfolding technique we are proposing. On the other hand, the mean energy and width of the peak located at negative energies agrees with the expected values for the Δ resonance.

We can then conclude that the present results clearly demonstrate the identification of the Δ resonance in relativistic heavy-ion collisions investigated with the magnetic spectrometer FRagment Separator. Moreover, the observation of the Δ resonance in isobar charge-exchange collisions also ensures that pions emitted in the Δ decay escape from the nuclear medium and, consequently, the Δ should be excited at the periphery of the nucleus.

5. Conclusion

In this work, we make use of an unfolding procedure based on the Richardson–Lucy method to investigate the excitation of the Δ resonance in isobaric charge-exchange reactions induced by relativistic heavy-ions. This unfolding method includes a regularization technique based on a χ^2 test between the measured distribution and the one obtained by folding the result with the response function. This χ^2 -likeness test provides the optimum number of iterations for the unfolding according to the binning and statistical significance of the measured distributions. The results obtained with two numerical distributions, with one and two peaks, indicate that the relevant parameter determining the final accuracy of the deconvolution is the statistical significance of the measurement.

The unfolding and regularization techniques presented in this work were used to investigate the Δ -resonance excitation in isobar charge-exchange reactions induced by ^{136}Xe projectiles impinging on a liquid hydrogen target at 500 A MeV. The magnetic spectrometer FRS at GSI was used not only to identify the two isobar charge-exchange nuclei, ^{136}Cs and ^{136}I , but also to determine its recoiling momentum (energy) with high accuracy. Unfolding the energy distribution of ^{136}Cs residual nuclei, we obtained a double peak distribution in the reference frame of the energy of the incident projectile in the middle of the target: with a peak around zero energy and a second peak corresponding to collisions where the ^{136}Cs nuclei have lost, on average, 300 MeV. The energy distribution of ^{136}I nuclei showed a single peak indicating that all events observed in this case correspond to an energy lost around 300 MeV. The two peaks observed in the production of ^{136}Cs were identified as the quasi-elastic and Δ -resonance channels of the (n,p) charge-exchange. In the case of ^{136}I , the proton target prevents the (p,n) quasi-elastic charge-exchange. This reaction is only mediated by the excitation of the Δ resonance. Moreover, the unfolding technique made it possible to determine the mean energy and width of the Δ resonance with resolutions around 5% and 30% respectively in a relatively low-statistics data set.

Acknowledgements

This work was partially funded by the Spanish Ministry for Science and Innovation under grant FPA2010-22174-C02-01, the programme “Ingenio 2010, Consolider CPAN”, and the programme “Grupos de referencia competitiva Xunta de Galicia” under Grant 2010/57. M.C. acknowledges the support provided by the Spanish Ministry of Science and Innovation through the programme “Juan de la Cierva”. Discussions with Juan Alcántara are acknowledged.

References

- [1] B.E. Bonner, et al., *Physical Review C* 18 (1978) 1418.
- [2] D. Contardo, et al., *Physics Letters B* 168 (1986) 331.
- [3] C. Ellegard, et al., *Physical Review Letters* 50 (1983) 1745.
- [4] E. Grorud, et al., *Nuclear Instruments and Methods in Physics Research* 188 (1981) 549.
- [5] H. Geissel, et al., *Nuclear Instruments and Methods in Physics Research Section B* 70 (1992) 286.
- [6] A. Kelic, et al., *Physical Review* 70C (2004) 064608.
- [7] D. Pérez-Loureiro, et al., *Physics Letters B* 703 (2011) 552.
- [8] W.H. Richardson, *Journal of the Optical Society of America* 62 (1972) 55.
- [9] L.B. Lucy, *Astrophysics Journal* 79 (1974) 745.
- [10] V. Panaretos, in: H.B. Prosper, L. Lyons (Eds.) *Proceedings of PHYSTAT 2011 Workshop on Statistical Issues Related to Discovery Claims in Search Experiments and Unfolding*, CERN, Geneva, Switzerland, 17–20 January 2011, CERN-2011-006, p. 229.
- [11] J.P. Schaffer, et al., *Nuclear Instruments and Methods in Physics Research Section B* 5 (1981) 75.
- [12] Y. Kong, K.G. Lynn, *Nuclear Instruments and Methods in Physics Research Section A* 302 (1991) 145.
- [13] P.H. Van Cittert, *Zeitschrift für Physik* 69 (1933) 298.
- [14] P. Bandžuch, et al., *Nuclear Instruments and Methods in Physics Research Section A* 384 (1997) 506.
- [15] M. Morháč, et al., *Nuclear Instruments and Methods in Physics Research Section A* 401 (1997) 385.
- [16] H.B. Prosper, L. Lyons (Eds.) *Proceedings of PHYSTAT 2011 Workshop on Statistical Issues Related to Discovery Claims in Search Experiments and Unfolding*, CERN, Geneva, Switzerland, 17–20 January 2011, CERN-2011-006.
- [17] G. D’Agostini, *Nuclear Instruments and Methods in Physics Research Section A* 362 (1995) 48.
- [18] V.B. Anykeyev, et al., *Nuclear Instruments and Methods in Physics Research Section A* 303 (1991) 350.
- [19] J. Albert, et al., *Nuclear Instruments and Methods in Physics Research Section A* 583 (2007) 494.
- [20] E. Veklerov, J. Llacer, *IEEE Transactions on Medical Imaging* 6 (4) (1987) 313.
- [21] P. Rousseeuw, K. Van Diessen, *Data Mining and Knowledge Discovery* 12 (2006) 29.
- [22] B. Voss, et al., *Nuclear Instruments and Methods in Physics Research Section A* 364 (1995) 150.
- [23] M. Pfützner, et al., *Nuclear Instruments and Methods in Physics Research Section B* 86 (1994) 213.
- [24] J. Benlliure, et al., *Physical Review C* 78 (2008) 054605.

APPENDIX C

Measured Cross Sections

Charge exchange cross sections at 1GeV using stable beams

Beam	Target	Product	Cross section (mb)	f_d	$f_{ch.st.}$	f_{sec}
^{124}Sn	proton	^{124}Sb	0.37 ± 0.04	1.49	1.02	1.06
^{124}Sn	C	^{124}Sb	0.79 ± 0.09	1.49	1.02	1.06
^{124}Sn	Cu	^{124}Sb	0.92 ± 0.10	1.48	1.01	1.06
^{124}Sn	Pb	^{124}Sb	1.07 ± 0.12	1.48	1.02	1.06
^{112}Sn	proton	^{112}Sb	0.36 ± 0.04	1.50	1.02	1.06
^{112}Sn	C	^{112}Sb	0.72 ± 0.08	1.50	1.02	1.06
^{112}Sn	Cu	^{112}Sb	0.83 ± 0.09	1.33	1.01	1.05
^{112}Sn	Pb	^{112}Sb	1.03 ± 0.10	1.62	1.01	1.05
^{112}Sn	proton	^{112}In	0.07 ± 0.01	1.40	1.03	1.05
^{112}Sn	C	^{112}In	0.25 ± 0.02	1.40	1.03	1.05
^{112}Sn	Cu	^{112}In	0.45 ± 0.05	1.40	1.03	1.05
^{112}Sn	Pb	^{112}In	0.57 ± 0.06	1.40	1.03	1.05

Table C.1: Charge exchange reaction cross sections using ^{124}Sn and ^{112}Sn stable beams at 1GeV/u. Correction factors are shown for each nucleus: f_d , f_s $f_{ch.st}$ are the dead time, secondary reactions and charge states correction factors respectively.

Production cross-sections

Product	Cross section (mb)	Product	Cross section (mb)
^{106}Rh	0.02 ± 0.01	^{110}Ag	0.014 ± 0.003
^{105}Rh	0.01 ± 0.02	^{109}Ag	0.52 ± 0.10
^{104}Rh	0.50 ± 0.12	^{108}Ag	0.82 ± 0.17
^{103}Rh	1.15 ± 0.24	^{107}Ag	3.56 ± 0.74
^{108}Pd	0.03 ± 0.01	^{111}Cd	0.57 ± 0.12
^{107}Pd	0.17 ± 0.04	^{110}Cd	4.35 ± 1.09
^{106}Pd	0.82 ± 0.16	^{109}Cd	7.62 ± 1.60
^{105}Pd	1.26 ± 0.26		

Table C.2: Isotopic cross-section measured in the reaction of ^{112}Sn on carbon target at 1 A GeV.

Bibliography

- [1] Aumann. T. *Eur. Phys. J. A.* , 20:441, 2005.
- [2] Glauber R J. *Lecture Notes on Theoretical Physics*, 1, 1959.
- [3] Hussein M.,Rego R and Bertulani C. *Phys. Rep.*, 201:279, 1991.
- [4] Kerman A.K., MacManus H. and Thaler R. *Ann. Phys.*, 8:551, 1959.
- [5] Al-Khalilli J. NunesF. *J. Phys. G.*, 29, 2003.
- [6] Johnson R.C. and Soper P.J.R. *Phys. Rev. C.*, 1:976, 1970.
- [7] Metropolis N., Bivins R. , Storm M. et al. . *Phys. Rev.*, 110:185, 1958.
- [8] Bowman, J.D.,Swiatecki, W.J.,Tsang, C.F. *Lawrence Berkeley Laboratory report* , 2908:1, 1973.
- [9] Bertini H.W. *Phys. Rev.*, 131:1801, 1963.
- [10] J. Cugnon . *Nucl.Phys. A* , 462:751, 1987.
- [11] J. Cugnon, C Volant and Vuillier . *Nucl.Phys. A* , 620:475, 1997.
- [12] Cugnon J. and Henrotte P. . In Filges D., Goldenbaum F. et al., editor, *Proceedings of the Fifth Workshop on Simulating Accelerator Radiation Enviroments*, page 65. Julich Publications, 2001.
- [13] A. Boudard, J. Cugnon, S. Leray, C. Volant. Intranuclear cascade model for a comprehensive description of spallation reaction data. *Phys. Rev. C*, 66:615, 2002.

-
- [14] J. Tostevin, G.Podolyak, B. A. Brown and P.G. Hansen. *Phys. Rev. C*, 70:064602, 2004.
- [15] J. Tostevin, B. A. Brown . *Phys. Rev. C*, 74:064604, 2006.
- [16] Morrissey D.J., W.R. Marsh, R.J. Otto et al. *Phys. Rev. C*, 18:1267, 1978.
- [17] Oliveira L.F., R. Donangelo et al. *Phys. Rev. C*, 19:856, 1979.
- [18] Gaimard J.J. and K.-H Schmidt. *Nuclear Physics A*, 531:709, 1991.
- [19] Hüfner, Schäfer K. and Schürmann B. . *Phys. Rev. C.*, 12:1888, 1975.
- [20] A. Kelic and K-H. Schmidt. Report indc(nds)-0530,vienna. Technical report, IAEA, 2008.
- [21] Tanihata I. et al. *Phys Lett. B*, 160:380, 1985.
- [22] Tanihata I. et al. . *Phys. Lett. B.*, 289:261, 1992.
- [23] Chulkov et al. . *Nucl. Phys. A.*, 603:219, 1996.
- [24] Alkhazov et al. . *Phys. Rev. Lett.*, 78:2313, 1997.
- [25] Ozawa A. et al. *Nucl. Phys. A*, 734:315, 2004.
- [26] Kox S. et al. *Phys. Rev. C* , 35:1678, 1987.
- [27] Mittig W. et al. *Phys. Rev. Lett.*, 59:1889, 1987.
- [28] Saint-Laurent M.G. et al. *Z. Phys. A* , 332:457, 1989.
- [29] Villari A.C.C. et al. *Phys Lett. B*, 268:345, 1991.
- [30] Negoita F. et al. *Phys. Rev. C*, 54:1787, 1996.
- [31] Warner R.E. et al. *Phys. Rev. C* , 52:1166, 1995.
- [32] Licot I. et al. *Phys. Rev. C*, 56:250, 1997.
- [33] Aissaoui N. et al. *Phys. Rev. C*, 60:03614, 1999.
- [34] Fukuda M. et al. *Phys Lett. B*, 268:339, 1991.
- [35] Fukuda M. et al. *Nucl. Phys. A*, 656:209, 1999.
- [36] Fang D.Q. et al. *Phys. Rev. C*, 61:064311, 2000.

-
- [37] Sick I. et al. *Prog. Part. Nucl. Phys.*, 47:245, 2001.
- [38] Wang L. B. et al. *Phys Rev. Lett.*, 93:142501, 2004.
- [39] Sánchez R. et al. . *Phys Rev. Lett.*, 96:033002, 2006.
- [40] Mueller P. et al. *Phys Rev. Lett.*, 99:252501, 2007.
- [41] Krieger A. et al. *Phys Rev. Lett.*, 108:142501, 2009.
- [42] Nörthershäuser W. et al. *Phys Rev. Lett.*, 102:062503, 2009.
- [43] Suzuki T. , Sagawa H. and Hagino K. *Phys. Rev. C.*, 68:014317, 2003.
- [44] Webber W.R. et al. *Phys. Rev. C* , 41:520, 1990.
- [45] Chulkov L. et al. *Nucl. Phys. A*, 602:219, 1996.
- [46] Chulkov L. et al. *Phys Lett. B*, 674:330, 2000.
- [47] Estradé A. et al. private communication, 2014.
- [48] Terashima et al. private communication, 2014.
- [49] Hansen P.G. and Tostevin J.A. *Annu. Rev. Nucl. Part. Sci.*, 53:219, 2003.
- [50] Cortina-Gil D. *Lecture Notes in Physics 879*, chapter Chapter 5. Springer Verlag, 2014.
- [51] Orr N.A. et al. *Phys. Rev. Lett.* , 69:2050, 1992.
- [52] K.-Schmidt,K. Sümmerer, H. Geissel et al. *Nucl. Instr and Meth. B*, 142:441, 1998.
- [53] Aumann T. et al. *Phys. Rev. Lett.* , 84:35, 2000.
- [54] Cortina-Gil D. et al. *Phys. Lett. B* , 529:36, 2002.
- [55] Kanungo R. . *Phys. Scr. T*, 152:014002, 2013.
- [56] Tanihata I., Savajols H. and Kanungo R. *Prog. Nucl. Phys.*, 68:215, 2013.
- [57] Terry J.R. et al. . *Phys. Lett B*, 640:86, 2006.
- [58] Maierbeck P. et al. . *Phys. Lett B*, 675:22, 2009.

- [59] Gade et al. A. . *Phys. Rev C*, 77:044306, 2008.
- [60] C. Bertulani and G. Baur . *Phys. Rep.*, 163:299, 1998.
- [61] Aumann T. , Bortignon P.F. and Emling H. . *Ann. Rev. Nuc. Part. Sci*, 48:351, 1998.
- [62] Aumann T. et al. . *Phys. Rev C*, 59:1252, 1999.
- [63] Leistenschneider A. et al. . *Phys. Rev. Lett*, 86:5442, 2001.
- [64] Adrich P. et al. . *Phys. Rev. Lett*, 95:132501, 2005.
- [65] Klimkiewicz A. et al . *Phys. Rev C*, 76:051603, 2007.
- [66] Rossi D. et al . *Phys.Rev.Lett.*, 111:242503, 2013.
- [67] Nakamura et al. . *Phys. Rev Letters*, 83:1112, 1999.
- [68] Palit R. et al. . *Phys. Rev C*, 68:034218, 2003.
- [69] Datta Pramanik U. et al. . *Phys. Lett. B*, 551:63, 2003.
- [70] Schümann F. et al. . *Phys. Rev. Lett.*, 90:232501, 2003.
- [71] Schümann F. et al. . *Phys. Rev C*, 73:015806, 2006.
- [72] Hammache F. et al. . *Phys. Rev C*, 82:065803, 2010.
- [73] Frekers D. *Prog. Part. Nucl. Phys.*, 57:217, 2006.
- [74] Frekers D. *Prog. Part. Nucl. Phys.*, 64:281, 2010.
- [75] Wong S.M . *Introductory Nuclear Physics*. Prentice Hall,New Jersey, 1990.
- [76] Bertsch G F and Esbensen H. *Rep. Prog. Phys*, 50:607, 1987.
- [77] Y. Fujita, B. Rubio, W. Gelletly. *Progress in Particle and Nuclear Physics*, 66:549, 2011.
- [78] S.J. Lindenbaum and R.M. Sternheimer . *Phys. Rev. 105* , 105:1874, 1957.
- [79] M. Fernández. *Peripheral collisions induced by ^{124}Xe and ^{136}Xe projectiles at relativistic energies*. PhD thesis, Universidad Santiago de Compostela, Spain, 2007.

-
- [80] Franey, Love. *Phys. Rev. C*, 31:488, 1985.
- [81] Gaarde, C., J. Rapaport, T.N. Taddeucci, C.D. Goodman, C.C. Foster et al. *Nucl. Phys. A.*, 369:258, 1981.
- [82] Moake, G.L., L.J. Gutay, R.P. Scharenberg, P.T. Debevec, and P.W. Quin. *Phys. Rev. Lett.*, 43:910, 1979.
- [83] Anderson, B.D., J.N. Knudson, P.C. Tandy, J.W. Watson, R. Madey, and C.C. Foster. *Phys. Rev. Lett.*, 45:699, 1980.
- [84] Ikeda, K.S. Fuijii and J.I. Fujita. *Phys. Lett.*, 3:271, 1963.
- [85] Gutierrez, C, De Sanctis, M. *Pramana, Journal of Physics*, 72:541, 2009.
- [86] C. Amsler et al. *Phys. Lett. B*, 667:1, 2008.
- [87] Gaarde, C. *Annu. Rev. Nucl. Part. Sci.*, 41:187, 1991.
- [88] Osterfeld, F. *Rev. Mod. Phys.*, 64:491, 1992.
- [89] E. Groun, et al. *Nuclear Instruments and Methods in Physics Research*, 188:549, 1981.
- [90] Bachelier, D et al. *Phys. Lett. B.*, 172:23, 1986.
- [91] H. Geissel, et al. *Nucl. Instr. Meth. B*, 70, 1992.
- [92] Manley, D.M. *Phys. Rev. D*, 51:9, 1995.
- [93] Roper, L.D. *Rev. Lett.*, 12:340, 1964.
- [94] M. Steiner, M. Blasche, HG Clerc, et al. *Nucl. Instrum. and Methods A*, 312:420, 1992.
- [95] R. Anne, A. Lefol, G Milleret and R. Perret. *Nucl. Instr and Meth.*, 152:395, 1985.
- [96] B. Jurado, K.H. Schmidt and K.H. Behr. *Nucl. Instr and Meth. A*, 483:603, 2002.
- [97] N. Iwasa et al. *Nucl. Instr. Meth. B*, 126:284, 1997.
- [98] K.L. Brown. *SLAC-Report*, 91, 1970.
- [99] <http://www.usc.es/genp/s364.html>.

-
- [100] B. Voss , T, Brohm, H.G Clerc , et al. *Nucl. Instr. Meth. A.*, 364:150, 1995.
- [101] M. Pützner, H. Geissel,G Münzenberg, F. Nickel , et al . *Nucl. Instrum. and Methods B*, 86:213, 1994.
- [102] V. Hlinka et al . *Nucl. Instr. Meth. A*, 419:503, 1998.
- [103] R. Janik, A. Prochazca, B Sitar, P. Strmen, I. Szarczka, H. Geissel,K.-H Behr, C. Karagiannis . *Nucl. Instr. Meth. A*, 640:54, 2011.
- [104] Carey D.C . *The Optics of the Charged Pericles Beams*. Harwood Academic Publishers, 1987.
- [105] K-H Schmidt, E. Hanelt, H Gissel, G. Munzenberg, and J.P. . *Nucl. Instr. Meth. A* , 260:150, 1987.
- [106] J. Vargas, J. Benlliure, and M. Caamaño. *Nucl. Instr. Meth. A*, 707:16, 2013.
- [107] G. D Agostini . *Nuclear Instruments and Methods in Physics Reseach A*, 362:48, 1995.
- [108] Veklerov E., J. Lacer . *IEEE Transitions on Medical Imaging* 6, 4:313, 1987.
- [109] Albert J. . *Nuclear Instruments and Methods in Physics Reseach A*, 583:350, 2007.
- [110] P. Rousseeuw, K. Van Diessen. *Data Mining and Knowledge Discovery*, 12:29, 2006.
- [111] P.J Karol. *Phys. Rev. C* , 11:1203, 1975.
- [112] C. Scheidenberger,Th. Stöhlker. W.E. Meyerhof, H. Geissel, P.H. Mokler, B.Blank . *Nucl. Instr and Meth. B*, 142:441, 1998.
- [113] C.Scheidenberger et al. *Nucl. Instr. Meth. B.* , 142:441, 1998.
- [114] Roy-Stephan, M. *Nucl. Phys. A.*, 488:187, 1988.
- [115] Kelic, A. et al. *Physical Review C.*, 70:064608, 2004.
- [116] H. Seitz. *Nucl. Instr. Meth.*, 86:157, 1970.
- [117] J. Cugnon, J. Vandermeulen, and D. L'Hote. *Nucl. Instr. Meth. B*, 111:215, 1996.

- [118] Vidaña I. private communication, 2014.
- [119] Morsh H.P., Zurpranski P. . *Phys. Rev. C*, 61:024002, 1999.
- [120] Krpic D., Drndarevich S et al. *Eur. Phys. J. A*, 20:351, 2004.
- [121] Bertulani C.A. private communication, 2013.
- [122] Bohr N. *Nature* , page 344, 1936.
- [123] Weisskopf V. *Phys. Rev.* , 52:295, 1937.
- [124] Weisskopf V., Erwing D.H. *Phys. Rev.* , 57:472, 1940.
- [125] Hauser W. and Feshbach H. *Phys. Rev.*, 87:366, 1952.
- [126] Bohr N. and Wheeler J.A. *Phys. Rev.*, 56:426, 1939.
- [127] K.-H Schmidt, T, Brohm, H.G Clerc , et al. *Physics Letters B*, 300:313, 1993.
- [128] L. Audirac, A. Obertelli, P. Doornenbal et al. *Phys. Rev. C.* , 88:041602, 2013.
- [129] D. Pérez et al. . *Phys. Lett. B.* , 703:552, 2011.
- [130] http://igfae.usc.es/~genp/index.php?option=com_content&view=article&id=88&Itemid=3.
- [131] <http://www.gsi.de>.

Resumen en Castellano

El objetivo de este trabajo de tesis doctoral es estudiar excitaciones nucleares y subnucleares utilizando reacciones periféricas de núcleos pesados inducidas por proyectiles relativistas de núcleos estables e inestables. En particular se propone estudiar estas excitaciones usando reacciones de intercambio de carga isóbaras y de arranque de nucleones.

Las reacciones de intercambio de carga corresponden a excitaciones espín-isoespín que pueden proporcionar información sobre la componente isovectorial de la fuerza nuclear. Estas excitaciones pueden manifestarse en dos rangos de energía disipada en la reacción que las induce. A baja energía ($E < 100$ MeV) estos intercambios de carga cuasielásticos dan lugar a excitaciones nucleares (Fermi, Gamow-Teller, spin-dipole, cuadrupolar, etc.) y se interpretan mediante el intercambio virtual de mesones cargados entre los núcleos proyectil y blanco. En el caso de excitaciones de mayor energía ($E > 100$ MeV) el proceso se explica mediante excitaciones de resonancias subnucleares y su desexcitación mediante la emisión de mesones cargados que escapan del medio nuclear. En este trabajo nos centramos en el estudio de las reacciones de intercambio de carga en el rango de mayor energía. En particular proponemos demostrar que se pueden producir e identificar bariones en materia nuclear asimétrica y eventualmente estudiar cómo las propiedades de estos bariones cambian en este medio. Por otra parte también queremos utilizar el carácter periférico de estas reacciones de intercambio de carga, impuesto por la condición de que los mesones emitidos escapan del medio nuclear, para investigar la abundancia relativa de protones y neutrones en la superficie de los núcleos que participan en la colisión.

En este trabajo también proponemos investigar reacciones de arranque de nucleones. Estas reacciones han sido muy utilizadas para caracterizar la estructura de partícula independiente de los núcleos que participan en estas colisiones, así como la extensión radial de núcleos alejados de la estabili-

dad. En este trabajo proponemos utilizar estas reacciones para investigar excitaciones nucleares en los procesos de arranque de nucleones.

Esta tesis doctoral presenta un estudio experimental de las reacciones que acabamos de describir basado en un experimento que se realizó en las instalaciones del laboratorio GSI de Alemania en Junio de 2011. Este experimento se basa en el uso de la cinemática inversa y un espectrómetro magnético de alta resolución para caracterizar de forma más precisa y eficiente los núcleos residuales del proyectil que se producen en las reacciones de intercambio de carga y arranque de nucleones. Además, se utilizaron haces de isótopos estables (^{112}Sn y ^{124}Sn) e inestables (^{110}Sn y ^{120}Sn) de estaño acelerados a 1000, 700 y 400 A MeV. También se utilizaron diferentes materiales blancos (C, CH₂, Cu y Pb) para estudiar de forma sistemática estas reacciones en función del isospín y energía de los núcleos proyectil y de la naturaleza del material blanco. A continuación describimos el experimento realizado, los observables experimentales utilizados para la caracterización de estas reacciones y los principales resultados obtenidos.

Descripción del experimento

En este experimento se utilizó el sincrotrón SIS18 del GSI para acelerar haces de ^{112}Sn y ^{124}Sn a energías relativistas. Estos haces se utilizaron para realizar dos tipos de medidas. En las primeras se utilizaban estos haces estables directamente para inducir reacciones de intercambio de carga y arranque de nucleones de estos núcleos sobre blancos situados a la entrada del espectrómetro magnético FRS. En este caso se utilizaba todo el espectrómetro para identificar isotópicamente los fragmentos del proyectil resultantes y medir con gran precisión su momento longitudinal. El segundo tipo de medidas consistía en fragmentar los núcleos de ^{112}Sn y ^{124}Sn en un blanco situado también a la entrada del FRS para producir un haz secundario de otros isótopos no estables de estaño, en particular ^{110}Sn y ^{120}Sn . Estos haces secundarios de núcleos no estables se separaban e identificaban utilizando la primera sección del FRS. Un segundo blanco situado en el plano focal intermedio del espectrómetro permitía inducir las reacciones de intercambio de carga y arranque de nucleones. En este caso los fragmentos del proyectil resultantes se identificaban con la segunda sección del espectrómetro. Estas dos configuraciones experimentales están esquematizadas en la figura C.1.

El separador de fragmentos FRS es un espectrómetro magnético de gran resolución que permite identificar isotópicamente y sin ambigüedad cualquier núcleo residual producido en reacciones inducidas por proyectiles relativistas.

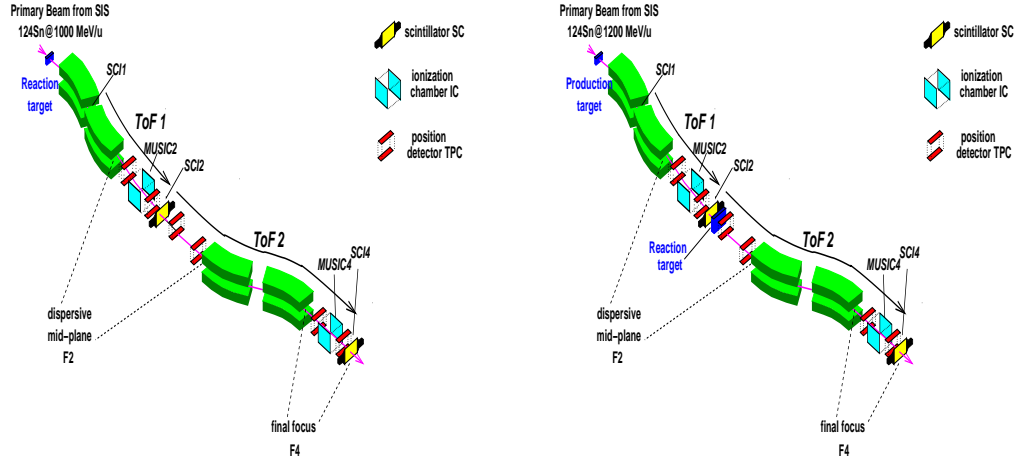


Figure C.1: Representación de las dos configuraciones del FRS usadas en este trabajo. La figura de la izquierda corresponde a la configuración cuando para las reacciones usando haces directos. La figura de la derecha muestra la configuración experimental para trabajar con haces secundarios.

Esta identificación se basa en la medida combinada de la rigidez magnética de estos núcleos residuales, de su velocidad y de la determinación de su número atómico a partir de la expresión siguiente:

$$B\rho = \frac{Au}{Qe} \gamma\beta c \quad (\text{C.1})$$

La rigidez magnética se determina midiendo con una precisión, del orden del milímetro, la posición transversal de las trayectorias de esos núcleos en los planos focales del FRS. Esta posición se obtiene utilizando las cámaras de proyección temporal situadas en el plano imagen intermedio y final del espectrómetro. La velocidad se determina a partir de la medida del tiempo de vuelo de los núcleos residuales utilizando los centelleadores plásticos situados en los planos imagen intermedio y final del espectrómetro. Finalmente el número atómico de estos fragmentos se obtiene midiendo su pérdida de energía en cámaras de ionización situadas también en los dos planos imagen del espectrómetro.

Observables

Las medidas obtenidas con el separador de fragmentos FRS permiten determinar los observables que se proponen utilizar en esta investigación. El primero de ellos es la sección eficaz de los canales de reacción utilizas

para investigar excitaciones nucleares y subnucleares en diferentes isótopos de estaño. La determinación de estas secciones eficaces depende de la identificación isotópica de los fragmentos del proyectil así como de la medida precisa del flujo de proyectiles incidentes. Para poder determinar estas secciones eficaces con precisión hay que corregir la tasa de producción medida de los fragmentos del proyectil que corresponden a las reacciones de interés para este trabajo de la eficiencia del dispositivo experimental. Esta eficiencia está determinada por el tiempo muerto del sistema de adquisición de datos, la aceptación en momento y ángulo del espectrómetro magnético, las reacciones secundarias en el propio blanco y en el resto de materiales que se encuentran a lo largo del espectrómetro y la propia eficiencia de detección de los detectores utilizados.

El segundo observable que se propuso utilizar es el espectro de energía perdida por los núcleos proyectil en las colisiones. Este espectro puede determinarse a partir de la medida del momento longitudinal de estos núcleos que puede obtenerse a partir de su rigidez magnética y su identificación isotópica.

Como el momento transversal de estos núcleos es muy pequeño comparado con su momento longitudinal podemos obtener la energía de los fragmentos del proyectil de acuerdo con la ecuación:

$$p_{\parallel} = \gamma m_0 v = qB\rho \quad (\text{C.2})$$

Finalmente obtenemos la energía perdida por los proyectiles por transformación al sistema de referencia definido por la velocidad que llevan esos proyectiles en la mitad del blanco.

La resolución de estas medidas está limitada sobre todo por la dispersión en energía que inducen los blancos de reacción. Por esta razón se han utilizado blancos muy finos (~ 100 mg/cm²) para investigar estas reacciones con haces de núcleos estables (^{112}Sn y ^{124}Sn). En el caso del estudio de las reacciones inducidas por núcleos no estables estamos limitados por la intensidad de esos haces secundarios y por tanto tenemos que utilizar blancos más gruesos (~ 1000 mg/cm²) que afectan a la resolución de las medidas.

Estudio de las reacciones de intercambio de carga isóbaras.

El principal observable que utilizamos para caracterizar las reacciones de intercambio de carga isóbaras es el espectro de energía perdida por los correspondientes fragmentos del proyectil en estas reacciones (A,Z-1) y (A,Z+1). En la figura C.2 se muestra un espectro típico. En esta figura pueden observarse claramente dos componentes una que corresponden a reacciones

en las que se disipa poca energía y otra para reacciones en las que se ha disipado mucha energía. Estas dos componentes las asociamos a las reacciones de intercambio de carga cuasielásticas que dan lugar a excitaciones nucleares y a las reacciones de intercambio de carga inelásticas que dan lugar a excitaciones subnucleares. Por tanto podemos concluir que el espectrómetro magnético FRS tiene una resolución suficiente para identificar esos dos canales de reacción.

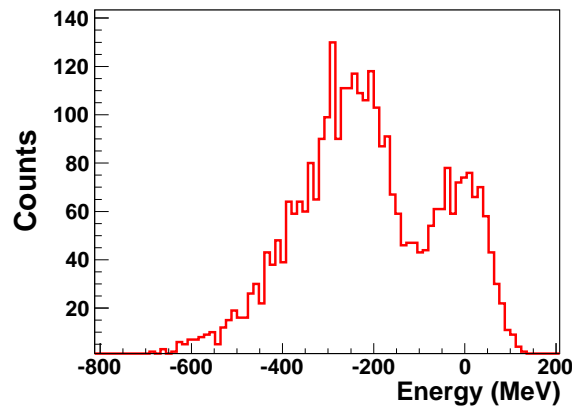


Figure C.2: Distribucion de energía para la reacción de intercambio de carga en el sistema de referencia del proyectil en la reacción del $^{124}\text{Sn}(C,X)^{124}\text{Sb}$ a 1 A GeV.

En este trabajo se hizo un esfuerzo adicional por mejorar la resolución de estas medidas deconvolucionando estos espectros de la respuesta del dispositivo experimental. Para realizar esta deconvolución de forma precisa se tuvo que desarrollar un nuevo método de regularización que permitiese determinar el número óptimo de iteraciones. Además se determinó de forma precisa la función de respuesta del dispositivo experimental a partir de medidas realizadas centrando el haz de proyectiles que no habían reaccionado en el blanco a lo largo de todo el espectrómetro. El resultado de esta deconvolución se ilustra en la figura C.3 donde mostramos el espectro de energía perdida por los fragmentos de ^{124}Sb producidos en reacciones de intercambio de carga isóbaras inducidas por ^{124}Sn sobre un blanco de carbono a 1000 A MeV. En esta figura el histograma (línea sólida) representa el espectro medido, el histograma y el histograma con la línea a trazos es el resultado de la deconvolución.

El espectro deconvolucionado muestra una mejora clara en la resolución de la medida que permite incluso apreciar diferentes subestructuras en la

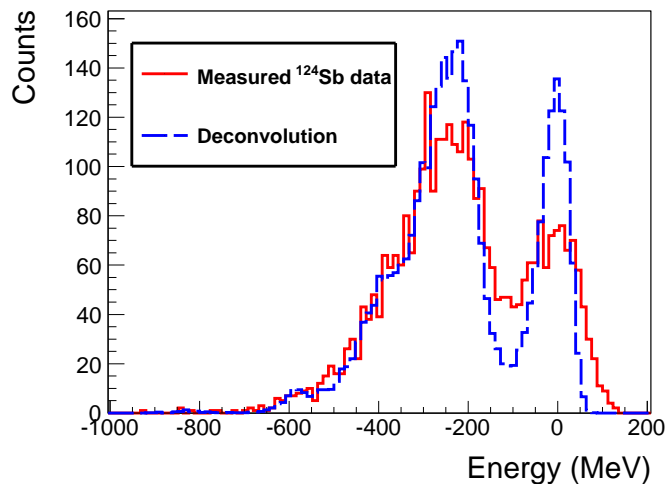


Figure C.3: Distribución energía (línea sólida) y su respectiva deconvolución (línea a trazos) en la reacción del $^{124}\text{Sn}(C,X)^{124}\text{Sb}$ a 1 A GeV.

componente inelástica de la reacción de intercambio de carga. La componente principal del canal inelástico corresponde a una resonancia centrada alrededor de unos -250 MeV y con una anchura de 114 MeV que asociamos a la excitación de la resonancia Δ .

En la figura C.4 ajustamos la estructura correspondiente a la resonancia Δ a una función Breit-Wigner que al sustraerla del espectro total muestra claramente la existencia de otras dos resonancias adicionales a la Δ . La primera de ellas con una energía media de -400 MeV y una anchura de unos 100 MeV, que es compatible con la excitación de una resonancia Roper, pero la tercera todavía no hemos podido identificarla.

Esta conclusión puede confirmarse estudiando la dependencia de estas excitaciones con la energía de la colisión. En la figura C.5 representamos el espectro de la energía perdida por fragmentos de ^{112}Sb producidos en reacciones de intercambio de carga isóbaras inducidas por ^{112}Sn sobre carbono a 1000 A MeV (línea roja a trazos), 700 A MeV (línea negra continua) y 400 A MeV (línea azul a puntos). Según lo esperado, a 700 A MeV la excitación de la resonancia Roper y de la tercera resonancia desaparecen y a 400 A MeV se reduce incluso la excitación de la resonancia Δ ya que estamos cerca de su umbral e producción.

Además estos resultados son sistemáticos, es decir que se observan excitaciones de resonancias bariónicas con todos los proyectiles y blancos que se han investigado tal y como se muestra en la figura C.4. Estos resultados

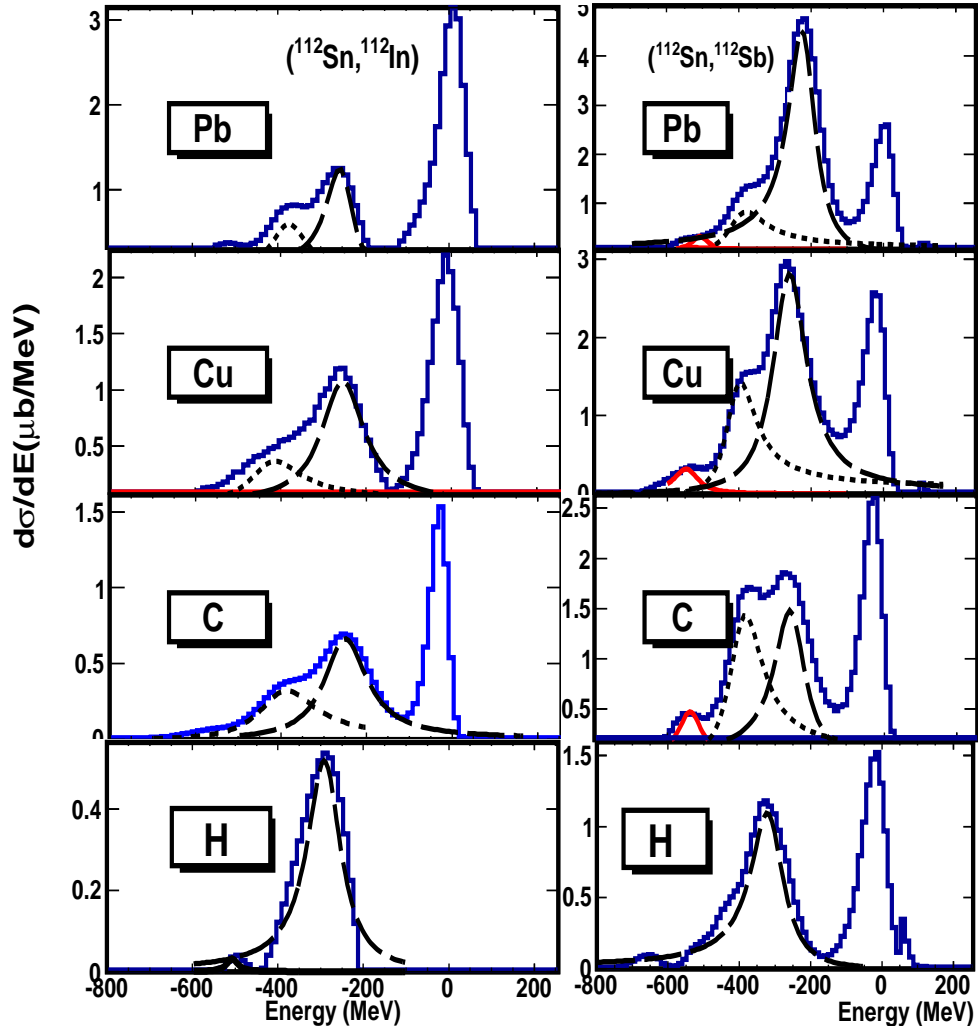


Figure C.4: Ajustes a los espectro deconvolucionados (línea sólida) usando una función Breit-Wigner generalizada. La línea a trazos indica la excitación de la resonancia Δ mientras que la línea a puntos representa la resonancia Roper.

confirman que hemos sido capaces de excitar resonancias bariónicas en materia nuclear. Incluso de que también es posible excitar esas resonancias en núcleos no estables, aunque con peor resolución. Este resultado abre la posibilidad de estudiar las propiedades de estas resonancias en materia nuclear asimétrica.

La interpretación cuantitativa de estos resultados requiere un estudio mucho más detallado y el uso de modelos teóricos que permitan describir estos canales de reacción. De hecho cuando se analizan los posibles procesos que

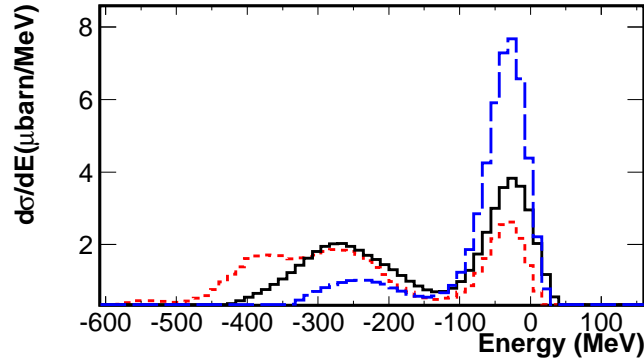


Figure C.5: Dependencia con la energía del canal inelástico en la reacción $^{112}\text{Sn}(C, X)^{112}\text{Sb}$ a 400 A MeV (línea a trazos), 700 A MeV (línea sólida) 1 A GeV (línea a puntos).

pueden dar lugar a la señal de excitación de resonancias bariónicas que observamos se concluye que en realidad una misma estructura en el espectro de energía perdida puede corresponder a la suma de diferentes canales de excitación de una misma resonancia o incluso a la suma de excitaciones tanto en el núcleo proyectil como en el núcleo blanco tal y como se muestra en la figura C.6 y C.7. Este estudio nos permite concluir que para poder utilizar los observables propuestos en este experimento para caracterizar la excitación de resonancias bariónicas en el medio nuclear será necesario realizar experimentos exclusivos que permitan detectar en coincidencia los piones emitidos para poder seleccionar así el canal concreto de excitación y si ésta tiene lugar en el proyectil o en el blanco. Del mismo modo la cuantificación de las abundancias relativas de protones y neutrones en la periferia del núcleo requerirá el uso de modelos teóricos.

Estudio de reacciones de arranque de nucleones.

En este experimento también se pudo medir con precisión las secciones eficaces de los canales de arranque de protones y neutrones de los isótopos estables y no estables de estaño utilizados como proyectiles en este experimento. Además, pudimos completar estas medidas con otros datos obtenidos también en el FRS para proyectiles de ^{132}Sn y en Riken para proyectiles de ^{104}Sn . De esta forma podemos estudiar la evolución sistemática de las secciones eficaces de estos procesos sobre un rango de isospín muy grande.

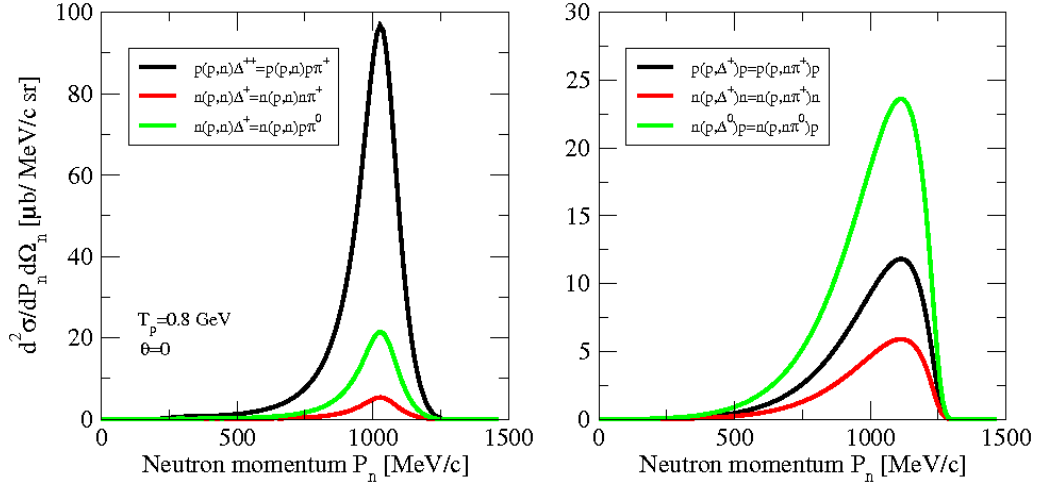


Figure C.6: Contribuciones de la resonancia Δ a la sección eficaz doble diferencial a el proceso elemental (p,n) [118]. La gráfica de la izquierda muestra la excitación de la resonancia en el blanco y la La gráfica de la derecha la excitación en el proyectil.

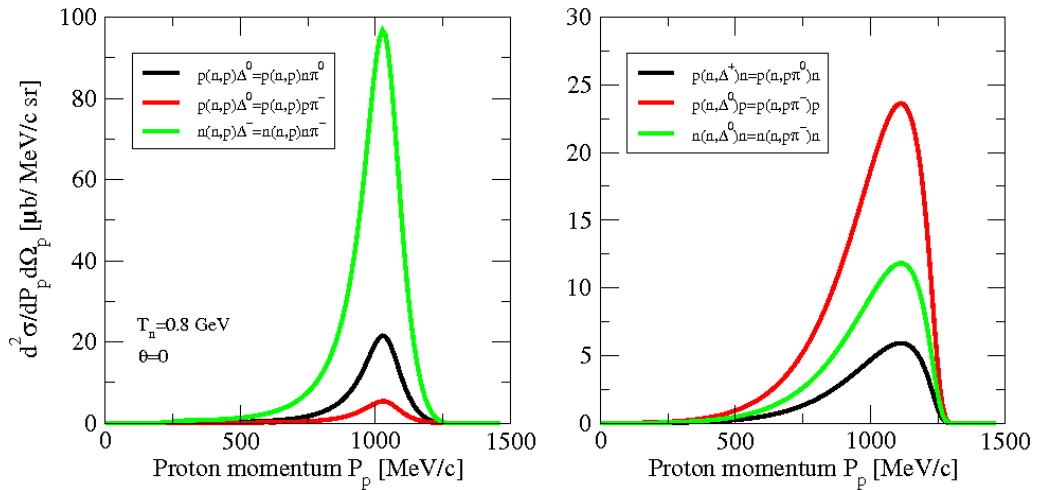


Figure C.7: Contribuciones de la resonancia Δ a la sección eficaz doble diferencial a el proceso elemental (n,p) [118]. La gráfica de la izquierda muestra la excitación de la resonancia en el blanco y la La gráfica de la derecha la excitación en el proyectil.

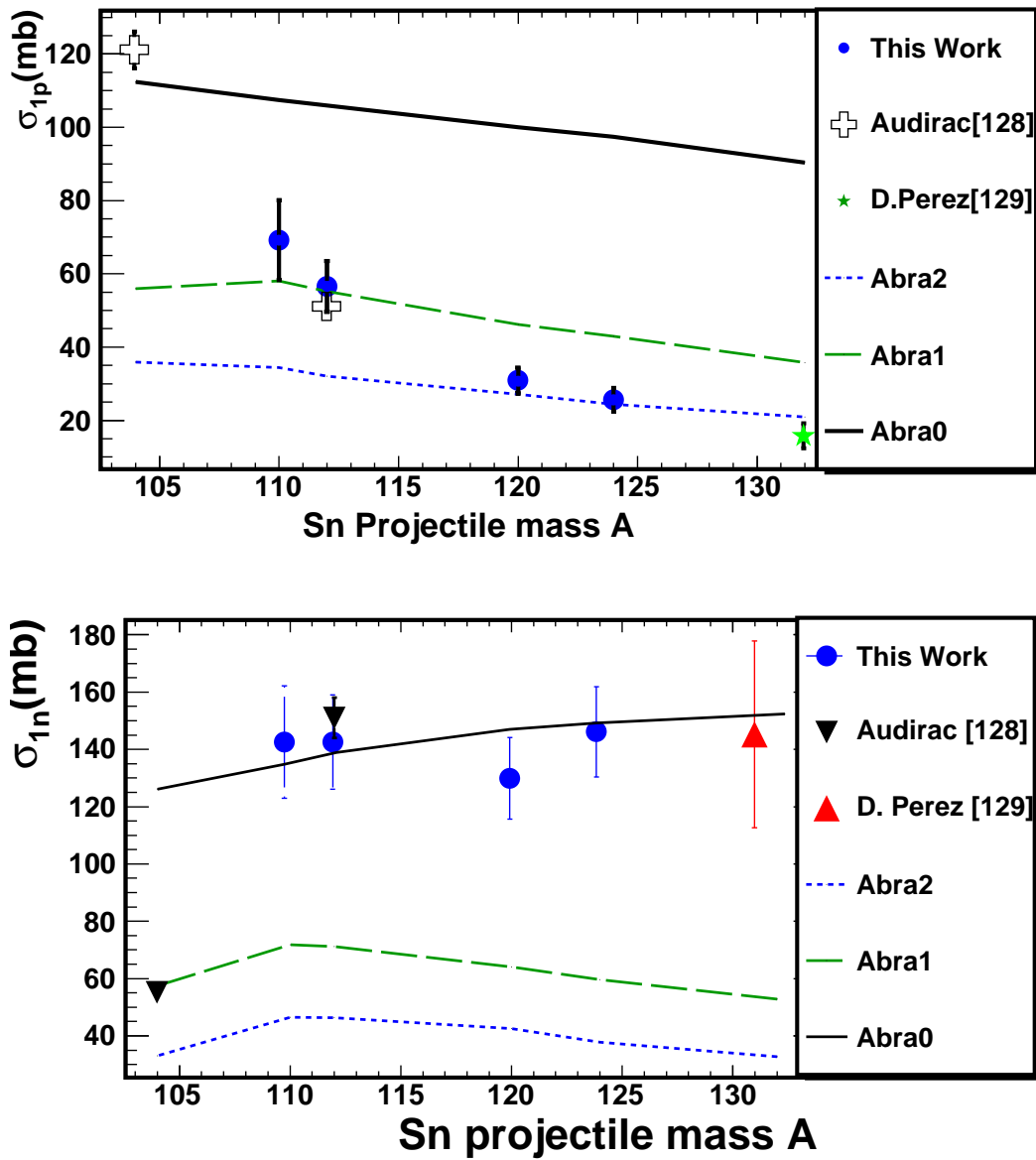


Figure C.8: Figura superior: secciones eficaces de arranque de protón en función de la masa del proyectil de Sn. Figura inferior: secciones eficaces de arranque de neutrón en función de la masa del proyectil de Sn sobre un blanco de carbono.

En la figura C.8 se muestra la evolución de las secciones eficaces de arranque de un protón (panel superior) y de un neutrón para diferentes isótopos de estaño incidiendo sobre un blanco de carbono. Como puede verse la evolución de las secciones eficaces de estos dos canales de reacción con el exceso de neutrones del núcleo es inversa. Para núcleos con un mayor exceso de neutrones la probabilidad de arrancar un neutrón es seis veces mayor que la de arrancar un protón y la tendencia se invierte para los núcleos deficitarios en neutrones.

En estas figuras también comparamos las secciones eficaces medidas con las predicciones obtenidas con un modelo de abrasión-evaporación. El primer cálculo corresponde a las secciones eficaces obtenidas suponiendo que el núcleo residual no se excita tras arrancarle un protón o neutrón (línea negra continua). En los otros cálculos suponemos que la excitación que gana el núcleo se puede describir a partir de excitaciones de partícula independiente dentro una distribución de Fermi de los nucleones (línea verde a trazos) y el mismo cálculo pero incrementando artificialmente el valor de la energía de excitación por un factor dos (línea azul punteada). Como puede verse, los cálculos sin excitación nuclear reproducen las secciones eficaces de arranque de nucleones poco ligados, los neutrones en el caso de núcleos con gran exceso de neutrones y los protones en el caso de núcleos deficitarios en neutrones. El cálculo que incluye excitaciones de partícula independiente sólo describe las secciones eficaces de arranque de nucleones de núcleos próximos a la estabilidad. Finalmente, para describir las secciones eficaces de arranque de los nucleones más ligados, protones en núcleos ricos en neutrones y neutrones en núcleos deficitarios en neutrones, necesitamos incrementar artificialmente la excitación calculada asumiendo excitaciones de partícula independiente. Estos cálculos muestran la importancia que tienen las excitaciones nucleares a la hora de describir las reacciones de arranque de nucleones.

Conclusiones y perspectivas

En este trabajo de tesis doctoral se han estudiado excitaciones nucleares y subnucleares en reacciones periféricas inducidas por núcleos pesados relativistas. En particular hemos realizado un experimento para estudiar excitaciones subnucleares en reacciones de intercambio de carga isóbaras y excitaciones nucleares en reacciones de arranque de nucleones. La técnica experimental utilizada se basaba en el uso de la cinemática inversa con la que se puede identificar sin ambigüedad los fragmentos del proyectil resultantes y medir con gran precisión su momento longitudinal utilizando un espectrómetro magnético de gran resolución. Esta técnica experimental ha

permitido utilizar dos observables para estudiar estas reacciones, las secciones eficaces de estos canales de reacción y la energía perdida en la reacción por los fragmentos del proyectil.

El estudio de las reacciones de intercambio de carga isóbaras ha permitido demostrar que el espectrómetro magnético FRS tiene una resolución suficiente como para separar las componentes cuasielástica e inelástica de este canal de reacción. Además la deconvolución de la respuesta del dispositivo experimental utilizando una técnica de regularización desarrollada en el ámbito de este trabajo ha permitido mejorar la resolución de los espectros de pérdida de energía de los residuos del proyectil. Esta mejora en la resolución ha permitido evidenciar la existencia de subestructuras en la componente del canal inelástico que asociamos a la excitación de diferentes resonancias bariónicas, en particular la resonancia Δ y la Roper. Esta interpretación se apoya también en la dependencia con la energía de la reacción observada para dichas excitaciones. Por tanto podemos concluir que el presente trabajo ha demostrado que se pueden excitar resonancias bariónicas en el medio nuclear y en particular en materia nuclear asimétrica. Estas medidas también muestran como las secciones eficaces de estos procesos dependen de la abundancia relativa de protones y neutrones en la periferia de los núcleos que participan en la colisión. En cualquier caso, un estudio detallado sobre las propiedades de bariones en el medio nuclear requeriría medidas exclusivas que permitiesen identificar los mesones (piones) emitidos en la desexcitación de esos bariones.

Finalmente el estudio de las reacciones de arranque de nucleones nos ha permitido estudiar las excitaciones nucleares en función del isoespín de los núcleos. Las secciones eficaces medidas indican que el arranque de nucleones poco ligados no inducen excitación alguna en el núcleo resultante. Por el contrario el arranque de nucleones muy ligados inducen excitaciones que van más allá de las que se obtendrían en el marco de excitaciones de partícula independiente.